UNIVERSITY OF LIVERPOOL

Crystal Structure Prediction for Complex Modular Materials

Thesis submitted in accordance with the requirements of the University of Liverpool for the degree of Doctor in Philosophy by

Kathryn Bradley

supervised by

Dr. George Darling

January 2017

Contents

Acknowledgements

Firstly, I'd like to thank my supervisor Dr George Darling, who has been a patient and supportive force throughout my PhD. I'd also like to thank Dr Matthew Dyer for his endless help, with no query too small or unimportant for his time. In terms of research, without the support and input of the Solid State Chemistry group, including Dr Christopher Collins, Dr John Claridge and Professsor Matthew Rosseinsky, this thesis would not have been possible.

My time at the University of Liverpool has been varied, and has opened new doors for me, both personally and professionally. I was able to discover climbing, a hobby that has now turned into a passion. I'd like to thank my friends at the University of Liverpool Mountaineering Club for this opportunity and outlet.

It is simply not possible to list every person who has contributed to my time here. I'd like to thank my friends, family and colleagues for everything. Specific mentions go to Dr John Sharp and (hopefully!) Dr Anna Gould for their input and advice.

Above all, I'd like to thank James.

Crystal Structure Prediction for Complex Modular Materials

Kathryn Bradley

This thesis concerns work on the structure solution and prediction of novel inorganic compounds, with specific focus on compounds that show potential use in commercial applications. The ability to predict structures at the atomic and molecular scale is a challenge at the forefront of inorganic and materials chemistry.

Complex functional transition metal oxides can generally be described in terms of modules containing elements in particular chemical environments. This observation has led to the development of the Extended Module Materials Assembly (EMMA) approach for the generation of plausible candidate structures. The EMMA method is extended in this project to examine hexagonal perovskites and is first applied to $Ba(Co,Nb)_{1-\delta}O_3$, examining known structures to facilitate the discovery of new structures within the structural series.

In the second instance, the EMMA method is applied to $Ba_3Nb_2O_8$, which has an unconfirmed structure experimentally. It is in this case that the advantages and disadvantages of the EMMA method become increasingly apparent, with structures identified in the initial screening using classical lattice dynamics becoming less stable when re-ranked with density functional theory.

Moving away from the EMMA method, a mixed system of $LiMgPO_4$ and Li_2MgSiO_4 is investigated based on Monte-Carlo site-swapping in an ideal oxide lattice. As with the EMMA approach, this method has several advantages and disadvantages, with successes seen for some compositions but not in others.

The results in this thesis demonstrate the difficulty in rising to the challenge of crystal structure prediction and the exciting avenues that can be explored to help find answers. It is hoped that the work in this thesis can be built on in the future, through optimisation of the above methodologies and experimental synthesis of predicted compounds.

Chapter 1

Introduction

1.1 Crystal Structure Prediction

Great progress has been made in the field of molecular modelling. We are increasingly able to mimic the behaviour and properties of molecules at the atomic level, giving us greater insight into the chemical principles underlying certain phenomena. However, predicting the structure and arrangement of atoms, with only knowledge of the chemical formula, remains a key challenge in chemistry.[1] For each chemical composition, there is an infinite number of possible atomic arrangements. The problem is finding the most stable configuration, at a given pressure and temperature, with only knowledge of the chemical formula and constituent atoms.

The ability to predict compounds brings many advantages. Knowledge of a crystal structure gives information about a large number of properties and can thus direct synthetic research. It also provides the opportunity to study matter at temperatures and pressures that would be difficult to study experimentally, with cost and safety coming into consideration.

Until recently, it was believed that crystal structures were practically unpredictable. The question, "Are crystal structures predictable?" was often met with a resounding no.[2] Our

inability to predict even the simplest of crystalline solids was termed a 'scandal' in an editorial in Nature in 1988:

> One of the continuing scandals in the physical sciences is that it remains impossible to predict the structure of even the simplest crystalline solids from a knowledge of their composition.[3]

However, a recent 'scientific revolution' has resulted in dramatic change. Crystal structures are no longer believed to be unpredictable;[4] much progress has been made in developing methods that have successfully predicted the structures of unknown compounds. This thesis aims to build on the recent successes extending and developing methodologies to different systems.

1.2 Application to Solid State Chemistry

The ability to design molecules that have specific functions is important in all areas of synthetic chemistry. In terms of molecular chemistry, a key step in drug development involves the synthesis of molecules that have been specifically designed to have a certain physiological action,[5] and it is common in organometallic chemistry to design compounds that have a specific catalytic action.[6] However, much of solid-state chemistry involves altering the synthesis conditions in order to yield compounds that may be of interest, without consideration of the predicted structure. Indeed, it has been said that serendipity is one of the key driving forces behind most solid state discoveries.[7]

Nonetheless, the ability to predict structures with specific physical and chemical properties is of great importance in solid state chemistry to drive forward the search for functional materials, such as those that can be used in lithium-ion batteries, photovoltaic cells and hydrogen fuel cells. The ideal properties for components of these technologies are well known, so the ability to predict structures and hence their properties can lead to major

advances in these fields.[8]

There are two key factors that influence crystal structure determination: search and ranking. Searching involves exploring the multidimensional energy landscape efficiently, and ranking involves the ability to correctly identify the lowest energy structure. It is these factors that differentiate organic crystal prediction from inorganic. Organic crystals tend to have very few atoms in the unit cell, making search relatively straight forward. However, many of the conformations are similar in energy, which makes ranking a key concern. For inorganic crystals, with many atoms in the unit cell, searching becomes the main issue. In addition, organic systems are often constrained in specific bonding geometries, which is not the case in inorganic systems.

A distinction between crystal structure prediction and solution must also be made. Crystal structure prediction occurs when there is no information available, for example unit cell dimensions or atomic coordinates. Thus, the search is 'blind' with no empirically based information. A sub-class of predictive methods, structure solution, determines the atomic positions of the elements with knowledge of the composition and unit cell dimensions. The ultimate aim for both solution and prediction remains the same: 'to announce a crystal structure before any confirmation by chemical synthesis or discovery in nature.'[9]

There are two principle streams of crystal structure prediction: one is derived from pre-existing knowledge of structures, often called data mining, while the other is based on global optimisation strategies, evaluating structure stabilities.[10] As a result, the primary focus of this literature review is to give a general outline of the techniques that are able to predict and identify suitable candidate structures from a known chemical composition.

1.3 Data Mining and High-Throughput Computing

Data centred methods mine existing data libraries to help understand new situations: a large volume of experimental observations are used in order to extract rules that rationalise trends in crystal structure with simple physical properties such as atomic radii, electronegativity and oxidation states.[11] This can be seen in Pettifor maps[12] and other structural mapping techniques[13] that predict the structure of new materials through the correlation of stable crystal structures.

The foundation for this approach can be found in Pauling's rules for determining the structure of complex ionic crystals.[14] He developed a set of principles based on the assumption of a coordinated arrangement of anions surrounding a cation, which are found at the corners of an approximately regular polyhedron. However, the main difficulty with using these rules to identify new structures results from the large number of structures that can be constructed for a given composition, due to the general and qualitative nature of the rules themselves. While structure maps have been used predictively,[15] they are more suited to explain already characterised crystals due to their focus on specific details.

An extension to Pauling's concept of corner-sharing polyhedra comes in the form of using larger building blocks to generate candidate structures. This greatly reduces the number of structures generated, as both 2D and 3D building blocks can be used. These 2D or 3D building blocks can then be stacked to create novel inorganic compositions.[16,17] This approach allows crystal structure solution to be more rational and intuitive.[18] It is from this rationale that the Extended Module Materials Assembly (EMMA) builds from, discussed in more depth in Chapter 3 and implemented in Chapters 4 and 5.

The bond valence method, derived from the concept of bond number, allows for an excellent approximation of the bond length.[19] This provides a powerful basis from which to search for promising candidates; however, the structure for many inorganic solids results from the

compromise between the conflicting requirements of chemical bonding and three-dimensional geometry, which require many ideal bond lengths to be strained.[20]

Other approaches include machine learning and statistical learning, where previous computations and experiments help to make informed guesses about likely candidate structures.[21] These take the form of regression analyses, such as the correlation between the energy of crystal structure prototypes in a binary system and probabilistic functions, where chemical substitutions and phase diagrams can be explored.[22,23]

However, in all instances, the candidate structures are finally evaluated using energy minimisation. The initial prediction is not enough, and is used to help with the extensive search of the energy landscape. High-throughput calculations help to identify promising structures, but they do not guarantee the stability of such structures. Only knowledge of the energy landscape allows for the informed choice of the stability of a structure.

1.4 Global Optimisation Methods

Quantum mechanical approaches, such as DFT,[24] are most often used for structure refinement rather than prediction. This generally means that known structures are taken and relaxed to local minima, and properties such as energy and density of states (DOS) can be calculated. For this reason, DFT is often combined with global minimum searching algorithms to great effect. This offers several advantages, such as explicit calculation of energies and unbiased searching techniques that can produce unexpected and novel structures. Due to the computational expense, interatomic potentials may be used in compromise. However, optimisation with either DFT or interatomic potentials both allow for the search of the energy landscape, with the choice often being speed or accuracy.

Materials form structures that are in thermodynamic equilibrium, unless they are kinetically constrained. Therefore, to predict a novel structure, the arrangement of atoms must minimise

the Gibbs free energy, given by the equation:

$$G = U - TS + pV \tag{1.1}$$

where U is the internal energy, T is the temperature, S is the entropy, p is the pressure and V is the volume. Entropy is often neglected, constraining the search at 0 K, due to the computational expense of the vibrational and configurational components.[25,26] The formula $H = U + pV$ is used to approximate the Gibbs free energy, and temperature effects can be included following identification of promising structures, using techniques such as molecular dynamics. Therefore, to search for stable materials, the enthalpy per atom must be minimised.

A complete description of a crystal structure can be thought in terms of multidimensional space, referred to as an energy landscape. The number of dimensions in any given energy landscape is given by:

$$d = 3N + 3 \tag{1.2}$$

where $3N - 3$ degrees of freedom are the atomic positions, and the remaining six dimensions are lattice parameters. Equation 1.2 illustrates that as the size of the system increases, the dimensionality also increases and hence prediction becomes more difficult. For example, for a system with 100 atoms, the landscape is 303-dimensional, while for a system containing 200 atoms, the landscape increases to become 603-dimensional.

However, the problem can be simplified using structure relaxation. During relaxation, correlations between atomic positions occur. Therefore, the dimensionality is reduced to:

$$d^* = 3N + 3 - \kappa \tag{1.3}$$

where κ is the non-integer value of correlated dimensions.

The lowest enthalpy structure is found at the deepest minimum of the energy landscape, and is referred to as the global minimum, with the number of local minima scaling exponentially with the dimensionality of the search space.[27] Other general features of the potential energy surface are known, such as the fact that much of the configuration space corresponds to structures with unphysical small interatomic distances, which allows for the development of efficient techniques to search the energy landscape.

For very small systems, with $N < 8 - 10$, a combination of random sampling[28] and local optimisation has delivered correct solutions. However, for systems with many atoms in the unit cell, more sophisticated methods must be used. As can be shown by Figure 1.1, efficient local optimisation is beneficial to the solution of reaching the global minimum, transforming the energy landscape into basins of attractions.

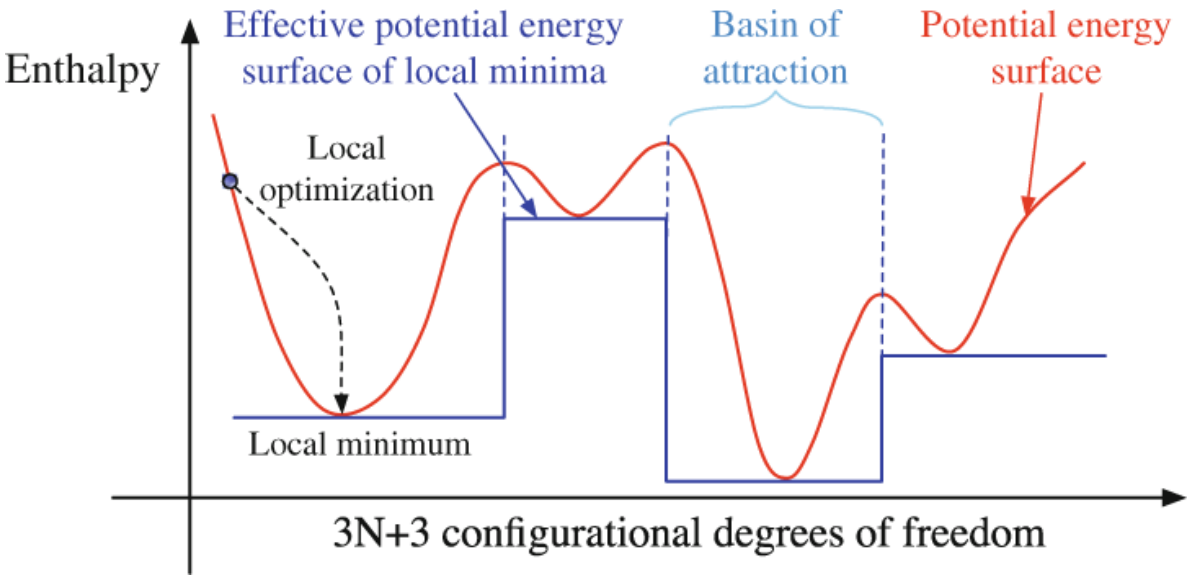

Figure 1.1: A potential energy surface. The use of local optimization simplifies the search problem by dividing the solution space into basins of attraction.[29]

Simulated annealing, which is based on physical concepts from physical annealing, is a technique used to search the energy landscape.[30] When a metal is slowly cooled from the molten state, the disordered atoms can crystallise in an ordered manner, reaching the global minimum. In computational simulations, the configuration is perturbed using either molecular

dynamics or Monte Carlo at each specific temperature, according to prescribed operations. The operations are known as move class operators, and take the form of a variety of changes to the candidate strucutres, such as swapping ions, removing or adding ions, or changing unit cell dimensions, if applicable. A criterion[31] is used to determine whether the move is accepted or rejected, based on the change in energy.

A very similar method to simulated annealing is basin hopping,[32] whereby new structures, obtained by either a Monte Carlo move or molecular dynamics, are immediately quenched or relaxed to a local minimum. Therefore, the accepted criterion is based on a comparison between the minimised energies. This method is used in Chapter 6, using Monte Carlo site-swapping between ions. This methodology has since been expanded, and can include thermodynamics via basin sampling or parallel tempering.[33] A similar method is known as minima hopping, with the aim of reducing the rate of return to already visited minima.[34]

However, all of the techniques described above are limited by the configuration space, because if the search is started in a 'poor' region, effort is often wasted. Another alternative is to use a 'self-improving' method, that locates the best structures, and uses these to generate further structures. One such method is evolutionary algorithms.

Evolutionary algorithms are derived from the concept of evolution, as the name suggests.[35] The population evolves through reproduction, mutation, recombination and selection, as in the biological sense of the word. Eventually, the population moves towards the energetically most favourable structure, through a fitness function that determines the survival of individual candidates in the population. As with all methods, there are limitations with evolutionary algorithms. There is a compromise between diversity of the population and convergence to the optimum solution. Reducing the population size decreases the computing expense and allows the population to collapse into a local minimum faster, whilst also increasing the risk of omitting the global minimum.

1.5 Outlook and thesis aims

While the answer to the question, "Are some crystal structures predictable?" is now 'yes', the answer is not yet definitive. There is no universally accepted method, with most studies focusing on one particular method. Indeed, it may be the case that certain methods work best on specific systems, or that a combination of approaches is necessary. While blind tests of molecular organic crystals are now common, where several approaches are tested against a known compound and compared, the same cannot be said for inorganic structures where the combinatorial complexity of the problem is much larger.

This thesis aims to expand and develop the points introduced earlier, investigating systems of interest for their potential application in materials chemistry. Two methods are implemented, but both make use of the same theoretical methods to calculate energies: interatomic potentials and DFT, described in detail in Chapter 2.

Chapter 3 describes the first approach used in this thesis: the EMMA method. Originally developed at the University of Liverpool in the research group of Professor Matthew Rosseinsky, the EMMA method can be considered a high-throughput method aided by a series of combination rules to generate candidate structures. Chapters 4 and 5 see the implementation and development of this method, applied to a system of hexagonal perovskite structures.

Chapter 6 addresses the global optimisation problem, applying Monte Carlo site-swapping to consider the experimental synthesis of novel lithium magnesium silicate-phosphate materials. Finally, Chapter 7 provides a summary of the findings of the work described above and outlines conclusions and possible future work.

References

1. Catlow, R. & Woodley, S. M. Themed issue: Solid state and cluster structure prediction. *Physical Chemistry Chemical Physics* **12,** 8436–8437 (2010).

2. Gavezzotti, A. Are crystal structures predictable? *Accounts of Chemical Research* **27,** 309–314 (1994).

3. Maddox, J. Crystals from first principles. *Nature* **335,** 201 (1988).

4. Oganov, A. R. *Modern Methods of Crystal Structure Prediction* 1st ed. (ed Oganov, A. R.) (Wiley-VCH, 2011).

5. Schneider, G. & Fechner, U. Computer-based de novo design of drug-like molecules. *Nature Reviews Drug Discovery* **4,** 649–663 (2005).

6. Nørskov, J. K., Bligaard, T., Rossmeisl, J. & Christensen, C. H. Towards the computational design of solid catalysts. *Nature Chemistry* **1,** 37–46 (2009).

7. Cario, L. *et al.* Design and magnetic properties of new compounds containing iron 2D building blocks of the perovskite type. *Solid State Sciences* **7,** 936–944 (2005).

8. Jansen, M. & Schön, J. C. Rational development of new materials–putting the cart before the horse? *Nature Materials* **3,** 838 (2004).

9. Le Bail, A. Inorganic structure prediction with GRINSP. *Acta Crystallographica Section A* **61,** 389–395 (2005).

10. Meden, A. Inorganic crystal structure prediction-a dream coming true? *Acta Chimica Slovenica* **53,** 148–152 (2006).

11. Curtarolo, S., Morgan, D., Persson, K., Rodgers, J. & Ceder, G. Predicting crystal structures with data mining of quantum calculations. *Physical Review Letters* **91,** 135503 (2003).

12. Pettifor, D. G. The structures of binary compounds. I. Phenomenological structure maps. *Journal of Physics C: Solid State Physics* **19,** 285–313 (1986).

13. Villars, P. Three-dimensional structural stability diagrams for 648 binary AB_3 and 389 binary A_3B_5 intermetallic compounds: III. *Journal of the Less Common Metals* **102,** 199–211 (1984).

14. Pauling, L. The principles determining the structure of complex ionic crystals. *Journal of the American Chemical Society* **51,** 1010–1026 (1929).

15. Morgan, D., Rodgers, J. & Ceder, G. Automatic construction, implementation and assessment of Pettifor maps. *Journal of Physics: Condensed Matter* **15,** 4361–4369 (2003).

16. Kabbour, H., Cario, L. & Boucher, F. Rational design of new inorganic compounds with the ZrSiCuAs structure type using 2D building blocks. *Journal of Materials Chemistry* **15,** 3525–3531 (2005).

17. Cario, L., Kabbour, H. & Meerschaut, A. Designing new inorganic compounds from 2D Building Blocks. *Chemistry of Materials* **17,** 234–236 (2005).

18. Mellot-Draznieks, C. *et al.* Computational design and prediction of interesting not-yet-synthesized structures of inorganic materials by using building unit concepts. *Chemistry - A European Journal* **8,** 4102–4113 (2002).

19. Brese, N. E. & O'Keeffe, M. Bond-valence parameters for solids. *Acta Crystallographica Section B* **47,** 192–197 (1991).

20. Brown, I. D. Chemical and steric constraints in inorganic solids. *Acta Crystallographica Section B: Structural Science* **48,** 553–572 (1992).

21. Hastie, T. J., Tibshirani, R. J. & Friedman, J. H. *The elements of statistical learning: data mining, inference, and prediction* New York, 2009.

22. Hautier, G., Fischer, C. C., Jain, A., Mueller, T. & Ceder, G. Finding nature's missing ternary oxide compounds using machine learning and density functional theory. *Chemistry of Materials* **22,** 3762–3767 (2010).

23. Fischer, C. C., Tibbetts, K. J., Morgan, D. & Ceder, G. Predicting crystal structure by merging data mining with quantum mechanics. *Nature* **5,** 641–646 (2006).

24. Kohn, W., Becke, A. D. & Parr, R. G. Density functional theory of electronic structure. *The Journal of Physical Chemistry* **100,** 12974–12980 (1996).

25. Feng, J., Hennig, R. G., Ashcroft, N. W. & Hoffmann, R. Emergent reduction of electronic state dimensionality in dense ordered Li-Be alloys. *Nature* **451,** 445–448 (2008).

26. Rudin, S. P., Jones, M. D. & Albers, R. C. Thermal stabilization of the hcp phase in titanium. *Physical Review B* **69,** 094117 (2004).

27. Stillinger, F. H. Exponential multiplicity of inherent structures. *Physical Review E* **59,** 48–51 (1999).

28. Anderson, R. L. Recent advances in finding best operating conditions. *Journal of the American Statistical Association* **48,** 789–798 (1953).

29. Atahan-Evrenk, Ş., Aspuru-Guzik, A. & Adjiman, C. S. *Prediction and calculation of crystal structures : methods and applications.* (Springer International Publishing, 2014).

30. Kirkpatrick, S., Jr, D. G. & Vecchi, M. P. Optimization by Simulated Annealing. *Science* **220,** 671–680 (1983).

31. Metropolis, N., Rosenbluth, A. W., Rosenbluth, M. N., Teller, A. H. & Teller, E. Equation of state calculations by fast computing machines. *The Journal of Chemical Physics* **21,** 1087–1092 (1953).

32. Wales, D. J. Global optimization of clusters, crystals, and biomolecules. *Science* **285,** 1368–1372 (1999).

33. Wales, D. J. & Doye, J. P. K. Stationary points and dynamics in high-dimensional systems. *The Journal of Chemical Physics* **119,** 12409–12416 (2003).

34. Goedecker, S. Minima hopping: An efficient search method for the global minimum of the potential energy surface of complex molecular systems. *The Journal of Chemical Physics* **120,** 9911–9917 (2004).

35. Oganov, A. R., Lyakhov, A. O. & Valle, M. How evolutionary crystal structure prediction works—and why. *Accounts of Chemical Research* **44,** 227–237 (2011).

Chapter 2

Computational Methods

This chapter outlines key theories and methodologies used in computational chemistry, with specific attention given to those used in this work. As such, a number of reference texts were used throughout and are listed in Section 2.5 if not referenced in text.

2.1 Energy Minimisation

As introduced in Chapter 1, the problem involved with predicting the structure for any given composition involves finding the global minimum on the energy landscape. This can be formulated in terms of optimisation of the multi-dimensional energy landscape, where the aim is to find the arrangement of atoms that correspond to the lowest energy for a given composition, as shown in Figure 2.1 (a).

During optimisation, shown by Figure 2.1 (b), the initial structure (at point 1) is higher in energy, and during energy minimisation (interchangeably used in this thesis with optimisation and relaxation) the positions of the atoms are changed in a stepwise manner so that a reduction in energy is observed. Eventually, a minimum will be reached, shown by point 4. However, each arrangement of atoms will have a specific starting point on the energy

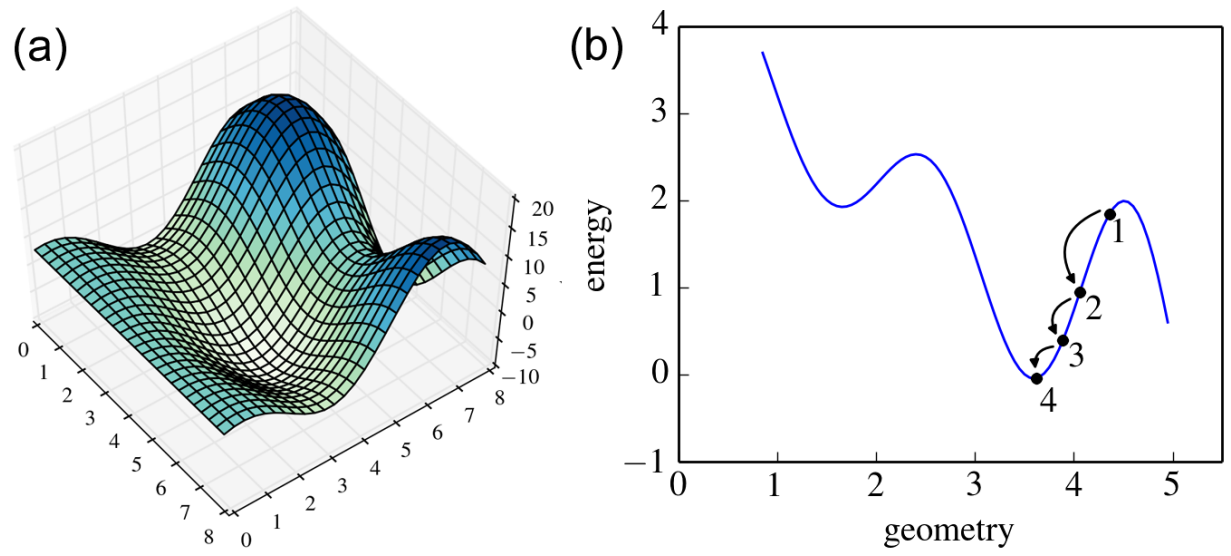

Figure 2.1: (a) A graphical representation of a multidimensional energy landscape (b) An example of an energy minimisation routine.

surface, where optimisation may only be local due to the presence of many minima in the PES. The problem then becomes a global optimisation one, as outlined in Chapter 1.

The energy minimisation method can thus be thought of as a mathematical problem relating to stationary points. Most methods proceed by determining the energy and the gradient (the derivative of the energy with respect to the position of the atoms, $\partial E/\partial r$) of the function at the starting point, and determining whether a change in the coordinates leads to a change in the gradient. For example, if the gradient is zero, a minimum has been reached.

There are a number of mathematical methods that can be used in the optimisation of PES, such as steepest descent,[1] conjugate gradient[2] and Newton-Raphson.[3] Conjugate gradient is an extension of the steepest descent method, where the search is initially directed along the largest gradient. However, following the first search, the previous direction is taken into consideration in the following search, avoiding oscillations back and forth.

Newton-Raphson is more computationally expensive than the other two methods, and involves a Taylor series expansion of the PES at the current geometry. It depends on both the gradient of the PES and the curvature, which is related to the second derivative, otherwise

known as the Hessian matrix. In general, Newton-Raphson methods are found to be superior, requiring fewer steps to find the minimum, but come at greater computational expense due to the necessity of calculating the second derivative. Amendments to this method include the Quasi-Newton method, where the Hessian matrix is estimated from successive values of the gradient.[4]

In general, the procedure for optimisation is as follows:

1. Calculate the force on each atom ($-\partial E/\partial r$)
2. Move the atoms to reduce the energy
3. Finish when the force is less than a convergence threshold, otherwise repeat.

The convergence threshold can be altered for various levels of precision, and refers to the the maximum force (usually in eV/Å) in the optimisation step in reference to the optimisation procedure above. Other convergence criteria can also be set, such as the maximum energy change (in eV/atom), the maximum stress (in GPa) and the maximum displacement (in Å). In practice, this means that there is a margin of error in the position of the minimum.

In the above scheme, the procedure depends on a calculation of the forces between each atom, which requires a model representing chemical bonding, such as quantum mechanics or interatomic potentials (forcefields). Both have benefits and issues, with forcefields (FF) requiring parameterisation, but coming at less computational expense.

2.2 Interatomic Potentials

Interatomic potentials are mathematical functions used to describe the interaction between atoms. In forcefield calculations, atoms are typically modelled as solid spheres with a radius equal to to the known value for the element in question, while bonds between particles are viewed as springs. The form of the mathematical function can vary, but must contain both

an attractive and repulsive component.

The basic functional form of a forcefield takes into account both bonded terms (where appropriate) and non-bonded terms describing long-range interactions, such as electrostatic and van der Waals (vdW) forces. The potentials are validated using experimental data and more accurate quantum mechanical calculations.

2.2.1 Common Potential Forms

One of the most common potentials used to describe vdW interactions is the Lennard Jones (LJ) potential, given by:

$$V_{\mathrm{LJ}}(r) = 4\varepsilon\left[\left(\frac{\sigma}{r}\right)^{12} - \left(\frac{\sigma}{r}\right)^{6}\right] \tag{2.1}$$

where ε represents the depth of the potential well, σ is the finite distance at which the inter-particle potential is zero and r is the distance between the particles.

The r^{-12} term dominates at short distance, and models the repulsion between atoms when they are brought in close proximity to one another. The r^{-6} term, dominating at long distance, represents the attraction between atoms. Since the LJ potential has an infinite range, it is practical to establish a cut off radius (r_c) that disregards the interactions between atoms separated at distances greater than r_c. The form of the LJ potential is shown below in Figure 2.2 (a).

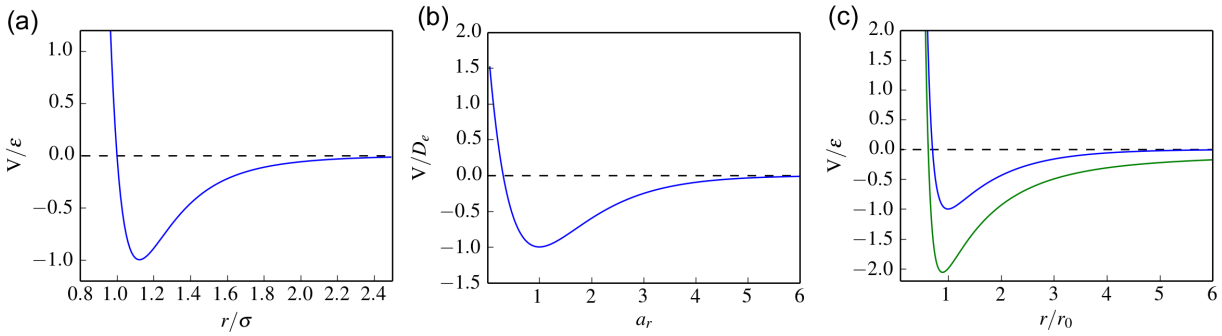

Figure 2.2: (a) The Lennard-Jones potential (b) The Morse potential and (c) The Buckingham potential, with the addition of a repulsive Coulombic interaction shown in green.

The potential provides a good description of the vdW interaction in inert gases and molecular systems, such as CH_4, H_2 and C_2H_4. An attempt to parameterise metals was found to have limited practical applications.[5] Other potentials, such as the Morse potential, are found to provide a better description of some metals with a fcc and hcp structure.[6]

The Morse potential, shown in Figure 2.2 (b), is a better approximation for the vibrational structure of a molecule than the harmonic oscillator because it includes the effects of bond breaking, and also accounts for the anharmonicity of real bonds. The potential energy function is of the form:

$$V_{\mathrm{M}}(r) = D_{\mathrm{e}}\left(e^{-2\beta\left(r-r_{\mathrm{e}}\right)} - 2e^{-\beta\left(r-r_{\mathrm{e}}\right)}\right) \tag{2.2}$$

Here, r is the distance between the atoms, r_{e} is the equilibrium bond distance, D_{e} is the well depth (defined relative to the dissociated atoms), and β controls the width of the potential well.

As the electron density falls approximately exponentially with distance from the nucleus, the repulsive component is often described by an exponential function. The form is shown in equation 2.3 below, and is commonly referred to as the Buckingham potential, demonstrated in Figure 2.2 (c).

$$V(r) = Ae^{\left(-r/\rho\right)} - \frac{C}{r^6} \tag{2.3}$$

where the terms A, ρ and C are fitted parameters.

Ionic materials are often described by a short-range repulsive term, such as the Buckingham potential, and a long-range Coulomb potential describing the interactions between the ions, shown below in equation 2.4.

$$V = \frac{q_i q_j}{4\pi\varepsilon_0 r} \tag{2.4}$$

where q_i and q_j are the formal charges on ions i and j, ε_0 is the permittivity of free space

and r is the interatomic distance between the atoms i and j.

Calculating the long-range Coloumbic interaction explicitly comes at a high computational expense due to the number of interactions that must be considered. An Ewald summation can be used to evaluate the function, which involves splitting the calculation into two parts: a short-range potential with a cut-off and the long-range potential that is periodic and slowly varying.[7] Other summation methods exist, for example the Wolf summation, which is found to be more efficient.[8]

The atomic charges can be assigned by empirical rules, or alternatively, more sophisticated charges can be assigned to account for the polarisation of atoms, such as in the case of the shell model.[9] In this model, the atoms are polarised by splitting them into two components: a core and a shell, with the charges represented by X_e and Y_e, respectively. The sum of the two charges is the same as the valence state of the ion. The shell and core are bound together via a harmonic spring, allowing the shell to move with respect to the core, giving an overall description of the polarisability of an atom α:

$$\alpha = \frac{1}{4\pi\varepsilon_0}\left(\frac{Y_\mathrm{e}^2}{k}\right) \tag{2.5}$$

where Y_e is the charge on the shell and k is the harmonic force constant.

When modelling a system, it is possible to include atoms with shells present and atoms without shells. This means that potentials can act between the core of one atom and the shell of another. Adding shells to all atoms would simply increase the calculation time when it is only necessary for some ions.

2.2.2 Parameterisation

Empirical potential fitting is an iterative process where the parameters are varied, and differences between the simulated result and experimental data are minimised. In some cases,

experimental data may not be readily available, in which case more accurate calculations (such as *ab initio* calculations) can be used in place. In most cases, the lattice constants of the unit cell of the compound are used to validate the parameters in the forcefield. Shell parameters are fitted against dielectric and elastic crystal properties in order to replicate polarisability.

Comprehensive databases of parameters exist, such as, the "Database of Published Interatomic Potential Parameters",[10] maintained by Dr Scott Woodley at University College London and the "Interatomic Potentials Repository Project"[11] at The National Institute of Standards and Technology. Care must be taken to ensure that the forcefield chosen is valid for the particular problem under consideration by ensuring the forcefield was developed for similar problems and running appropriate simulations.[12]

2.2.3 Limitations of forcefields

The use of forcefields has some intrinsic limitations.[13] Specifically, they cannot provide any information about the electronic structure of a material and cannot easily replicate reactions such as bond breaking, bond formation, and charge transfer (though the Morse potential can be parameterised to include such processes). In addition, due to their extensive parameterisation, the predictive power and transferability of forcefields is limited to conditions that match the original system. It is in this scenario that we move towards theories that do not depend so heavily on experimental data, such as density functional theory, which is outlined in the following section.

2.3 Density Functional Theory

Density functional theory (DFT) is a quantum mechanical approach for studying the electronic structure of matter. It is widely applied to a variety of problems, ranging from solid

state physics to biology.[14] In this thesis, DFT is almost exclusively used for structure optimisation, though it is routinely applied in calculations such as binding energies, band structures and magnetic properties.[15]

2.3.1 Schrödinger equation

To calculate the ground-state electronic structure, we must examine the wavefunction. Non-relativisitically, this can be calculated from the Schrödinger equation, which for a single electron moving in a potential $v(\mathbf{r})$ is given by:

$$\Big[-\frac{\hbar^2\nabla^2}{2m} + v(\mathbf{r}) \Big] \Psi(\mathbf{r}) = E\Psi(\mathbf{r}) \tag{2.6}$$

In the case of a many-body problem, where there is more than one electron, equation 2.6 becomes:

$$\Big[\sum_i^N \Big(-\frac{\hbar^2\nabla_i^2}{2m} + v(\mathbf{r_i}) \Big) + \sum_{i<j} U(\mathbf{r_i}, \mathbf{r_j}) \Big] \Psi(\mathbf{r_1}, \mathbf{r_2} ... \mathbf{r_N}) = E\Psi(\mathbf{r_1}, \mathbf{r_2} ... \mathbf{r_N}) \tag{2.7}$$

where N is the number of electrons and $U(\mathbf{r_i}, \mathbf{r_j})$ is the electron-electron interaction. For a Coulombic system, we have:

$$\hat{U} = \sum_{i<j} U(\mathbf{r_i}, \mathbf{r_j}) = \sum_{i<j} \frac{e^2}{|\mathbf{r_i} - \mathbf{r_j}| 4\pi\varepsilon_0} \tag{2.8}$$

While the kinetic energy operator is:

$$\hat{T} = -\frac{\hbar^2}{2m} \sum_i \nabla_i^2 \tag{2.9}$$

Both $\hat{U}$ and $\hat{T}$ are the same operator for any system of particles interacting via the Coulomb interaction (barring any relativistic effects). Thus, the system only depends on the potential

$v(\mathbf{r_i})$, which for a system containing more than one atom is given by:

$$\hat{V} = \sum_i v(\mathbf{r_i}) = \sum_{ik} \frac{Q_k e}{|\mathbf{r_i} - \mathbf{R_k}|} \tag{2.10}$$

where the sum on k extends over all nuclei in the system, with charge Q_k and position $\mathbf{R_k}$.

By specifying $v(\mathbf{r})$, a solution for the wavefunction Ψ can, in principle, be found using Schrödinger's equation, and expectation values of observables calculated. One such observable that can be calculated in this way is the particle density, which is given by:

$$n(\mathbf{r}) = N \int d^3 r_2 \int d^3 r_3 ... \int d^3 r_N \Psi^*\big(\mathbf{r}, \mathbf{r}_2, ..., \mathbf{r}_N\big) \Psi\big(\mathbf{r}, \mathbf{r}_2, ..., \mathbf{r}_N\big) \tag{2.11}$$

A variety of methods have been developed to solve the Schrödinger equation, but in practice this can only be applied to very small systems (with no more than a few electrons) due to the computational demands. DFT was therefore developed to provide an alternative method that is less computationally expensive.

2.3.2 Hohenberg-Kohn theorems

The Hohenberg-Kohn (HK) theorems[16] reverse the situation described above: finding the ground state energy of a system uses the electron density $n(\mathbf{r})$ as the key variable.

The first theorem states that

> The external potential $v_{\text{ext}}(\mathbf{r})$, and hence the total energy, is a unique functional of the electron density $n(\mathbf{r})$.

The energy functional can be written in terms of the external potential, $v_{\text{ext}}(\mathbf{r})$:

$$E[n(\mathbf{r})] = \int n(\mathbf{r}) v_{\text{ext}}(\mathbf{r}) d\mathbf{r} + F_{\text{HK}}[n(\mathbf{r})] \tag{2.12}$$

where $F_{\mathrm{HK}}[n(\mathbf{r})]$ is an unknown, but universal functional of the electron density $n(\mathbf{r})$.

The second theorem states that

> The ground state energy can be obtained variationally: the density that minimises the total energy is the exact ground state density.

When combined, the HK theorems are extremely powerful. The ground state energy of a system can thus be obtained by the minimisation of equation 2.12 with respect to $n(\mathbf{r})$, giving the exact ground state energy and density, and as a result it is formally exact.

2.3.3 Kohn-Sham equations

The ground state energy of a system is given by equation 2.12, where $F_{\mathrm{HK}}[n(\mathbf{r})]$ contains contributions of the kinetic energy, the Coloumb interaction and non-classical interactions. However, $F_{\mathrm{HK}}[n(\mathbf{r})]$ is not known, and further modifications are necessary in order to perform DFT calculations.

The Thomas-Fermi model gives an example of density functional theory, but the approximation of the kinetic energy functional leads to a poor performance overall. To overcome this problem, Kohn and Sham[17] proposed that the kinetic energy calculation could be facilitated by the introduction of a non-interacting reference system, the kinetic energy of which is given by T_0. The total energy functional can then be written as:

$$E\big[n(\mathbf{r})\big] = T_0\big[n(\mathbf{r})\big] + \int \big[v_{\mathrm{ext}}(\mathbf{r}) + V_{\mathrm{H}}\big] n(\mathbf{r}) d\mathbf{r} + E_{\mathrm{XC}}[n(\mathbf{r})] \tag{2.13}$$

where $T_0\big[n(\mathbf{r})\big]$ is the kinetic energy of electrons in a system that has the same density as the real system, but in which there are no electron-electron interactions. The last functional $E_{\mathrm{XC}}[n(\mathbf{r})]$ is called the exchange-correlation energy, and includes all the energy contributions that have not been accounted for by previous terms, such as:

- electron exchange
- electron correlation
- a correction to obtain the true kinetic energy of a real system, $T_e\big[n(\mathbf{r})\big]$
- a correction for a self-interaction introduced by the Coloumb potential

The form of the exchange-correlation functional is not known, and it is here that approximations enter DFT.

Minimisation of the energy of the non-interacting system with respect to non-interacting states (known as the Kohn-Sham states), taking into account orthogonality and the fact that the density of the non-interacting states equals that of the interacting sytem, leads to formulation of the Kohn-Sham (KS) equations.

The KS equations are superficially similar to the Schrödinger equation, and take the form:

$$-\left[\frac{h^2}{2m}\nabla^2 + V(\mathbf{r}) + V_{\mathrm{H}}(\mathbf{r}) + V_{\mathrm{XC}}(\mathbf{r})\right]\Psi_i(\mathbf{r}) = \varepsilon_i\Psi_i(\mathbf{r}) \tag{2.14}$$

where the first of the functions, $V(\mathbf{r})$, describes the interaction between an electron and the atomic nuclei. The second function, V_{H} is called the Hartree potential and is defined such that:

$$V_{\mathrm{H}}(\mathbf{r}) = e^2\int\frac{n(\mathbf{r'})}{|\mathbf{r}-\mathbf{r'}|}d^3r' \tag{2.15}$$

This potential describes the Coulomb repulsion between the electron under consideration and the total electron density. It is here that the self-interaction problem becomes evident, as the electron is part of the total electron density, and as such this term involves an interaction between the electron and itself. This is unphysical, and is one of the aforementioned corrections included in the exchange-correlation potential.

The final potential, V_{XC}, can be defined as a functional derivative of the exchange-correlation

energy:

$$V_{\mathrm{XC}}(\mathbf{r}) = \frac{\delta E_{\mathrm{XC}}\big[n(\mathbf{r})\big]}{\delta n(\mathbf{r})} \tag{2.16}$$

To find a solution to equation 2.14, we must define the Hartree and exchange-correlation potentials, using the electron density. However, to find the electron density, we must know the single-electron wavefunctions, which can also be found from solving equation 2.14. It is in this way that the KS equations are considered to be self-consistent, and they must be solved iteratively:

1. An initial, trial electron density $n(\mathbf{r})$ is defined.
2. The KS equations are solved using $n(\mathbf{r})$ to find the KS states, $\Psi_i(\mathbf{r})$.
3. The electron density is calculated from the KS wavefunctions in Step 2, given by $n(\mathbf{r}) = \sum_i \Psi_i^*(\mathbf{r})\Psi_i(\mathbf{r})$.
4. The calculated electron density is compared with the trial electron density. If the two densities are equal (within a reasonable degree of accuracy), this is the ground-state electron density, which can then be used to calculate the total energy. However, if the two densities are different, the trial electron density must be altered and the process begins again.

2.3.4 The Exchange-Correlation Functional

Several approximations have been developed for the exchange-correlation functional. The two most common approximations are the local density approximation (LDA), proposed in the original Hohenberg and Kohn paper, and the generalised gradient approximation (GGA).[18] The simplest approximation is the LDA, which assumes that the exchange-correlation energy at a point $\mathbf{r}$ is the same as the exchange-correlation energy of a uniform electron gas

with the same density at point $\mathbf{r}$:

$$E_{\mathrm{XC}}\big[n(\mathbf{r})\big] = \int \varepsilon_{\mathrm{XC}}(\mathbf{r}) n(\mathbf{r}) d\mathbf{r} \tag{2.17}$$

with the assumption that the exchange-correlation energy is purely local:

$$\varepsilon_{\mathrm{XC}}(\mathbf{r}) = \varepsilon_{\mathrm{XC}}^{\mathrm{hom}}\big[n(\mathbf{r})\big] \tag{2.18}$$

Thus, the exchange-correlation potential V_{XC} can be written as:

$$V_{\mathrm{XC}}(\mathbf{r}) = \frac{\delta E_{\mathrm{XC}}\big[n(\mathbf{r})\big]}{\delta n(\mathbf{r})} \tag{2.19}$$

The most common parametrisation in use for $\varepsilon_{\mathrm{XC}}^{\mathrm{hom}}$ is based on quantum Monte-Carlo calculations on homogeneous electron gases at various densities.[19]

The LDA is particularly effective in solid-state physics, where metal electrons are often highly delocalised and can be well approximated by a free electron gas where the electron density varies slowly over space. However, the LDA ignores corrections to the exchange-correlation energy due to inhomogeneities in the electron density at point $\mathbf{r}$, and is known to overbind, particularly in molecules, where bonds are broken as opposed to simply being rearranged.

The GGA attempts to improve on the LDA by including the gradient of the electron density, and therefore it can be considered as a semi-local method. The GGA XC functional can be written as:

$$E_{\mathrm{XC}}^{\mathrm{GGA}}\big[n(\mathbf{r})\big] = \int n(\mathbf{r}) \varepsilon_{\mathrm{XC}}^{\mathrm{hom}}\big[n(\mathbf{r})\big] F_{\mathrm{XC}}\big[n(\mathbf{r}), \nabla n(\mathbf{r})\big] d\mathbf{r} \tag{2.20}$$

where $F_{\mathrm{XC}}\big[n(\mathbf{r}), \nabla n(\mathbf{r})\big]$ is the enhancement factor. There are several variations of this enhancement factor, giving different forms of the GGA, such as PBE[20] and PW91.[21] In general, the GGA has much more success when applied to molecules, and significantly reduces

overbinding.

2.3.5 Spin-polarised DFT

In the outline so far, there is an underlying assumption that there is no overall spin polarisation in the system. The HK theorems can be generalised to include the spin degrees of freedom, by replacing the electron density with a density matrix, where the one-to-one relationship between the external potential and the spin density is replaced by a relationship between the ground state many-body wavefunction and the density matrix.[22]

In most cases, it can be assumed that spins are collinear, which leads to two spin densities $n^{\uparrow}(\mathbf{r})$ and $n^{\downarrow}(\mathbf{r})$, where the overall electron density is given by the addition of these two terms, introducing the concept of the local spin density approximation (LSDA).

In contrast to non-spin polarised DFT, spin-polarised DFT yields multiple self-consistent solutions with different stable spin-densities. Therefore, to ensure that the global minimum is found, it may be necessary to start from a variety of initial spin densities by varying the spin moments applied to specific atoms.[23]

2.3.6 DFT+U

The study of transition metals also necessitates the extension of the LDA and GGA approximations due to the presence of highly localised and correlated d-electrons that vary rapidly over space.

Typically, both the LDA and GGA underestimate the band gaps of materials with localised electrons. To correct this, an additional term can be introduced, similar to that in the Hubbard model of tight-binding. The strength of the on-site interactions can be described by the parameters U and J, representing the Coulomb and exchange interactions, respectively. The parameters can be found by fitting to known experimental data or calculated

computationally.

The correction can be introduced in different ways,[24,25] with one common method involving the use of an effective parameter, U_{eff}:

$$U_{\text{eff}} = U - J \tag{2.21}$$

2.3.7 Basis Sets

The wavefunctions can be expanded using a basis set:

$$\Psi_i = \sum_{\alpha} c_\alpha \varphi_\alpha \tag{2.22}$$

There are a number of different basis sets available,[26] such as Slater type orbitals (STO) (usually expanded as Gaussians) and Gaussian type orbitals (GTO), which are classified as atomic orbitals. In this instance, the basis function exponentially decays to zero at large distances, and the orbitals are centred on atoms.

However, this is usually only applicable to isolated atoms and molecules, where the wavefunction also decays in the same manner. There is software available using atom centred basis sets for solid state systems (such as CRYSTAL14[27]), though for periodic systems, a plane wave basis set is more often used. The wavefunction can be written as a product of a function that is periodic in the cell lattice vectors, $\mathbf{R}$, such that:

$$\psi_k(\mathbf{r}) = e^{i\mathbf{kr}} u_k(\mathbf{r}) \tag{2.23}$$

where u_k is periodic in the cell lattice vectors:

$$u_k(\mathbf{r} + \mathbf{R}) = u_k(\mathbf{r}) \tag{2.24}$$

As $u_k(\mathbf{r})$ is periodic, it can be expanded in plane wave form:

$$u_k(\mathbf{r}) = \sum_{\mathbf{G}} c_{k,G} e^{i\mathbf{G}\cdot\mathbf{r}} \tag{2.25}$$

where $\mathbf{G}$ are reciprocal lattice vectors.

As a result, the wavefunction can be written as:

$$\psi_k(\mathbf{r}) = \sum_{\mathbf{G}} c_{k,G} e^{i(\mathbf{k}+\mathbf{G})\cdot\mathbf{r}} \tag{2.26}$$

As the sum over $\mathbf{G}$ is infinite sum, it must be truncated. This is usually done by imposing a kinetic energy cut-off, such that:

$$E_{\text{cut}} = \frac{|\mathbf{k}+\mathbf{G}|^2}{2} \tag{2.27}$$

Plane wave basis sets offer a number of advantages over STO and GTO. As plane waves do not depend on nuclear positions, corrections are not needed for force calculations as in the case of localised basis sets. In addition, the convergence can be easily verified by changing the energy cut-off.

Another aspect of convergence is based on the $\mathbf{k}$-point sampling, as the eigenenergies are found to vary with $\mathbf{k}$. Therefore, the convergence of the total energy depends on the system in question. There are a number of different $\mathbf{k}$-point sampling methods available, such as Monkhorst-Pack,[28] for choosing the $\mathbf{k}$-points and Gaussian smearing and Methfessel-Paxton,[29] for integrating over discrete $\mathbf{k}$-points and energies.

2.3.8 Pseudopotentials

As the KS wavefunctions approach the nucleus, they exhibit rapid oscillations to maintain orthogonality between valence and core electrons, requiring a large plane wave basis set to accurately represent them. This comes at a large computational expense, and as a result, the pseudopotential method[30] was developed to address this issue.

This method takes advantage of the fact that the oscillations cause the wavefunctions in these regions to be fairly insensitive to their chemical environment. This means that the core can be replaced with node-less wavefunctions, while still maintaining the long-range behaviour of the valence electron wavefunctions.[31] The rapid oscillations experienced in the core region of an atom by the valence electron wavefunctions become smoother outside of the core region. A pseudopotential can be added that reproduces wavefunctions with similar behaviour to all electron wavefunctions outside the core region, but with no nodes, outside of a specific cut off radius, r_c, as shown in Figure 2.3. This means that the system can now be described with a reasonably small number of plane waves.

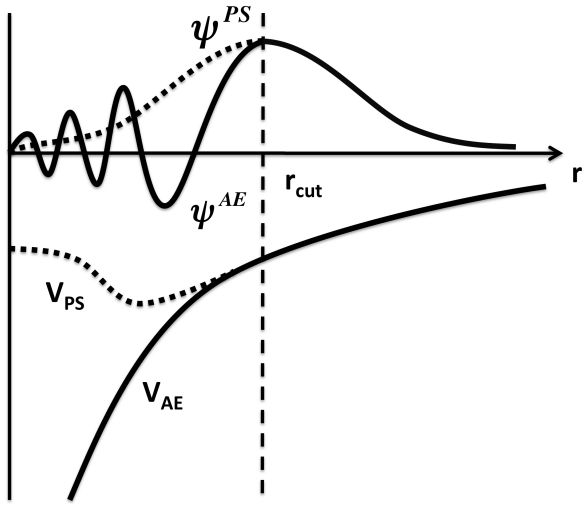

Figure 2.3: A comparison of a wavefunction in the Coulomb potential of the nucleus to the wavefunction in the pseudopotential. The real and pseudo wavefunction and potentials are the same above a cut-off radius, r_c.

In one approach to this issue, called the augmented wave method, the system is broken down into two types of region: the core region, near the atomic centre, and valence regions. In the core region, the wavefunction is defined by an atomic-like basis set, while in the valence region, another basis set can be used, such as plane waves.

The projector augmented wave (PAW) method combines the augmented wave and pseudopotential methods, where projectors are defined so that KS wavefunctions are transformed into functions that do not oscillate rapidly near the nucleus, which means that their expansion to plane waves is less complex. An inversion of this projection leads to the original KS wavefunctions, while still obtaining good results for observables.

2.4 General Software and Calculations

The General Utility Lattice Program (GULP)[32] was originally written to facilitate the fitting of interatomic potentials to energy surfaces and experimental data. It has since expanded to become a general purpose code for modelling solid state problems, and can perform a variety of tasks using forcefield calculations.

In this thesis, GULP is used to perform structure optimisation for a variety of structures. Specific details are given in each chapter regarding the optimisation scheme and other variables, as GULP allows for a lot of flexibility.

The DFT calculations in this thesis were computed using The Vienna Ab initio Simulation Package (VASP).[33] Using VASP, structure optimisation and spin-polarised DFT calculations were performed using the PAW method with plane-wave basis sets.

The DFT calculations in Chapters 4, 5 and 6 were all performed in the same manner. In each case, a cut-off energy of 550 eV was used and geometries were relaxed until all forces were less than 0.01 eV Å^{-1}. A Γ-centered **k**-point grid was used for each calculation, where the number of **k**-points in each direction was set to the lowest number to satisfy the condition:

real-space lattice vector (Å) × **k**-points on lattice vector ≥ 20. Finally, all relaxations were performed without symmetry constraints.

Other software used throughout includes:

- FINDSYM,[34] which can identify the space group of a crystal given the positions of atoms in the unit cell.
- VESTA,[35] a 3D visualisation program that can also compute volumetric data such as electron density.
- ASE,[36] an atomic simulation environment written in Python to facilitate atomistic simulations.

Calculations themselves were performed on a number of different computers. The University of Liverpool provides high-performance computing facilities, and the majority of forcefield calculations were performed in batch jobs on these resources.

Access to the UK's supercomputer ARCHER (and previously HECToR) was provided both through membership of the UK's HEC Materials Chemistry Consortium, funded by EPSRC (EP/L000202) and a PRACE-3IP project (FP7 RI-312763). The majority of DFT calculations were performed using these resources.

2.5 Reference Texts

- "A Chemist's Guide to Density Functional Theory" (2nd Edition), W. Koch and M. C. Holthausen, 2001, Wiley
- "A bird's eye view of density-functional theory", K. Capelle, Brazilian Journal of Physics 36 (4A), 2006, p. 1318-1343
- "Computational Chemistry and Molecular Modeling: Principles and Applications",

K.I. Ramachandran, G. Deepa and K. Namboori, 2008, Springer-Verlag Berlin Heidelberg

- "Introduction to Computational Chemistry" (2nd Edition), F. Jensen, 2011, Wiley
- "Introduction to Solid State Physics" (8th Edition), C. Kittel, 2004, Wiley

References

1. Payne, M. C., Teter, M. P., Allan, D. C. & Arias, T. A. Iterative minimization techniques for *ab initio* total-energy calculations: molecular dynamics and conjugate gradients. *Reviews of Modern Physics* **64,** 1045–1097 (4 1992).

2. Polak, E. *Computational Methods in Optimisation* (Academic Press, New York, 1970).

3. Joseph-Frédéric, B., Gilbert, C. J., Lemarechal, C. & Sagastizábal, C. A. *Numerical Optimization: Theoretical and Practical Aspects* (Springer-Verlag Berlin Heidelberg, 2006).

4. Press, W. H., Teukolsky, S. A., Vetterling, W. T. & Flannery, B. P. *Numerical Recipes: The Art of Scientific Computing* 3rd (Cambridge University Press, New York, 2007).

5. Halicioğlu, T. & Pound, G. M. Calculation of potential energy parameters form crystalline state properties. *Physica Status Solidi (a)* **30,** 619–623 (1975).

6. Girifalco, L. A. & Weizer, V. G. Application of the Morse potential function to cubic metals. *Physical Review* **114,** 687–690 (3 1959).

7. Frenkel, D. & Smit, B. *Understanding molecular simulation: from algorithms to applications* (Elsevier, 2002).

8. Wolf, D., Keblinski, P. & Phillpot, S. R. Exact method for the simulation of Coulombic systems by spherically truncated, pairwise r^{-1} summation. *The Journal of Chemical Physics* **110,** 8254–8282 (1999).

9. Dick, B. G. Jr & Overhauser, A. W. Theory of the dielectric constants of alkali halide crystals. *Physical Review* **112,** 90–103 (1 1958).

10. *Database of Published Interatomic Potential Parameters* `http://www.ucl.ac.uk/klmc/Potentials/`. Accessed: September 2016.

11. *Interatomic Potentials Repository Project* `http://www.ctcms.nist.gov/potentials/`. Accessed: September 2016.

12. Becker, C. A., Tavazza, F., Trautt, Z. T. & de Macedo, R. A. B. Considerations for choosing and using force fields and interatomic potentials in materials science and engineering. *Current Opinion in Solid State and Materials Science* **17,** 277–283 (2013).

13. Hill, J. R., Freeman, C. M. & Subramanian, L. *Use of force fields in materials modeling* 141–216 (John Wiley Sons, Inc., 2000).

14. Parr, R. G. in *Horizons of Quantum Chemistry: Proceedings of the Third International Congress of Quantum Chemistry Held at Kyoto, Japan, October 29 - November 3, 1979* (eds Fukui, K. & Pullman, B.) 5–15 (Springer Netherlands, Dordrecht, 1980).

15. Kohn, W., Becke, A. D. & Parr, R. G. Density functional theory of electronic structure. *The Journal of Physical Chemistry* **100,** 12974–12980 (1996).

16. Hohenberg, P. & Kohn, W. Inhomogeneous electron gas. *Physical Review* **136,** B864 (1964).

17. Kohn, W. & Sham, L. J. Self-consistent equations including exchange and correlation effects. *Physical Review* **140,** A1133 (1965).

18. Perdew, J. Accurate density functional for the energy: Real-space cutoff of the gradient expansion for the exchange hole. *Physical Review Letters* **55,** 1665–1668 (1985).

19. Perdew, J. P. & Zunger, A. Self-interaction correction to density-functional approximations for many-electron systems. *Physical Review B* **23,** 5048–5079 (10 1981).

20. Perdew, J., Burke, K. & Ernzerhof, M. Generalized Gradient Approximation Made Simple. *Physical Review Letters* **77,** 3865–3868 (1996).

21. Perdew, J. *et al.* Atoms, molecules, solids, and surfaces: Applications of the generalized gradient approximation for exchange and correlation. *Physical Review B: Condensed Matter* **46,** 6671–6687 (1992).

22. Von Barth, U. & Hedin, L. A local exchange-correlation potential for the spin polarized case. i. *Journal of Physics C: Solid State Physics* **5,** 1629–1642 (1972).

23. Singh, D. J. & Nordstrom, L. *Planewaves, Pseudopotentials, and the LAPW method* 2006.

24. Liechtenstein, A. I., Anisimov, V. I. & Zaanen, J. Density-functional theory and strong interactions: Orbital ordering in Mott-Hubbard insulators. *Physical Review B* **52,** R5467–R5470 (8 1995).

25. Dudarev, S. L., Botton, G. A., Savrasov, S. Y. & Humphreys, C. J. Electron-energy-loss spectra and the structural stability of nickel oxide: An LSDA+ U study. *Physical Review B* **57,** 1505–1509 (1998).

26. Boese, A. D., Martin, J. M. L. & Handy, N. C. The role of the basis set: Assessing density functional theory. *The Journal of Chemical Physics* **119,** 3005–3014 (2003).

27. Dovesi, R. *et al.* C RYSTAL14: A program for the *ab initio* investigation of crystalline solids. *International Journal of Quantum Chemistry* **114,** 1287–1317 (2014).

28. Monkhorst, H. J. & Pack, J. D. Special points for Brillouin-zone integrations. *Physical Review B* **13,** 5188–5192 (1976).

29. Methfessel, M. & Paxton, A. High-precision sampling for Brillouin-zone integration in metals. *Physical Review B: Condensed Matter* **40,** 3616–3621 (1989).

30. Blöchl, P. E. Projector augmented-wave method. *Physical Review B* **50,** 17953–17979 (1994).

31. Phillips, J. C. Energy-band interpolation scheme based on a pseudopotential. *Physical Review* **112,** 685–695 (1958).

32. Gale, J. D. GULP: A computer program for the symmetry-adapted simulation of solids. *Journal of the Chemical Society, Faraday Transactions* **93,** 629–637 (1997).

33. Kresse, G. & Furthmüller, J. Efficient iterative schemes for ab initio total-energy calculations using a plane-wave basis set. *Physical Review B* **54,** 11169–11186 (1996).

34. Stokes, H. T. & Hatch, D. M. FINDSYM: program for identifying the space-group symmetry of a crystal. *Journal of Applied Crystallography* **38,** 237–238 (2005).

35. Momma, K. & Izumi, F. VESTA: a three-dimensional visualization system for electronic and structural analysis. *Journal of Applied Crystallography* **41,** 653–658 (2008).

36. Bahn, S. R. & Jacobsen, K. W. An object-oriented scripting interface to a legacy electronic structure code. *Computing in Science and Engineering* **4,** 56–66 (2002).

Chapter 3

Development of Search Methods

This chapter provides an outline of the methods developed and implemented in this thesis, building on work discussed in Chapter 1 and applying the theoretical models described in Chapter 2.

3.1 Extended Module Materials Assembly

The Extended Module Materials Assembly (EMMA) approach, developed at the University of Liverpool, combines data centred methods with quantum mechanical techniques.[1] It works on the basic principle of using module sets to generate candidate structures, building on the data mining techniques described in Chapter 1. This is briefly summarised in Figure 3.1 below, where the long-range ordering of cubic perovskite structures can be broken down into the constituent modules.

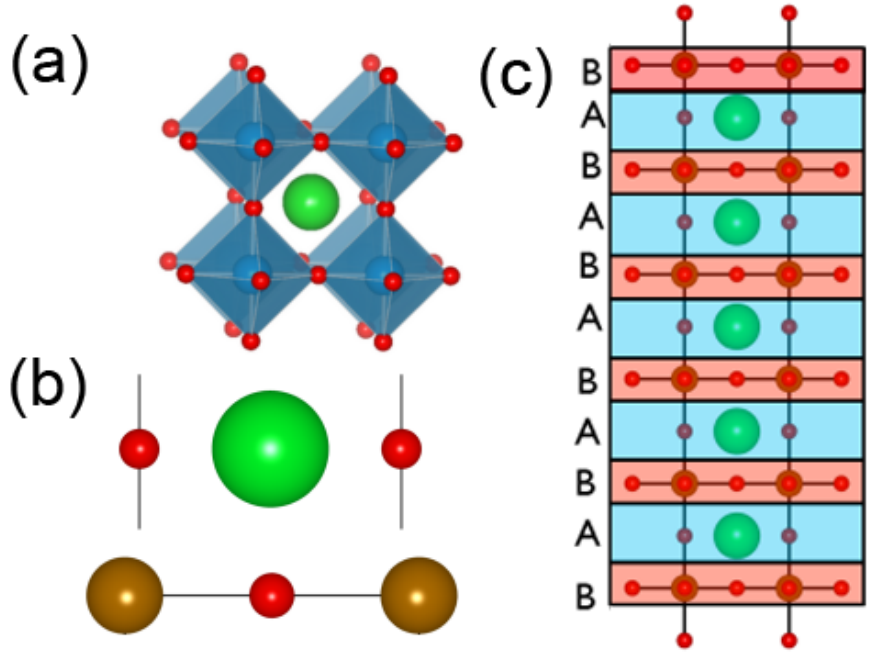

Figure 3.1: The principle of module sets as demonstrated by long range ordering of cubic perovskite structures. The general perovskite structure is shown in (a) with formula ABO_3, the module sets of AO and BO_2 are shown in (b) and (c) demonstrates the stacking of layers in the [001] direction

3.1.1 Polysomatism

Although it is common to consider a crystal structure on an atom-by-atom basis, it is also useful to consider units of larger modules, particularly if there are many atoms present in the unit cell. For example, coordination polyhedra simplify the visualisation of many complex structures and allow for easier interpretation.[2] From this fundamental concept, Thompson formulated 'polysomatism' derived from the ancient Greek for many-bodied, to describe the theory of building structures from chemically distinct modules that can occur in different proportions in different crystals.

The concept of polysomatism is readily visualised using building blocks. Each building block contains a distinct chemical environment, and these particular building blocks can be stacked to give a specific structure.[3] In converse, one can also imagine a situation whereby a structure is sliced into its component parts.

Thus, the initial building of the candidate structures can be visualised using 'lego' blocks, or slabs. This can be seen below in Figure 3.2, where the step following the initial construction involves assessing the candidate structures by removing repeated structures.

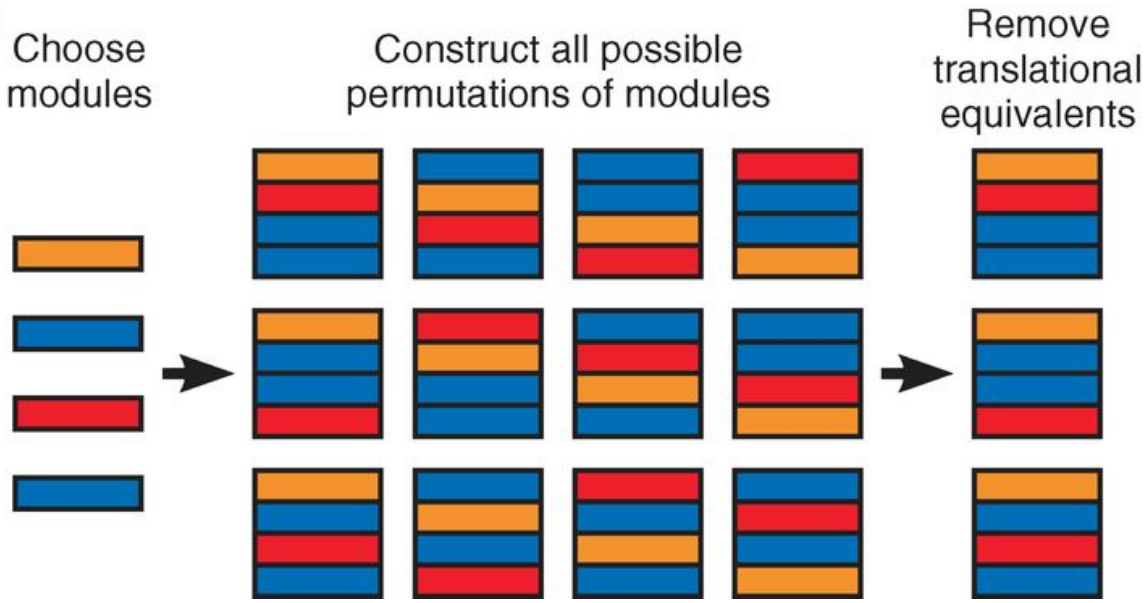

Figure 3.2: A visual representation of how candidate structures are built.[1]

3.1.2 Perovskites

The are several structural families that can be described in terms of layers, such as mineral families, hexaferrites and the diverse perovskite family. The work in this thesis primarily focuses on the pervoskite families, described below.

Cubic Perovskites

The perovskite structure has the ideal formula ABX_3, based on the crystal structure of calcium titanium oxide, $CaTiO_3$, as shown in Figure 3.3. A and B are cations that have a large size difference, with A being the larger cation and B the smaller. The anion, X, bonds to both.

The structure can accommodate most of the metallic ions in the periodic table, including the larger rare-earth metals such as the lanthanides. Most commonly, the anion takes the form of oxide or fluoride, but perovskites exist with the heavier halides and hydrides, amongst other anions. Therefore, as a family of compounds, the physical properties exhibited vary greatly, and perovskite compounds are often used in applications ranging from solid oxide fuel cells (SOFCs) to radioactive waste containment.

In the ideal form, the structure of cubic ABX_3 can be described in terms of corner sharing BX_6 octahedra. The BX_6 octahedra share corners infinitely in all three dimensions, resulting in a symmetric structure. The A cations occupy the holes created by eight BX_6 octahedra, giving the A cation a 12-fold oxygen coordination, and the B cation a 6-fold oxygen coordination. This ideal structure is observed in $SrTiO_3$,[4] shown in Figure 3.3.

However, many distortions from the idealised perovskite structure are known. Both $CaTiO_3$,[5] from which the structure was originally derived, and $GdFeO_3$,[6] comprise of tilted BO_6 octahedra, also shown in Figure 3.3. This is the most common variation of the perovskite structure, occurring when the A-site cation is too small for the cavities created in the octahedra network.

Several other distortions are known, and some occur in conjunction with others. Distortions due to Jahn-Teller effects can also occur, as seen in $CaCu_3Ti_4O_{12}$[7] where three-quarters of the A cation sites become square planar. This effect is exclusively seen when the A sites are filled by Jahn-Teller ions such as Cu^{2+} and Mn^{3+}. As an illustration of the complexity of the distortion that can be present in the perovskite structure, $BaTiO_3$[8] undergoes numerous phase transitions at different temperatures. It has a rhombohedral ($R3m$) structure at at temperatures below 90°C, and on heating becomes orthorhombic ($Amm2$), tetragonal ($P4mm$) and cubic ($Pm\bar{3}m$).

One can also describe perovskite layers as based on the stacking of hexagonal $[AX_3]$ layers. The $[AX_3]$ layers result from replacing the X anions with A cations of a similar size in $[X_4]$

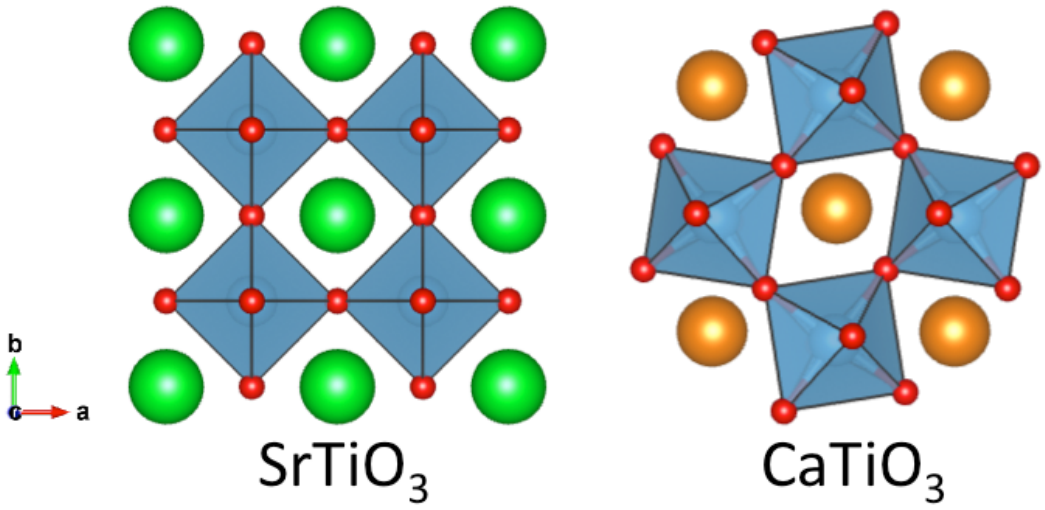

Figure 3.3: The structures of $SrTiO_3$ and $CaTiO_3$ where Sr^{2+} and Ca^{2+} are shown by the green and orange spheres, respectively. The TiO_6 octahedra are shown in blue.

anionic layers. The layers stack in a cubic arrangement (-ABCA-), and the B cations occupy the octahedral holes formed by the X anions, giving rise to the formula ABX_3.[9]

Hexagonal Perovskites

Among the perovskite related structures, hexagonal perovskites exhibit a structure that is also characterised by close packing of AX_3 layers, but differ due to the introduction of the hexagonal stacking sequence (-AB-), shown below in Figure 3.4. Therefore, a hexagonal perovskite comprises both hexagonal and cubic AX_3 stacking sequences, which can be described using the Jagodzinski notation. In this notation, a layer in the sequence is denoted h or c depending on whether its neighbouring layers are the same or different. The mixed sequences in the stacking arrangement results in the appearance of BX_6 face-sharing octahedra.[10]

Therefore, close-packed lattices can be readily broken down into layers that are related by specific stacking rules. Translating a layer A by in-plane translations of (1/3, 2/3) and (2/3, 1/3) along the hexagonal cell vectors results in two layers B and C respectively. These layers can then be stacked in the out-of-plane direction in any order, as long as no layer is directly

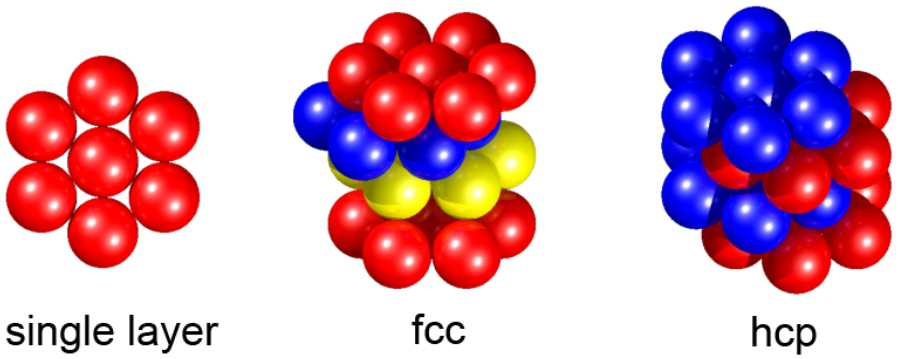

Figure 3.4: A comparison of fcc and hcp stacking, which can be used to create hexagonal pervoskite structures.

stacked upon itself. Commonly observed stacking sequences involve alternating A and B layers, and cubic close-packing in which the sequence ABC is periodically repeated, demonstrated in Figure 3.4 in a fcc unit cell. However, as stated above, any sequence is theoretically possible and many other sequences are observed in known crystal structures.

It is possible to enumerate the number of unique stacking sequences by taking into account the individual layers A, B and C and the stacking sequence that connects them, for any given stacking length within limits. Often, limiting factors are the number of unique stacking sequences or the size of the structures generated. It is from this principle that the EMMA method was conceived, with the original work outlined in the section below.

3.1.3 Original EMMA with Cubic Stacking

In the EMMA approach, a set of candidate structures is generated using 3D building blocks combined in different permutations. Translational equivalents are removed so that structures are not repeated. Following this, an initial screening is completed using force field optimisation. Finally, the most promising structures from the initial screening are relaxed using density functional theory. These steps are summarised below in Figure 3.5.

EMMA was developed to assist with the design of functional inorganic materials, focusing initially on cubic perovskite materials that had the potential for use in solid oxide fuel cells,

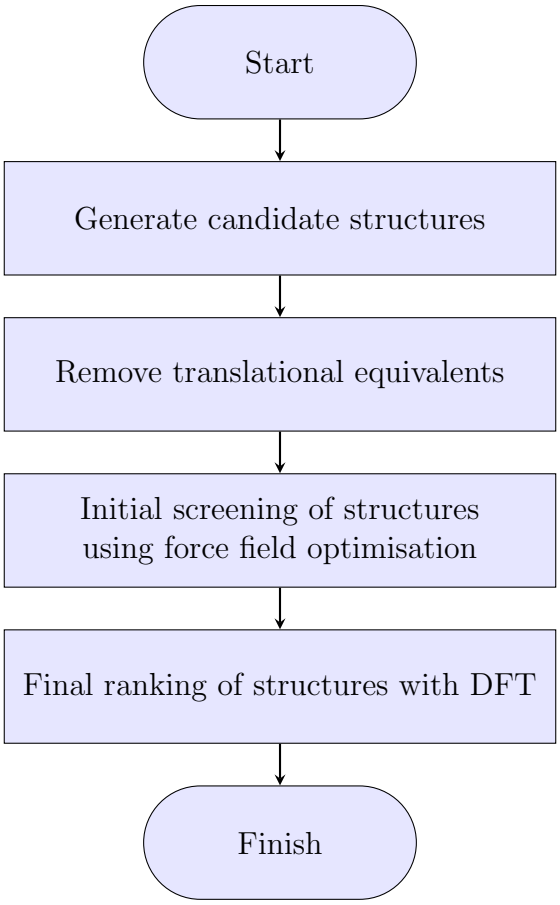

Figure 3.5: Block scheme of the EMMA method.

using $YBa_2CaFe_5O_{13}$ as a starting point to validate the approach. After generating 14,190 candidate structures with the desired composition, EMMA was able to find the experimental structure as the lowest energy structure, as shown below in Figure 3.6.

Following this, EMMA was used to identify a new material with improved performance as a SOFC cathode, using cation substitution to increase electronic conductivity. EMMA was able to identify a candidate structure of $Y_2Ba_2Ca_4Fe_{7.5}Cu_{0.5}O_{21}$ that was significantly more stable than the other structures. This structure was then experimentally realised* and confirmed through structure refinement techniques, with the desired enhanced electronic conductivity.

*The experimental work was carried out at the University of Liverpool within the group of Professor Matthew J. Rosseinsky.

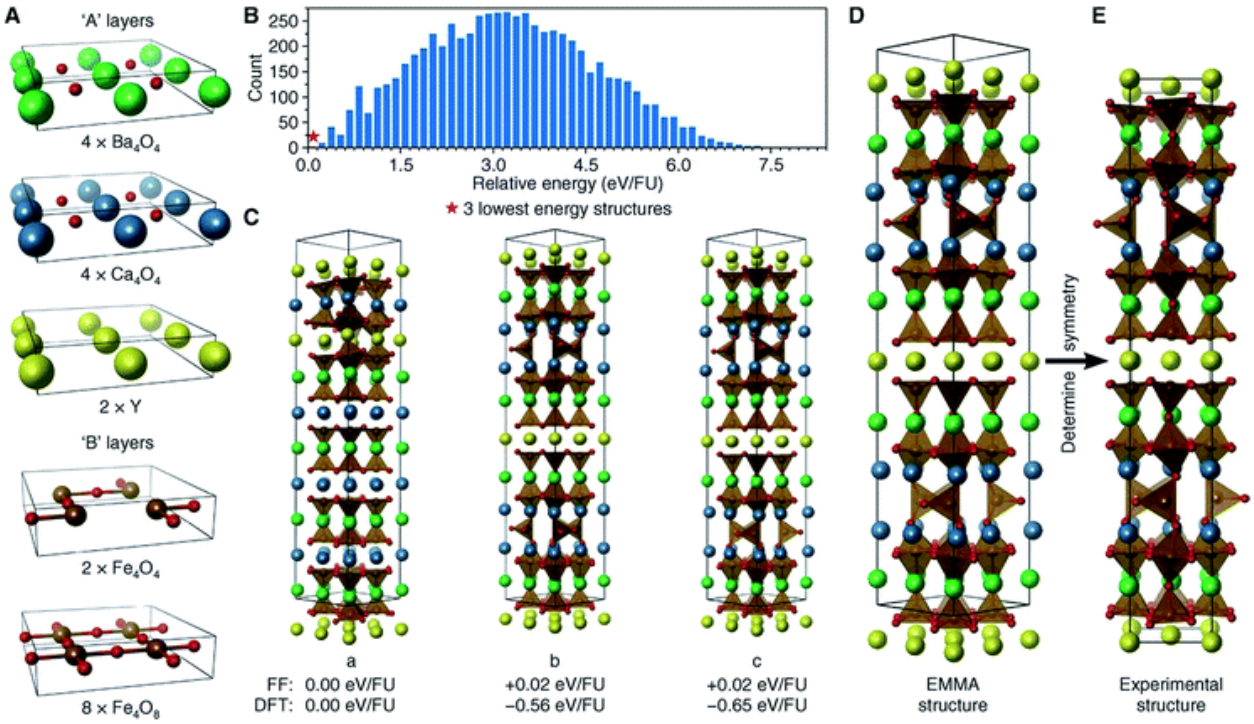

Figure 3.6: Reproducing the structure of $YBa_2Ca_2Fe_5O_{13}$ via EMMA. (A) The layer modules. (B) A histogram showing the force-field energies of all candidate structures. (C) The three lowest-energy polysomes predicted from initial force-field calculations, together with their force-field and DFT relative energies. (D) The final polysome predicted via EMMA. (E) The refined experimental structure. Atoms are coloured as follows: yellow, Y; green, Ba; blue, Ca; brown, Fe; and red, O.

The work in this thesis aims to expand the types of compounds investigated via the EMMA approach, assisting in the identification and synthesis of desired compounds.

3.1.4 Extension to Hexagonal Stacking

EMMA enables the bulk generation of all possible structures in two ways, either by imposing charge neutrality on a given stacking length or limiting the composition and specific atom numbers. Since EMMA is written in the Python programming language, it can be extended to facilitate the generation of candidate structures, for example by generating all candidate structures for a range of stacking lengths.

For a given stacking length, the possible choices of A, B and C are constructed. A permutation is removed if over half of one layer type is present, since this would mean that one layer

type would have to directly stack upon itself, in addition to removing sequences that include two or more identical neighbouring layers. Translational equivalents are also removed so that sequences are not repeated, for example by shifting the sequence up or down.

Finally, sequences related to others by any combination of the three symmetry operations identified by McLarnan[11] are identified and removed. These symmetry operations are

- reversing a sequence (e.g. ABCAB = BACBA)
- exchanging all B layers for C layers and vice versa (e.g. ABCAB = ACBAC)
- permuting the layers from A to B, B to C, C to A, and A to C, B to A, C to B (e.g. ABCAB = BCABC = CABCA)

As a result, only the symmetrically unique layer sequences for a given stacking length are chosen, $S_{\min}$, as shown in Figure 3.7 (b).

Following the construction of the stacking sequence, it is necessary to populate both the close-packed lattice and interstitial sites with specific atom types. The layers are originally entered into EMMA as untranslated lattice layers, A_i, which are then translated to the B_i and C_i layers as described earlier. Every possible of permutation is generated by substituting each specific layer into the sequence $S_{\min}$. For example, if two different lattice layers are used, A_1 and A_2, then eight lattices would be constructed for the general sequence ABC: $A_1B_1C_1$, $A_2B_1C_1$, $A_1B_2C_1$, ..., $A_2B_2C_2$.

Following the construction of the close-packed lattice, the interstitial sites are occupied. Possible interstitial layers, α_j, which lie between the B and C layers are identified. The interstitial layers that lie between C and A, β_j and A and B, γ_j are generated from in-plane translations of α_j, as in the case of the close-packed lattice. The interstitial layers that lie between a reversed stacking sequence are constructed by reflecting the interstitial layer in a mirror plane perpendicular to the stacking direction, for example, α_j^* lying between C and B layers. The permutations are then generated from the chosen interstitial layers, for example, if two different interstitial layers, α_1 and α_2 are used, then eight structures would be generated from

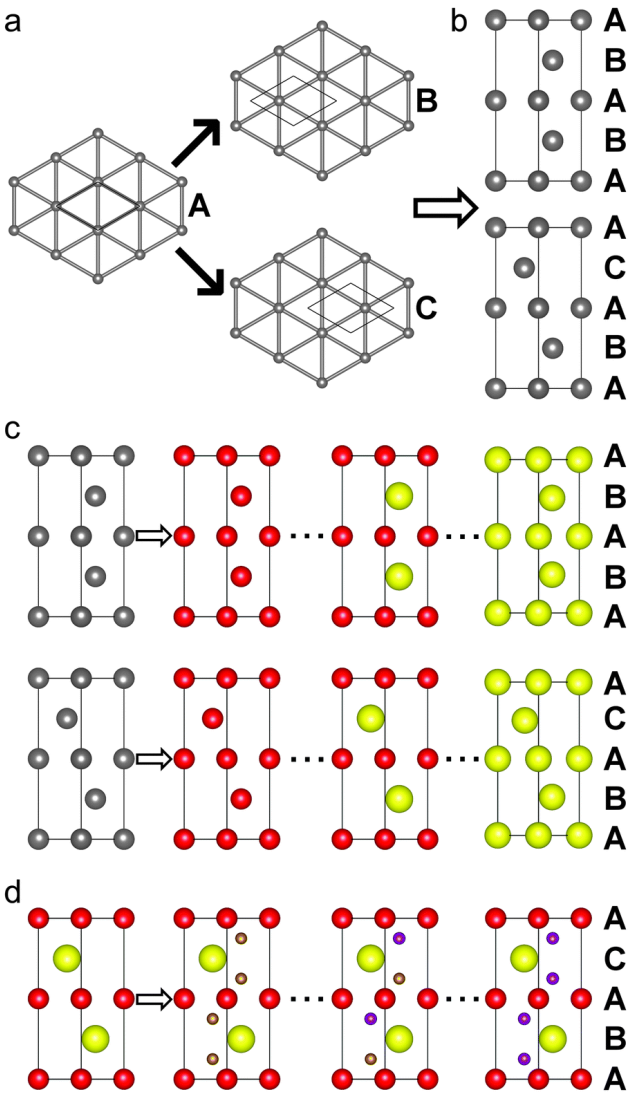

Figure 3.7: (a) The three layers, A, B and C, which are used to construct close packed lattices, with the unit cell represented by the black square. (b) The two symmetrically unique stacking sequences for a repeat length of four layers. (c) Decorating the two stacking sequences with red and yellow lattice layers, representing different compositions leads to a total of $2 \times 16 = 32$ structures. (d) Inserting interstitial layers into each decorated lattice, choosing from green or blue compositions, results in $32 \times 16 = 512$ structures.

the lattice $A_1B_1C_1$: $A_1\gamma_1B_1\alpha_1C_1\beta_1, A_1\gamma_2B_1\alpha_1C_1\beta_1, A_1\gamma_1B_1\alpha_2C_1\beta_1, \ldots, A_1\gamma_2B_1\alpha_2C_1\beta_2$. Therefore, a total of 64 structures from the general sequence ABC decorated with the two lattice layers A_1 and A_2.

3.1.5 Identification of Promising Structures

Once the candidate structures have been generated, the next task is to identify the most promising structures. Based on the combination of module sets and stacking length, thousands of candidate structures could potentially be constructed, and therefore it is imperative that structures are efficiently evaluated.

As described in Chapter 2, there is a compromise between accuracy and speed in computational calculations. EMMA takes advantage of this by employing two methods: an initial screening with forcefield calculations followed by a more accurate DFT calculation for the final energy ranking.

The forcefield screening allows for the evaluation of thousands of structures, though at the cost of accuracy. For example, in the initial EMMA study, three structures were found to be far more stable than the other structures and very similar in energies to one another at the FF stage. However, in the final energy ranking, the experimental structure was found to be more stable than the second most stable structure by approximately 0.1 eV/FU.

Other options exist for the initial screening. Forcefield optimisation was chosen due to the availability of parameters for a wide variety of ions. However, it is possible to apply other methods, such as tight binding[12] or chemical intuition, such as inspection of coordination environments and bonding.

Indeed, it is also possible to imagine other methods for the final ranking stage, with *ab initio* calculations again being more expensive computationally but more accurate. Therefore, the EMMA process draws its strength from its versatility, as steps in the process could be adapted for specific compounds. The following two chapters will explore the strengths and weaknesses of the EMMA method as applied to a new family of hexagonal perovskites.

3.2 Monte Carlo Site Swapping

Monte Carlo (MC) is a common name given to a wide variety of stochastic techniques, which all make use of random numbers and probability to investigate problems ranging from physics to economics. In materials science, several examples of Monte Carlo methods include:

- 'classical' Monte Carlo, in which samples are drawn from a probability distribution (such as the Boltzmann distribution) to obtain thermodynamic properties and minimum energy structures
- 'quantum' Monte Carlo, where random walks are used to calculate quantum-mechanical energies, using the Schrödinger equation as a starting point
- 'kinetic' Monte Carlo, whereby processes are simulated at different rates

There are two key implementations of Monte Carlo: the first, termed Metropolis Monte Carlo, generates configurations according to a desired statistical distribution. However, since there is no time dependence, this method cannot be used to study how the system evolves. The second can address kinetics, and as such is called Kinetic Monte Carlo. It uses transition rates that are dependent on the energy barrier between the states, with time increments chosen to relate to the microscopic kinetics of the system.

3.2.1 Metropolis Monte Carlo

To address the global optimisation problem, we are primarily concerned with the former implementation: Metropolis Monte Carlo, since it allows for the sampling of multidimensional space. In this instance, the multidimensional space sampled is the energy landscape, with the probability density, ρ^{eq} set by an equilibrium ensemble (such as the canonical, the isothermal-isobaric and grand canonical ensembles). The sampled configuration states form a Markov chain, with each state forming from the previous state following a MC step.

In the original algorithm, a MC step proceeds in two stages. The first involves a change from the current (or old) state, i into a new state j with probability $\alpha(i \to j)$, satisfying the condition:

$$\alpha(i \to j) = \alpha(j \to i) \tag{3.1}$$

The attempted move is then accepted or rejected based on the probability:

$$P_{\text{accept}}(i \to j) = \min\left[1, \frac{\rho^{\text{eq}}(j)}{\rho^{\text{eq}}(i)}\right] \tag{3.2}$$

If the move is rejected, state i is retained. This also means that the condition of detailed balance is satisfied, such that:

$$\rho^{\text{eq}}(i)P(i \to j) = \rho^{\text{eq}}(j)P(j \to i) \tag{3.3}$$

In the production phase of a MC simulation, each state i is sampled with a frequency proportional to its equilibrium probability density, $\rho^{\text{eq}}(i)$. This is known as importance sampling, and arises from the fact that the generated Markov chain asymptotically samples the probability distribution ρ^{eq}.

3.2.2 Implementation

A typical Monte Carlo algorithm making use of the Metropolis method is usually implemented in the following way:[13]

1. Choose the initial configuration of the system and calculate the energy
2. Loop through the atoms. For each atom, choose a random displacement, such as $d = (\text{random number} - 0.5) \times d_{\max}$ for the x, y and z coordinations. In this case, $d_{\max}$

is the maximum displacement, and the random number generated is between 0 and 1.

3. Calculate the energy change, ΔU, due to this displacement

4. Decide whether to accept the move based on the Metropolis criterion: if $\Delta U < 0$, then the new configuration is accepted if $\Delta U > 0$ calculate $W = \exp\left(-\frac{\Delta U}{kT}\right)$

5. A random number R is drawn between 0 and 1, and if $W > R$ then the new configuration should be accepted. Otherwise, the old configuration is retained.

   If the atom is retained at its old position, the old configuration is recounted as a new state

6. The next atom is chosen. If the number of MC cycles is less than the maximum number of cycles, repeat from step 2.

In theory, step 2 could be modified for the specific system in question. For example, the change to the system could also involve modifications to the unit cell size and shape. In this thesis, a Monte Carlo scheme is applied in such a way where ions are swapped between sites to investigate a novel system $(x)\mathrm{LiMgPO_4} + (1-x)\mathrm{Li_2MgSiO_4}$, as described in Chapter 6.

References

1. Dyer, M. S. *et al.* Computationally Assisted Identification of Functional Inorganic Materials. *Science* **340,** 847–852 (2013).

2. Thompson, J. B. Biopyriboles and polysomatic series. *American Mineralogist* **63,** 239–249 (1978).

3. Veblen, D. R. Polysomatism and polysomatic series; a review and applications. *American Mineralogist* **76,** 801–826 (1991).

4. Brous, J., Fankuchen, I. & Banks, E. Rare earth titanates with a perovskite structure. *Acta Crystallographica* **6,** 67–70 (1953).

5. Sasaki, S., Prewitt, C. T., Bass, J. D. & Schulze, W. A. Orthorhombic perovskite $CaTiO_3$ and $CdTiO_3$: structure and space group. *Acta Crystallographica Section C: Crystal Structure Communications* **43,** 1668–1674 (1987).

6. Geller, S. Crystal Structure of Gadolinium Orthoferrite, $GdFeO_3$. *The Journal of Chemical Physics* **24,** 1236–1239 (1956).

7. Bozin, E. S. *et al.* Temperature dependent total scattering structural study of $CaCu_3Ti_4O_{12}$. *Journal of Physics: Condensed Matter* **16,** S5091–S5102 (2004).

8. Ravel, B., Stern, E. A., Vedrinskii, R. I. & Kraizman, V. Local structure and the phase transitions of $BaTiO_3$. *Ferroelectrics* **206,** 407–430 (1998).

9. Katz, L. & Ward, R. Structure relations in mixed metal oxides. *Inorganic Chemistry* **3,** 205–211 (1964).

10. Darriet, J. & Subramanian, M. A. Structural relationships between compounds based on the stacking of mixed layers related to hexagonal perovskite-type structures. *Journal of Materials Chemistry* **5,** 543–552 (1995).

11. Müller, U. *Symmetry relationships between crystal structures : applications of crystallographic group theory in crystal chemistry.* (Oxford : Oxford University Press, 2013., 2013).

12. Koskinen, P. & Mäkinen, V. Density-functional tight-binding for beginners. *Computational Materials Science* **47,** 237–253 (2009).

13. Allan, N. in. *Chemical Thermodynamics of Materials* (eds Stølen, S. & Grande, T.) 337 –377 (John Wiley, 2003).

Chapter 4

Reported and predicted structures of $Ba(Co,Nb)_{1-\delta}O_3$ hexagonal pervoskite phases

Abstract

The Extended Module Materials Assembly computational method for structure solution and prediction has been implemented for hexagonal lattices. Exploring the family of B-site deficient materials in hexagonal perovskite barium cobalt niobates, it is found that the EMMA procedure returns the experimental structures as the most stable for the known compositions of $Ba_3CoNb_2O_9$, $Ba_5Nb_4O_{15}$ and $Ba_8CoNb_6O_{24}$. The unknown compositions $Ba_{11}Co_2Nb_8O_{33}$ and $Ba_{13}CoNb_{10}O_{39}$, having longer stacking sequences, are predicted to form as intergrowths of $Ba_3CoNb_2O_9$ and $Ba_5Nb_4O_{15}$, and are found to have similar stability to pure $Ba_3CoNb_2O_9$ and $Ba_5Nb_4O_{15}$, indicating that it is likely they can be synthesised.

Published: Phys. Chem. Chem. Phys., 2014, 16, 21073-21081.[1]

4.1 Introduction

As discussed in Chapter 3, complex perovskite structures are a diverse family of compounds, and their compositional flexibility allows them to be modified to yield multiproperty functional materials.[2] Two possible strategies to achieve this aim are cation order[3,4] and stacking variants of the pseudo close packed AO_3 layers.[5] In the archetypal perovskite, these layers are stacked in a cubic manner along [111].

The mixed stacking sequences are often associated with B site vacancies in hexagonally packed layers,[6] and alternative descriptions relate these structures to the many structures derived from pervoskite via crystal shear.[7] Structures produced via both these containing high valent d^0 cations have received significant attention as dielectric materials, for example, $Ba_3ZnTa_2O_9$ (BZT),[8] is a high-Q dielectric material used in microwave resonators. Here, cation ordering along the close-packed [111] direction of the cubic perovskite, produces a trigonal structure for BZT with purely cubic staking, as shown in Figure 4.1 (a). Niobium-based analogues of BZT such as $Ba_3ZnNb_2O_9$ (BZN)[9] and $Ba_3CoNb_2O_9$, (BCN)[10] have also been studied due to their lower cost.

B-site deficient hexagonal perovskite materials have also been investigated with the structural formula $A_nB_{\delta-1}O_{3n}$. $Ba_8ZnTa_6O_{24}$, with the B site occupied by Zn^{2+} and Ta^{5+} ions, while $n = 8$ and $\delta = 1$, was found to have excellent dielectric properties.[11] Its structure has mixed cubic (c) and hexagonal (h) stacking of the BaO_3 layers,[12] in the sequence $(hccc)_2$, in the Jagodzinski notation discussed in Chapter 3. The B site octahedra are corner sharing either side of a c layer and face sharing either side of a h layer, which means that the cation vacancies occur in the face sharing octahedra, demonstrated in Figure 4.1 (d). The compound $Ba_8CoTa_6O_{24}$ is found to be isostructural.

However, the compound $Ba_8CoNb_6O_{24}$ adopts a different *ccchhccc* stacking motif, with long-range ordering of the Co^{2+} cations, leaving a layer of vacant octahedral sites between

the *hh* stacked layers, as seen in 4.1 (c).[13] With a vacant layer at the *hh* boundary, all octahedra in the stacking sequence are corner sharing. This structure is part of a family of which $Ba_5Nb_4O_{15}$ ($n = 5$, $\delta = 1$) is also a member, with a *hhccc* stacking sequence. The vacant B-site layer arises from the electrostatic repulsion from the highly charged Nb^{5+} cations, shown by Figure 4.1 (b).[14] Several further members of the hc_n and hhc_n series have been studied. Members of the former series are referred to as twin structures, as they can be viewed as [111] twins of the parent cubic perovskite, whereas members of the latter are referred to as shift structures due to their being derived from [111] crystal shear of the parent perovskite.

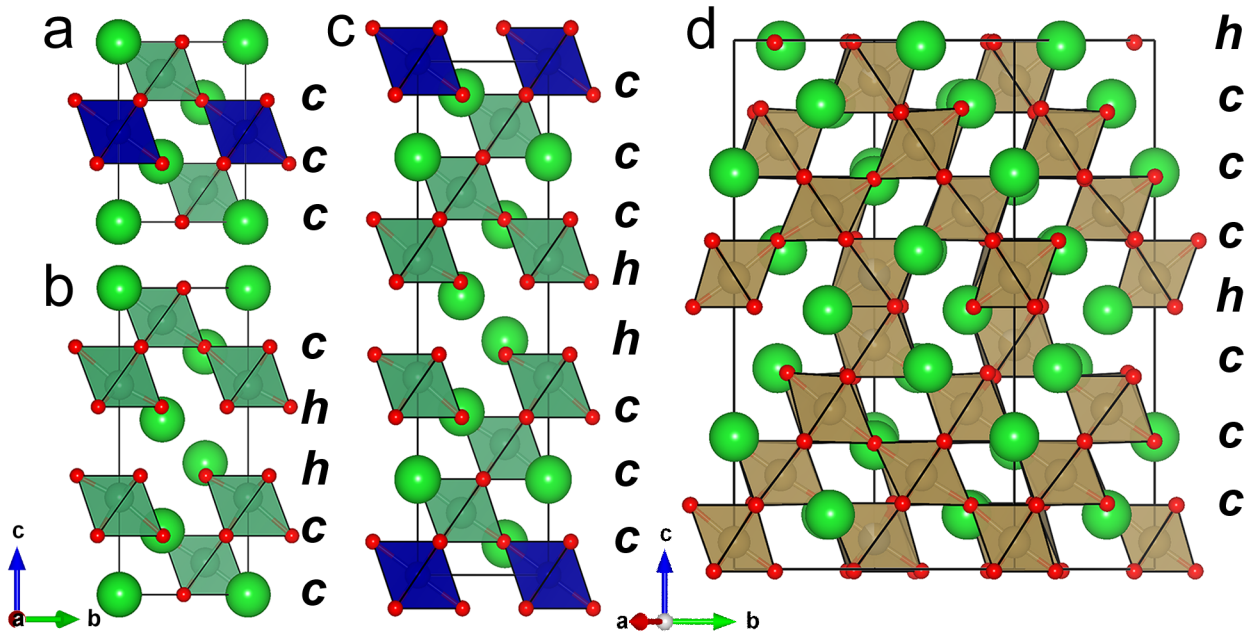

Figure 4.1: (a) The experimental structure of $Ba_3ZnTa_2O_9$, $Ba_3ZnNb_2O_9$ and $Ba_3CoNb_2O_9$. (b) The experimental structure of $Ba_5Nb_4O_{15}$. (c) The experimental structure of $Ba_8CoNb_6O_{24}$ and (d) the experimental twinned structure of $Ba_8ZnTa_6O_{24}$. The green spheres are Ba, red spheres are O, green polyhedra are Nb or Ta, blue polyhedra are Co or Zn and brown polyhedra are Ta/Zn with partial occupancy in some cases.

4.2 Methodology

The development of the Extended Module Materials Assembly (EMMA) method has facilitated the investigation of complex perovskites. In this chapter, the EMMA methodology is applied to close-packed lattices by studying materials in the $Ba_n(Co,Nb)_{n-1}O_{3n}$ hexagonal perovskite family, particularly looking for stable members with longer stacking sequences than those identified to date.

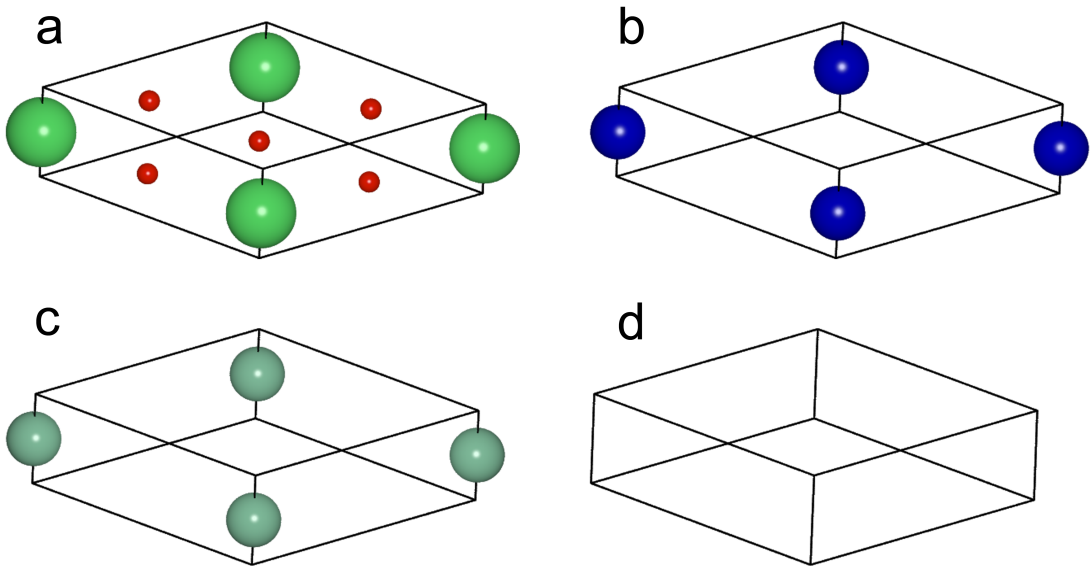

Figure 4.2: The module sets chosen to generate the structures using EMMA: (a) the lattice layer BaO_3 and three interstitial layers; (b) Co (c) Nb and (d) vacancy layer.

The module sets chosen to investigate this compositional series were extracted from $Ba_3CoNb_2O_9$, $Ba_5Nb_4O_{15}$ and $Ba_8CoNb_6O_{24}$ and are shown in Figure 4.2. The close-packed lattice is constructed using BaO_3 modules as described in Chapter 3, as shown in Figure 4.2 (a), while three interstitial layers (α_1, α_2, α_3) were introduced between BaO_3 layers, shown in Figures 4.2 (b)-(d). The empty cell was used to represent the vacancy layer found in both $Ba_5Nb_4O_{15}$ and $Ba_8CoNb_6O_{24}$, since there are no transition metal cations placed between the two BaO_3 layers. All structures were then generated in a $2 \times 2 \times 1$ supercell.

For the initial screening of candidate structures, forcefields were used to perform geometry

relaxations using GULP. A Buckingham potential was used, with the parameters for each ion pairing shown in Table 4.1. In addition, a polarisable shell model was used for both O^{2-} and Ba^{2+}. The values for the potential were taken from a combination of literature sources,[15,16] and tested against the known experimental structures of $Ba_3CoNb_2O_9$, $Ba_5Nb_4O_{15}$ and $Ba_8CoNb_6O_{24}$ in order to reproduce lattice constants within a reasonable limit of 5% and to preserve bonding geometries. For each geometry relaxation, a combination of first order and second order optimisation methods were used: 500 conjugate gradient steps, followed by 500 BFGS steps. Following the initial forcefield screening, the structures were re-evaluated using DFT calculations. The number of structures assessed by DFT is dependent on the system being investigated, and specific details are given for each case where appropriate.

Buckingham Potential			
Interaction	Å(eV)	ρ (eV)	C (eV Å^6)
Nb^{5+} ... O^{2-}	1425.0	0.3650	0.0
Co^{2+} ... O^{2-}	696.3	0.3362	0.0
Ba^{2+} ... O^{2-}	4818.0	0.3067	0.0
O^{2-} ... O^{2-}	22764.3	0.1490	42.0

Shell Charges		
Ion	Y ($\|e\|$)	k (eV Å^{-2})
Ba^{2+}	1.831	34.05
O^{2-}	−2.240	42.00

Table 4.1: The cut-off limit for all interactions was set to 12 Å. The Nb^{5+} ... O^{2-} potential was taken from ref. [16] with the three-body term removed and all other potentials are from ref. [15], with modifications to the O^{2-} ... O^{2-} interaction as found in ref. [17].

For the final ranking, DFT was performed using the criteria as outlined in Chapter 2. A Hubbard U correction was applied to account for the highly correlated d-orbitals present on Co^{2+}. A single effective parameter ($U_{\text{eff}} = U - J$) equal to 3.3 eV was used, as found in related studies.[18] As Co^{2+} can exist as either high-or low-spin, the magnetic moments on the Co ions were calculated. The initial magnetic moments were varied in order to find the magnetisation of the ground state, using values of 5 μB and 2 μB per Co^{2+} ion, for high and low-spin, respectively.

4.3 Known compounds

The known synthesised experimental compounds can be considered as part of the series $Ba_kCo_l\square_mNb_nO_{3k}$, where the empty box indicates a vacancy layer, and k, l, m and n represent integer values. To assess the EMMA methodology as applied to hexagonal perovskites, the compositions $Ba_3CoNb_2O_9$, $Ba_5Nb_4O_{15}$ and $Ba_8CoNb_6O_{24}$ were investigated using the method outlined above.

4.3.1 $Ba_3CoNb_2O_9$

Using the module set shown in Figure 4.2, three structures were generated using EMMA for a 3 layer cell at composition $Ba_3CoNb_2O_9$. However, following forcefield relaxation, only one unique structure emerged, as all three structures were found to converge to the same energy and stacking sequence. Therefore, DFT was performed to determine the magnetic moment on the Co^{2+} ion and to ascertain how accurately DFT is able to reproduce the experimental structure.

The structure generated using EMMA was confirmed to be the experimental structure through inspection of the stacking sequence and confirmation of the space group using FINDSYM. As can be seen from Table 4.2, the experimental unit cell angles are mod-

elled accurately by both forcefields and DFT. There is a significant increase in the unit cell volume following forcefield relaxation, which is not fully rectified upon relaxation with DFT, though some contraction in the *c*-axis is observed. Overall, there is very little difference in the parameters following relaxation with DFT. In general, the PBE functional has been known to overestimate oxide unit cell parameters, so this is not unexpected.[19]

Parameter	Experimental	FF	DFT
a (Å)	11.54	11.70	11.71
b (Å)	11.54	11.70	11.71
c (Å)	7.09	7.23	7.20
α (°)	90.00	90.00	90.00
β (°)	90.00	90.00	90.00
γ (°)	120.00	120.00	120.00
Volume (Å^3)	817.11	857.20	855.17

Table 4.2: Summarising the parameter calculations for FF and DFT calculations

Closer investigation of the structure revealed that the forcefield calculations do not reproduce the interlayer distances found experimentally, resulting in an overestimation of the Nb interlayer distance and an underestimation of the Co interlayer distance, demonstrated in Figure 4.3 (a). In addition, the average bond length in the Co polyhedra is overestimated by 5.6%. Following relaxation of the forcefield structure in DFT, these discrepancies are largely corrected, shown by Figure 4.3 (b). These results are summarised in Table 4.3, with distortion indices calculated using Baur's distortion index in the VESTA visualisation program, which can evaluate the effective coordination number by adding bond distances from all surrounding atoms with a weighting scheme.[20] The functional form is defined such

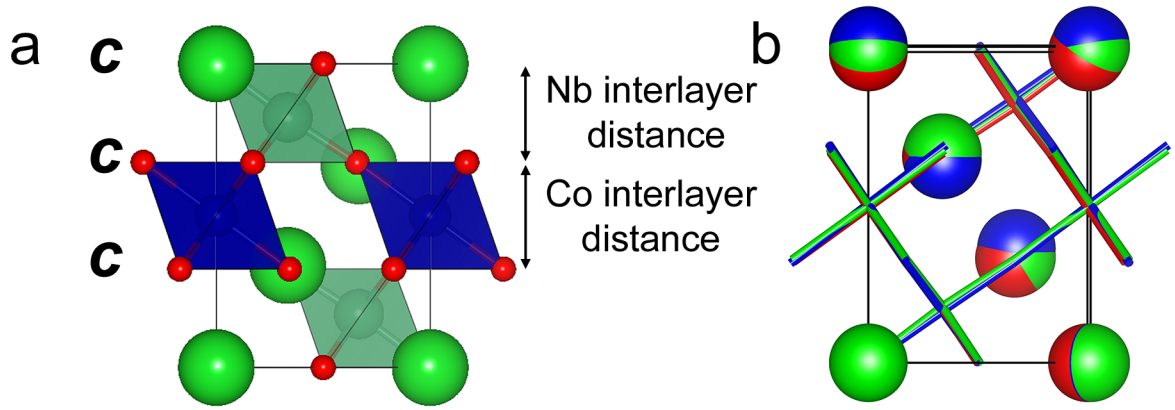

Figure 4.3: (a) The structure of $Ba_3CoNb_2O_9$ as generated by EMMA, following forcefield and DFT relaxation, shown as a $1 \times 1 \times 1$ unit cell. The stacking sequence is shown on the left, while the interlayer distances are defined on the right. (b) The FINDSYM reduced structure of $Ba_3CoNb_2O_9$, for the experimental (red), forcefield (blue) and DFT (green) structures.

that:

$$D = \frac{1}{n} \sum_{i=1}^{n} \frac{|l_i - l_{\text{av}}|}{l_{\text{av}}} \tag{4.1}$$

where D is the distortion index, l_i is the distance from the central atom to the ith coordinating atom, and l_{av} is the average bond length.

Although only one unique structure was obtained following forcefield screening, relaxation using DFT was found to substantially correct the relaxed bonding geometries and allows for investigation of the electronic properties of the compound, for example by obtaining the spin-moment on the Co^{2+} ions. They were found to be high-spin with a total magnetisation of 2.99 μB per ion. Both ferromagnetic and anti-ferromagnetic states were found having the same total energy, suggesting that there is very little magnetic exchange interaction between the metal centres. This is in line with experimental observations of paramagnetism.[21] In addition to the high-spin configuration, which is found experimentally, a low-spin anti-ferromagnetic state, with a spin moment of 0.88 μB per Co^{2+} ion was found. However, this was less stable by 1.29 eV/FU, implying that the high-spin state of the Co^{2+} ions is the ground state.

	Experimental	FF	DFT
Nb interlayer distance (Å)	2.38	2.60 (+9.2%)	2.41 (+1.3%)
Co interlayer distance (Å)	2.32	2.02 (−12.9%)	2.38 (−2.6%)
Mean bond length (Å)	2.01	2.00 (−0.5%)	2.04 (+1.5%)
Distortion index	0.04	0.03 (−17.5%)	0.04 (+8.4%)
Effective coordination number	5.67	5.78 (+2.0%)	5.60 (−1.1%)
Mean bond length (Å)	2.11	2.23 (+5.6%)	2.14 (+1.4%)
Distortion index	0.00	0.00	0.00
Effective coordination number	6.00	6.00	6.00

Table 4.3: Interlayer distances and polyhedra

4.3.2 $Ba_9Co_3Nb_6O_{27}$

Given the modules chosen for the composition of $Ba_3CoNb_2O_9$ in a 3 layer cell, no competing structures were generated. Therefore, the unit cell was tripled in the c direction, resulting in a 9 layer composition of $Ba_9Co_3Nb_6O_{27}$, to determine whether $(Ba_3CoNb_2O_9)_3$ was found as the most stable structure generated by EMMA. In total, EMMA generated 672 structures, which were then relaxed using forcefields. The most stable two structures were found to have energies within 0.09 eV/FU of each other, while the third structure was found to be 1.38 eV/FU less stable than the second structure. Key structural differences include the preference for corner-sharing octahedra as opposed to face-sharing octahedra, with structures comprising the latter found to be less stable than those with the former.

Consequently, only the two most stable structures were relaxed using DFT. Following relaxation with DFT, the stabilities of the two structures switched, with the structure ranked second becoming more stable by 0.63 eV/FU. Both structures are shown in Figure 4.4.

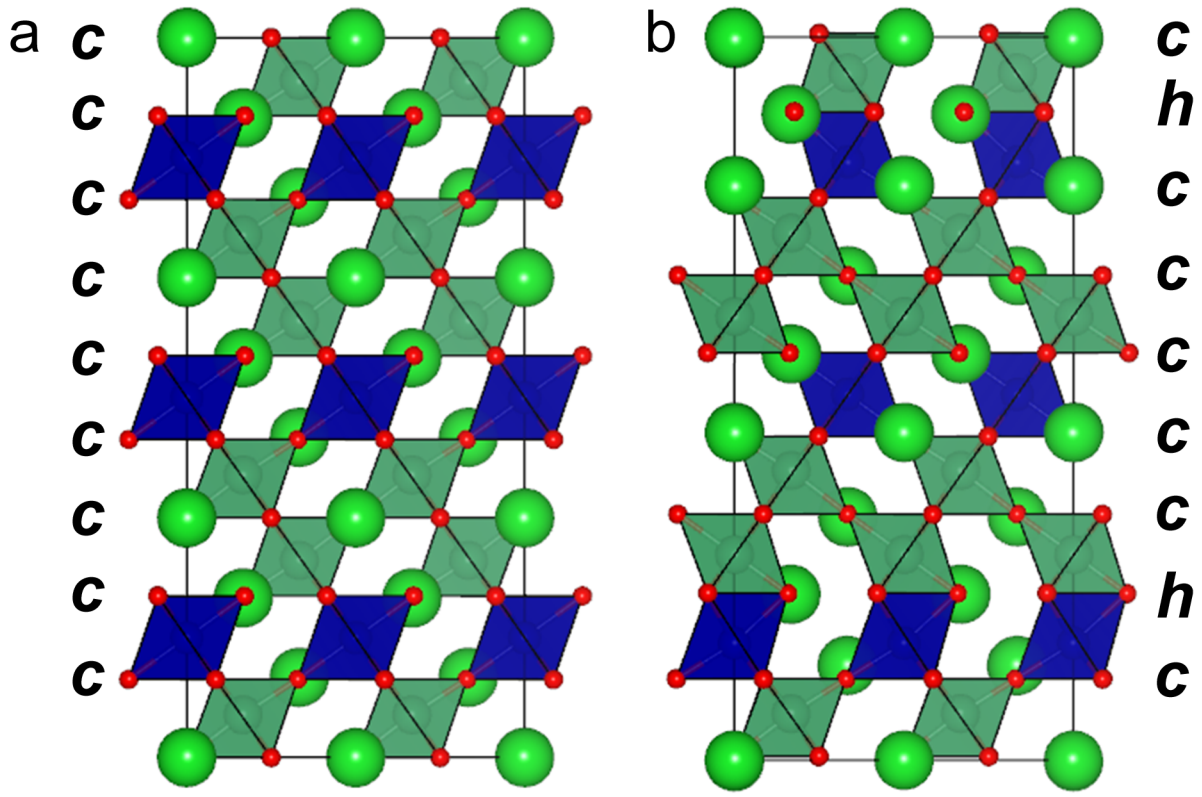

Figure 4.4: The two most stable structures identified by the forcefield screening. Structure (a) is found to be 0.63 eV/FU more stable than structure (b) following DFT relaxation.

The most stable structure, in Figure 4.4 (a), could be reduced to a 3 layer cell in space group $P\bar{3}m1$. The magnetic structure was found to be high-spin ferromagnetic, with all Co^{2+} ions found to be in the same coordination environment. The magnetisation was calculated to be 2.99 μB per Co^{2+} ion, which is the same as the spin-moment calculated for the individual 3 layer structure. No space group other than P1 could be identified for the second structure shown in Figure 4.4, though again the most stable spin state was found to be high-spin. In addition, the most stable structure comprises corner-sharing octahedra, while the less stable structure contains face-sharing octahedra.

Overall, the study of $(Ba_3CoNb_2O_9)_3$ underlines the importance of the DFT step in the EMMA methodology, since it corrects the discrepancies in the stability ranking following the forcefield screening.

4.3.3 $Ba_5Nb_4O_{15}$

$Ba_5Nb_4O_{15}$ was generated in five layers using the same module set as in the study of $Ba_3CoNb_2O_9$; however, due to the compositional constraint, the Co layers were disregarded. Five structures were generated using EMMA, and following forcefield relaxation, only four distinct structures emerged. The two most stable structures had energies within 0.15 eV/FU of each other, while the remaining two structures were over 5.00 eV/FU less stable. Thus, DFT was performed only on the two most stable structures identified in the FF ranking.

Parameter	Experimental	FF	DFT
a (Å)	11.59	11.81	11.78
b (Å)	11.59	11.81	11.78
c (Å)	11.79	12.05	12.00
α (°)	90.00	90.00	90.00
β (°)	90.00	90.00	90.00
γ (°)	120.00	120.00	120.00
Volume ($Å^3$)	1231.79	1454.44	1440.81

Table 4.4: Lattice parameters for $Ba_5Nb_4O_9$

The experimental structure was found to be the most stable structure in both the forcefield screening and DFT relaxation, by 0.15 eV/FU and 0.35 eV/FU respectively. As can be seen from Figure 4.5, the vacancy layer in the forcefield calculations is more contracted than in both the experimental and DFT structures (see Table 4.5). In addition, the distortion index of the Nb polyhedra, above and below the vacancy layer, is corrected by DFT, giving a value of 0.10, matching the experimental value, while the forcefield structure has a distortion index of 0.08.

	Experimental	FF	DFT
Nb interlayer distance (Å)	2.60	2.69 (+3.5%)	2.50 (−3.8%)
Vacancy layer distance (Å)	1.61	0.72 (−55.3%)	1.70 (+5.6%)
Nb polyhedra			
Average bond length (Å)	2.01	2.04 (+1. 5%)	2.04 (+1.5%)
Distortion index	0.04	0.02 (−50.0%)	0.04
Effective coordination number	5.67	5.87 (+3.5%)	5.70 (+0.5%)
Nb polyhedra (distorted)			
Average bond length (Å)	2.05	2.04 (− 0.5%)	2.08 (+1.5%)
Distortion index	0.10	0.08 (+20.0%)	0.10
Effective coordination number	3.74	4.43 (+18.4%)	3.80 (+1.6%)

Table 4.5: Interlayer distances and polyhedra for $Ba_5Nb_4O_9$

In general, the lattice parameters remain largely similar following relaxation of the forcefield structure in DFT (see Table 4.4). The space group was found to be $P\bar{3}m1$ for the DFT relaxed structure, in agreement with the experimental space group. The highest symmetry that could be found for the forcefield structure was $P\bar{3}$, using the same tolerance (0.04 Å) as for the DFT structure. This illustrates that DFT corrects for small displacements in atomic positions, affecting the final symmetry and energy of the structure.

4.3.4 $Ba_8CoNb_6O_{24}$

The next structure in the series is $Ba_8CoNb_6O_{24}$, which is found experimentally to contain a vacancy layer similar to that observed in $Ba_5Nb_4O_{15}$, and thus the same module sets were used as in the previous studies to generate structures for this composition in an eight

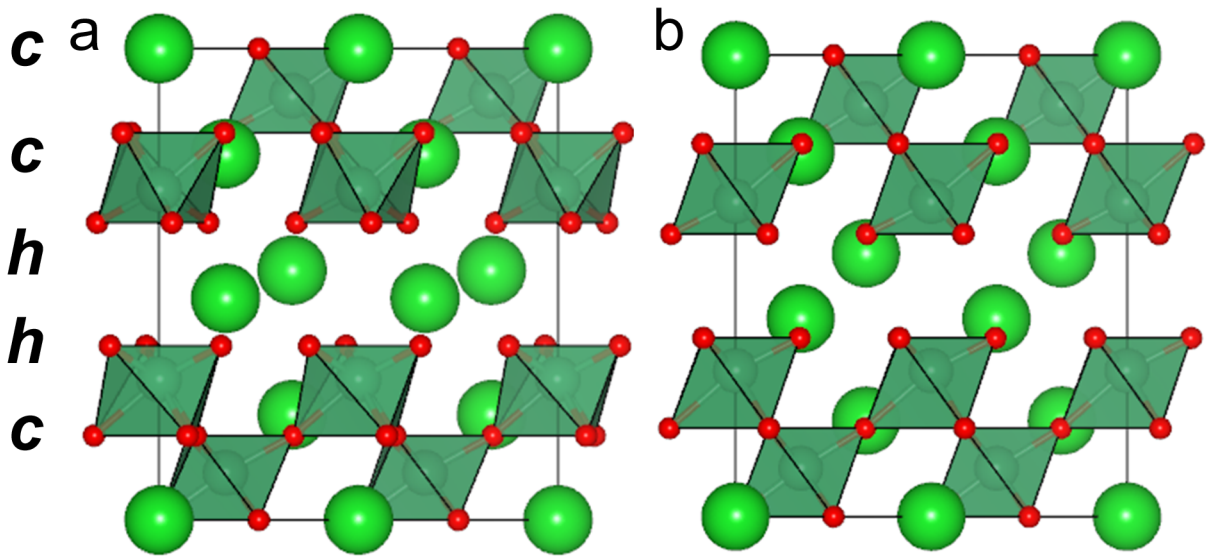

Figure 4.5: The lowest energy structure in both forcefield and DFT calculations for $Ba_5Nb_4O_{15}$, shown in (a) and (b) respectively, illustrating the contraction of the vacancy layer and the deformation of the polyhedra after forcefield relaxation.

layer cell. EMMA generated 448 structures, of which 21 did not converge during geometry optimization, either due to unphysical cell parameters or by reaching the maximum number of steps.

Examples of structures that did not converge are shown in Figure 4.6. The starting structures before relaxation are shown in the top left corner. Structure (a) did not converge in the maximum number of cycles, and and the forcefield had trouble maintaining the face-sharing coordination polyhedra chain. For structure (b), the conditions for a minimum were not satisfied, with a higher gradient than the other converged structures. Structure (c) did not converge, with a significant expansion in the unit cell, giving unphysical cell dimensions.

The energies of the composition $Ba_8CoNb_6O_{24}$ following forcefield relaxation were more evenly distributed, as shown in Figure 4.7 (a) and consequently, the ten most stable unique structures were selected for DFT calculations, based on a compromise between computational expense and exhaustively searching for the experimental structure. The results of the DFT calculations are summarised in Figure 4.8, as ranked by DFT.

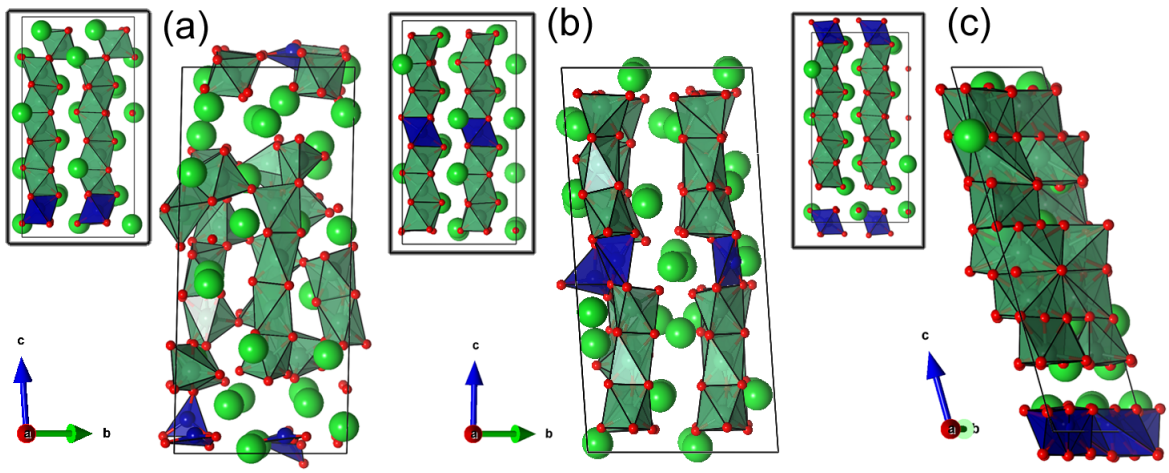

Figure 4.6: Examples of structures that did not converge following forcefield screening of $Ba_8CoNb_6O_{24}$. Structure (a) reached the maximum number of steps, structure (b) did not satisfy the conditions for convergence and structure (c) was found to have unphysical cell dimensions. The starting point for each structure is shown in the top left hand box.

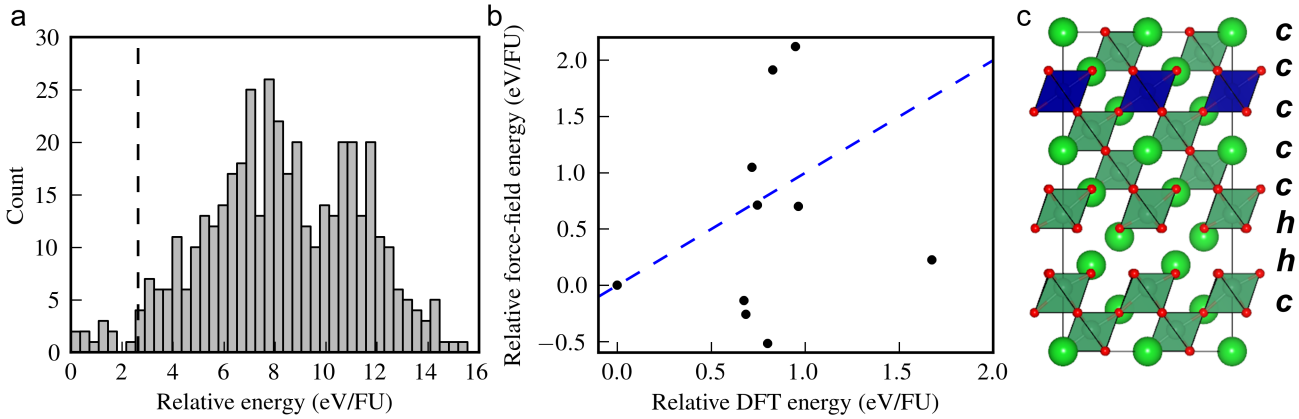

Figure 4.7: (a) Histogram showing the energy distribution of possible $Ba_8CoNb_6O_{24}$ structures obtained following forcefield screening. (b) Scatter plot showing the difference between the relative stabilities in both forcefield and DFT calculations, relative to the most stable structure in DFT. The points would lie on the blue line if the forcefield and DFT results were in exact agreement. (c) The lowest energy structure from DFT.

The DFT stability ranking of the structures was found to be significantly different from the FF ranking, illustrated by Figure 4.7 (b). The structure ranked fourth in the forcefield screening became the most stable structure upon relaxation with DFT, shown in Figure 4.7 (c). This structure was then confirmed to be the experimental structure, following determination of space group of $P\bar{3}m1$ and inspection of the stacking sequence, which was found to have the same motif as the experimental structure. It was found to be 0.67 eV/FU more

stable than the structure ranked second by DFT. Similar to $Ba_3CoNb_2O_9$, the magnetisation per Co^{2+} ion was found to be 2.99 μB. In comparison, the low-spin ferromagnetic structure, with a magnetisation of 1.01 μB, was found to be 0.94 eV/FU less stable than the high-spin structure.

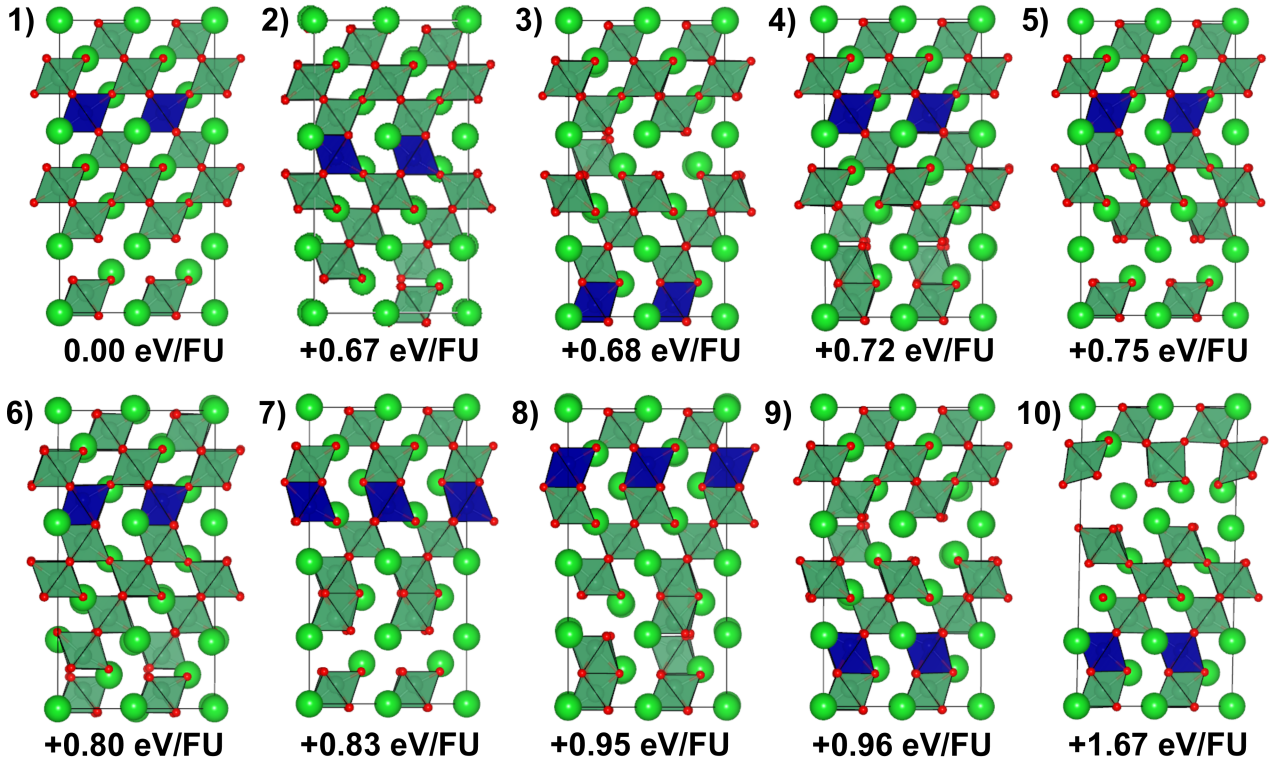

Figure 4.8: The most stable ten structures from the forcefield screening as ranked by DFT.

In terms of composition, $Ba_8CoNb_6O_{24}$ can be considered as a combination of $Ba_3CoNb_2O_9$ and $Ba_5Nb_4O_{15}$. However, since $Ba_8CoNb_6O_{24}$ can be isolated experimentally, the energy of $Ba_8CoNb_6O_{24}$ is expected to be lower than the combined energies of $Ba_3CoNb_2O_9$ and $Ba_5Nb_4O_{15}$. The energy difference between $Ba_8CoNb_6O_{24}$ and the summed energies of $Ba_3CoNb_2O_9$ and $Ba_5Nb_4O_{15}$ can be defined as:

$$\Delta E = E_8 - \left(E_3 + E_5\right) \tag{4.2}$$

Or more generally, for compositions corresponding to $m(Ba_3CoNb_2O_9)$ and $n(Ba_5Nb_4O_{15})$:

$$\Delta E_{m,n} = E_{3m+5n} - \left(mE_3 + nE_5\right) \tag{4.3}$$

Interestingly, the energies are very similar, with $\Delta E_{1,1}$ equal to 3 meV/FU, which offers some explanation as to why the $Ba_8CoNb_6O_{24}$ compound is difficult to synthesise. On closer inspection, the $Ba_8CoNb_6O_{24}$ structure appears very similar to a $Ba_3CoNb_2O_9$ subunit stacked on top of a $Ba_5Nb_4O_{15}$ subunit. It is therefore possible to envision greater length stacking sequences, based on a combination of the $Ba_3CoNb_2O_9$ and $Ba_5Nb_4O_{15}$ subunits.

4.4 Novel Compositions

4.4.1 Compositional rules

Compounds of the formula $Ba_kCo_l\square_mNb_nO_{3k}$ can be considered part of the compositional series $Ba_kCo_{l-m}Nb_{k-l-m}O_{3k}$, eliminating n. This is in agreement with the known compounds of $Ba_3CoNb_2O_9$ ($k = 3$, $l = 1$, $m = 0$), $Ba_5Nb_4O_{15}$ ($k = 5$, $l = 0$, $m = 1$) and $Ba_8CoNb_6O_{24}$ ($k = 8$, $l = 1$, $m = 1$). Hence, varying the values of l and m can give novel compositions.

If one of l or m is zero (i.e. only cobalt or vacancy layers are present), the structure is constrained to multiples of the two known structures, so no new structures would be expected from EMMA. For example, $m = 0$, $k = 3l$, $n = 2l$, gives $Ba_{3l}Co_lNb_{2l}O_{9l}$ or $l(Ba_3CoNb_2O_9)$ and $l = 0$, $k = 5m$, $n = 4m$ gives $Ba_{5m}Nb_{4m}O_{15m}$ or $m(Ba_5Nb_4O_{15})$. This was demonstrated in Section 3.1.2 for the composition $Ba_9Co_3Nb_6O_{27}$, or alternatively, $3\,Ba_3CoNb_2O_9$. The next structures in the series occur when $l = 2$, $m = 1$, $k = 11$, giving $Ba_{11}Co_2Nb_8O_{33}$, and when $l = 1$, $m = 2$, $k = 13$, giving $Ba_{13}CoNb_{10}O_{39}$. These structures

have been studied using the same methodology outlined above for the known experimental compositions.

4.4.2 $Ba_{11}Co_2Nb_8O_{33}$

$Ba_{11}Co_2Nb_8O_{33}$ differs from the other members in the compositional series as it contains two cobalt layers per unit cell rather than one. Increasing the stacking length to 11 layers had a great impact on the number of EMMA-generated structures, which increased in comparison to the 8 and 9 layer members, to 10,395, with an approximate 50% failure rate for FF structure relaxation. Similar to $Ba_8CoNb_6O_{24}$, the energy distribution was evenly spread, and the lowest ten energy structures were selected for further optimisation, as shown in Figure 4.9 (a).Since Co^{2+} was found to be high spin in both $Ba_3CoNb_2O_9$ and $Ba_8CoNb_6O_{24}$, it was assumed that this would also hold for $Ba_{11}Co_2Nb_8O_{33}$, and the calculations were set up with an initial magnetic moment of 5 μB.

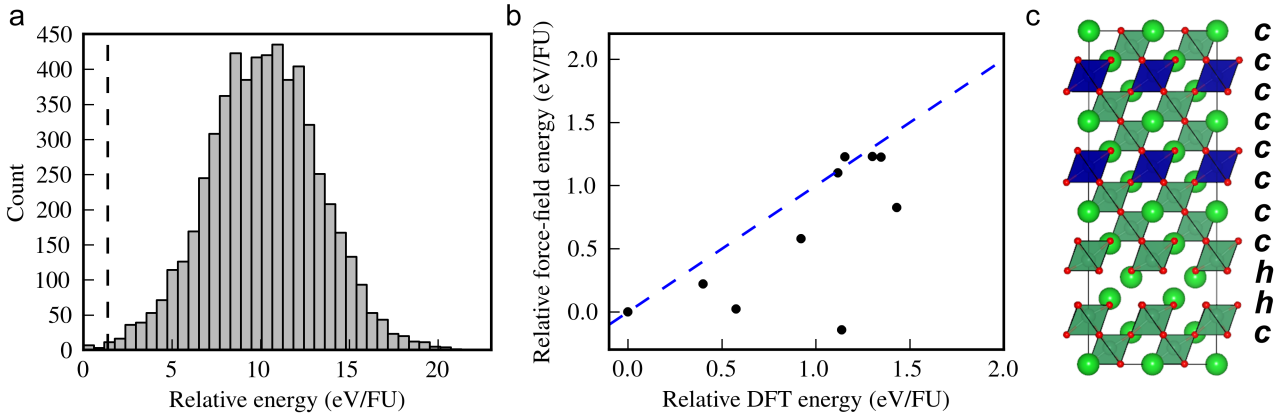

Figure 4.9: (a) Histogram showing the energy distribution of $Ba_{11}Co_2Nb_8O_{33}$ obtained following forcefield screening. (b) Scatter plot showing the difference between the relative stabilities in both forcefield and DFT calculations, relative to the most stable structure in DFT. The points would lie on the blue line if the forcefield and DFT results were in exact agreement. (c) The lowest energy structure from DFT.

In general, the forcefield ranking was in-line with the DFT ranking, as shown in Figure 4.9 (b), though there were some cases where the DFT ranking of relative stabilities differed from that of the forcefield stage. The most stable structure, shown in Figure 4.9 (c), has a stacking

sequence of $(ccc)_2chhc$. It was identified as high-spin, with a spin-moment of 2.74 ± 0.03 μB on the Co^{2+} ions, as given by the spin-density projected onto the PAW projectors. This is in agreement with the other high-spin structures investigated in this compositional series. The structure was also found to be ferrimagnetic, with an overall magnetisation of 0.22 μB. The ten lowest energy structures are shown in Figure 4.10

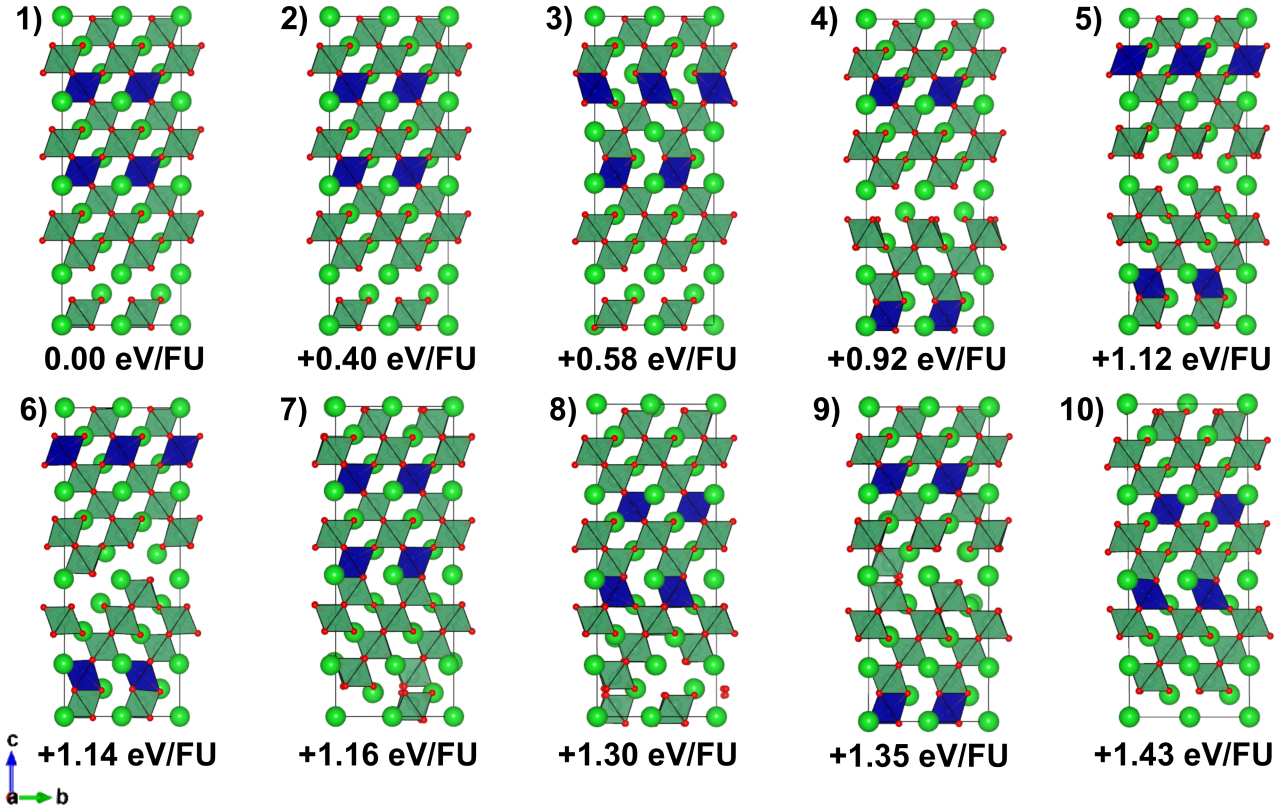

Figure 4.10: The most stable ten structures from the forcefield screening as ranked by DFT.

The most stable structure is 0.40 eV/FU more stable than the second most stable structure in the DFT ranking. Closer inspection shows that they are isostructural, relaxing to the same structure in the forcefield screening with an energy difference of 0.22 eV/FU. This illustrates the importance of the oxygen positions in determining the relative energies, as there are small differences in the oxygen atomic coordinates.

The second ranked structure was found to have a different magnetic moment when relaxed using DFT, accounting for the difference in energy in the final ranking step. It was found to

be low-spin, with a magnetic moment of 1.25 μB. The fact that this low-spin analogue was found to be 0.40 eV/FU less stable again shows the preference of Co^{2+} to exist as high-spin in these structures.

The stacking sequence of the most stable $Ba_{11}Co_2Nb_8O_{33}$ compound matches the structural motif of two $Ba_3CoNb_2O_9$ structures stacked on the $Ba_5Nb_4O_{15}$ structure. Using equation 4.2, it is found that the best $Ba_{11}Co_2Nb_8O_{33}$ structure is less stable than the combination of individual subunits by 20 meV/FU.

4.4.3 $Ba_{13}CoNb_{10}O_{39}$

Similarly to the known material $Ba_8CoNb_6O_{24}$ in section 4.3.4, $Ba_{13}CoNb_{10}O_{39}$ has a single cobalt layer, but with a much greater stacking length. It differs from the other members of the compositional series considered so far in having two fewer B site cations than A site cations rather than one fewer. This composition was chosen to investigate whether the different cation ratios affects the overall ordering.

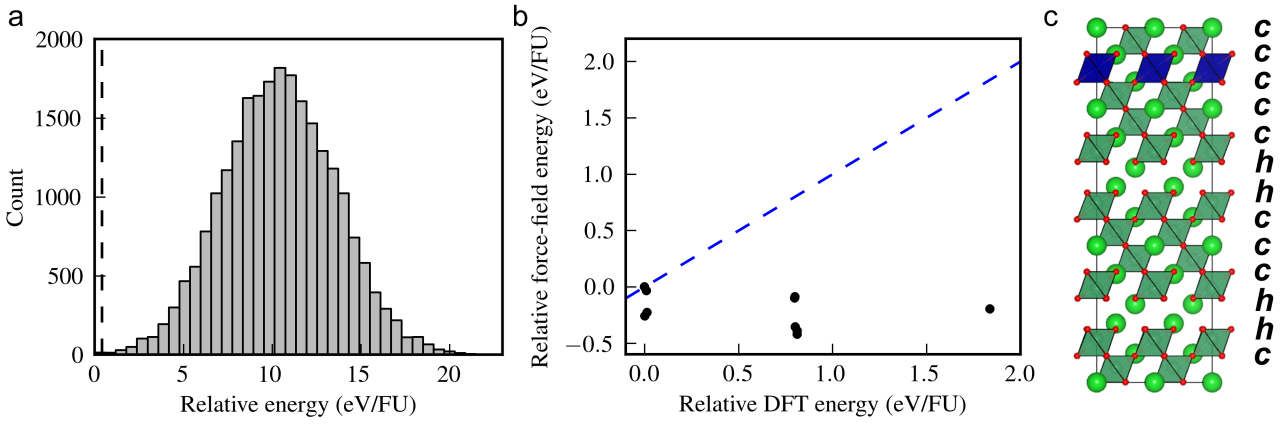

Figure 4.11: (a) Histogram showing the energy distribution of $Ba_{13}CoNb_{10}O_{39}$ obtained following forcefield screening. (b) Scatter plot showing the difference between the relative stabilities in both forcefield and DFT calculations, relative to the most stable structure in DFT. The points would lie on the blue line if the forcefield and DFT results were in exact agreement. (c) The lowest energy structure from DFT.

The number of structures generated by EMMA was 54,054, and again the ten most sta-

ble structures were taken forward for optimisation with DFT. The failure rate was similar to that found in the $Ba_{11}Co_2Nb_8O_{33}$ system, with the energy distribution of the converged structures is shown in Figure 4.11 (a). Of the ten structures, the most stable four were found to have energies within 20 meV of each other, as shown in Figure 4.11 (b), and inspection confirmed that the stacking sequence was the same in each case. This shows that the more structures generated by EMMA, the greater the possibility of relaxing into similar structures from initially distinct starting geometries. These structures will have slightly different forcefield energies due to different final ionic positions, are not distinguished as identical in the post-FF screening process, and thus are taken forward to the DFT calculations. The structures following DFT relaxation then have very similar energies and geometries.

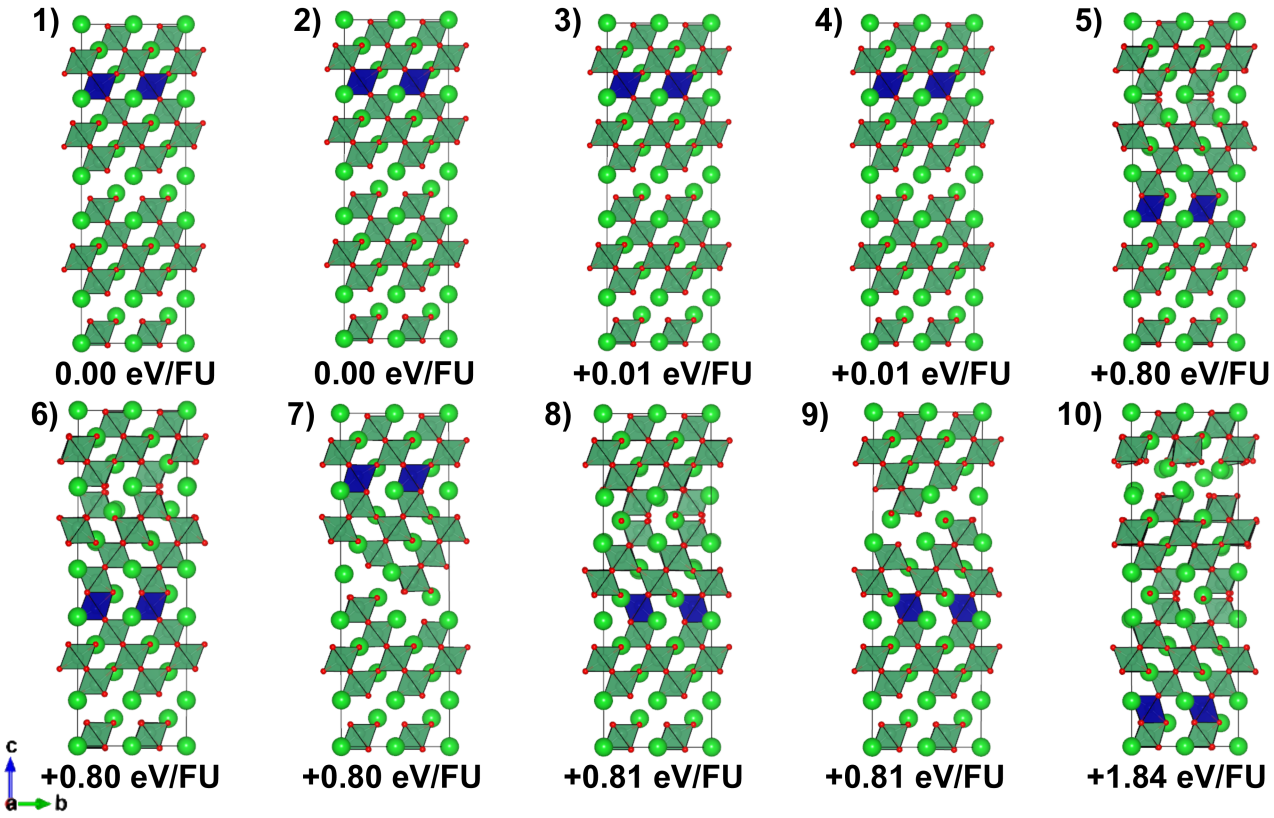

Figure 4.12: The most stable ten structures from the forcefield screening as ranked by DFT.

The lowest ten structures are shown in Figure 4.12. The stacking sequence of the most stable $Ba_{13}CoNb_{10}O_{39}$ structure is found to be $ccc(chhcc)_2$, which is the same stacking sequence

that is obtained by placing the $Ba_3CoNb_2O_9$ structure on top of two $Ba_5Nb_4O_{15}$ structures, as shown in Figure 4.11 (c). The energetics confirms this, as the energy is very similar to that obtained when summing the respective energies, having the same value within 3 meV/FU. This is similar to that found in the $Ba_8CoNb_6O_{24}$ case, which can be synthesised experimentally. However, in this case, the structure of $Ba_{13}CoNb_{10}O_{39}$ is found to be less stable than the constituent subunits, whereas $Ba_8CoNb_6O_{24}$ is found to be more stable.

As with the other most stable structures, the magnetisation was found to be high-spin, with a magnetisation of 2.99 μB per Co^{2+} ion. A metastable state, with three Co^{2+} ions having a magnetic moment of 2.74 μB and one with a magnetic moment of 1.03 μB, was found to be less stable by 0.31 eV/FU.

4.5 Conclusions

Investigation of the compositional series $Ba_kCo_l\square_mNb_nO_{3k}$ demonstrates an extension of the EMMA method to hexagonal perovskites. The experimental structures of $Ba_3CoNb_2O_9$, $Ba_5Nb_4O_{15}$ and $Ba_8CoNb_6O_{24}$ were identified as the lowest energy structure for each composition. Additionally, the method was successful with periodically repeated structures, as seen in the case of $(Ba_3CoNb_2O_9)_3$, which was initially built as a general 9 layer structure.

The implementation of EMMA for structures based on close-packed lattices makes accessible an extremely wide field of potential material families that EMMA can be routinely applied to. However, it is important to note the significance of the forcefield screening in this process, as the energy distribution determines the structures taken forward to the DFT ranking. Thus, it is imperative that the screening is able to identify viable candidate structures.

The investigation of the novel compositions with $k = 11$ and 13 show that the EMMA method can be used to find new structures and predict intergrowths. It was found that these compositions consist of subunits of $Ba_3CoNb_2O_9$ and $Ba_5Nb_4O_{15}$, as found in the case of

$Ba_8CoNb_6O_{24}$. The energy differences between $Ba_{11}Co_2Nb_8O_{33}$ and $Ba_{13}CoNb_{10}O_{39}$ and the respective $Ba_3CoNb_2O_9$ and $Ba_5Nb_4O_{15}$ subunits suggest that although solid state synthesis may be difficult due to thermodynamic reasons, synthesis of these compositions might be possible using layer-by-layer growth, for example, by using pulsed layer deposition (PLD) or molecular beam epitaxy (MBE), which are limited by kinetics and allow formation of thermodynamically metastable states.[22]

In addition, studies of the magnetic structures of these compounds show that there is little difference in the relative stabilities between ferromagnetic and anti-ferromagnetic ordering, suggesting that the exchange energy for Co^{2+} is small for the specific Hubbard U value chosen in this study. All systems investigated were found to be most stable with Co^{2+} in the high spin state, again for this specific U. Future work could investigate the dependence of such magnetic states on the Hubbard U value.

The present work has extended the EMMA modular description of perovskite compounds to hexagonal unit cells. Due to the success in predicting hexagonal perovskites with two transition metal centres, the method can now be extended to structural families with three or more centres, or similar compounds with unsolved structures, such as $Ba_3Nb_2O_8$, which is investigated in the following chapter.

References

1. Bradley, K. A. *et al.* Reported and predicted structures of $Ba(Co,Nb)_{1-\delta}O_3$ hexagonal perovskite phases. *Physical Chemistry Chemical Physics* **16,** 21073–21081 (39 2014).

2. Vanderah, T. A. Talking ceramics. *Science* **298,** 1182–1184 (2002).

3. King, G. & Woodward, P. M. Cation ordering in perovskites. *Journal of Materials Chemistry* **20,** 5785–5796 (2010).

4. Davies, P. K., Wu, H., Borisevich, A. Y., Molodetsky, I. E. & Farber, L. Crystal Chemistry of Complex Perovskites: New Cation-Ordered Dielectric Oxides. *Annual Review of Materials Research* **38,** 369–401 (2008).

5. Darriet, J. & Subramanian, M. A. Structural relationships between compounds based on the stacking of mixed layers related to hexagonal perovskite-type structures. *Journal of Materials Chemistry* **5,** 543–552 (1995).

6. Trolliard, G., Ténèze, N., Boullay, P. & Mercurio, D. TEM study of cation-deficient-perovskite related $A_nB_{1-n}O_{3n}$ compounds: the twin-shift option. *Journal of Solid State Chemistry* **177,** 1188–1196 (2004).

7. Lichtenberg, F., Herrnberger, A. & Wiedenmann, K. Synthesis, structural, magnetic and transport properties of layered perovskite-related titanates, niobates and tantalates of the type. *Progress in Solid State Chemistry* **36,** 253–387 (2008).

8. Desu, S. B. & O'Bryan, H. M. Microwave loss quality of $BaZn_{1/3}Ta_{2/3}O_3$ ceramics. *Journal of the American Ceramic Society* **68,** 546–551 (1985).

9. Lufaso, M. W. Crystal Structures, Modeling, and Dielectric Property Relationships of 2:1 Ordered $Ba_3MM'_2O_9$(M = Mg, Ni, Zn; M' = Nb, Ta) Perovskites. *Chemistry of Materials* **16,** 2148–2156 (2004).

10. Hughes, H., Iddles, D. M. & Reaney, I. M. Niobate-based microwave dielectrics suitable for third generation mobile phone base stations. *Applied Physics Letters* **79,** 2952–2954 (2001).

11. Moussa, S. M. *et al.* $Ba_8ZnTa_6O_{24}$: a high-Q microwave dielectric from a potentially diverse homologous series. *Applied Physics Letters* **82,** 4537–4539 (2003).

12. Anderson, M. T., Greenwood, K. B. & Taylor, G. A. B-cation arrangements in double perovskites. *Progress in Solid State Chemistry* **22,** 197–233 (1993).

13. Mallinson, P. M. *et al.* $Ba_8CoNb_6O_{24}$: A d^0 Dielectric Oxide Host Containing Ordered d7 Cation Layers 1.88 nm Apart. *Angewandte Chemie International Edition* **44,** 7733–7736 (2005).

14. De Paoli, J. M., Alonso, J. A. & Carbonio, R. E. Synthesis and structure refinement of layered perovskites $Ba_{5-x}La_xNb_{4-x}Ti_xO_{15}$ ($x = 0$, 1, 2, 3 and 4) solid solutions. *Journal of Physics and Chemistry of Solids* **67,** 1558–1566 (2006).

15. Woodley, S. M., Battle, P. D., Gale, J. D. & Catlow, R. A. The prediction of inorganic crystal structures using a genetic algorithm and energy minimisation. *Physical Chemistry Chemical Physics* **1,** 2535–2542 (1999).

16. Jackson, R. A. & Valerio, M. E. G. A new interatomic potential for the ferroelectric and paraelectric phases of $LiNbO_3$. *Journal of Physics: Condensed Matter* **17,** 837–843 (2005).

17. Dyer, M. S. *et al.* Computationally Assisted Identification of Functional Inorganic Materials. *Science* **340,** 847–852 (2013).

18. Lee, Y.-L., Kleis, J., Rossmeisl, J. & Morgan, D. *Ab initio* energetics of $LaBO_3$ (001)(B=Mn, Fe, Co, and Ni) for solid oxide fuel cell cathodes. *Physical Review B* **80,** 224101 (2009).

19. Loschen, C., Carrasco, J., Neyman, K. M. & Illas, F. First-principles LDA+U and GGA+U study of cerium oxides: dependence on the effective U parameter. *Physical Review B* **75,** 035115 (2007).

20. Momma, K. & Izumi, F. VESTA: a three-dimensional visualization system for electronic and structural analysis. *Journal of Applied Crystallography* **41,** 653–658 (2008).

21. Ting, V. *et al.* A structure, conductivity and dielectric properties investigation of $A_3CoNb_2O_9$ (A=Ca^{2+}, Sr^{2+}, Ba^{2+}) triple perovskites. *Journal of Solid State Chemistry* **177,** 4428–4442 (2004).

22. Palgrave, R. G. *et al.* Artificial construction of the layered Ruddlesden–Popper manganite $La_2Sr_2Mn_3O_{10}$ by reflection high energy electron diffraction monitored pulsed laser deposition. *Journal of the American Chemical Society* **134,** 7700–7714 (2012).

Chapter 5

Application of EMMA to the unknown structure of $Ba_3Nb_2O_8$

Abstract

The structure of $Ba_3Nb_2O_8$ is unsolved, and several structures have been proposed with a variety of niobium coordination environments and occupancies. The EMMA process has been successfully applied to the compositional series $Ba(Co,Nb)_{1-\delta}O_3$, and hence has the potential to help solve the structure of $Ba_3Nb_2O_8$. In this chapter, the forcefield choice is refined based on the consistency of the ranking between the forcefield and DFT calculations, and repeated structures are identified before the DFT step based on atomic coordinates to reduce the number of calculations. The proposed candidate structures are then assessed based on energetics.

5.1 Introduction

The structure of $Ba_3Nb_2O_8$ is found to be experimentally metastable with respect to $Ba_5Nb_4O_{15}$ in chemical equilibrium.[1] The well-defined structure of $Ba_5Nb_4O_{15}$ was discussed at length in the previous chapter, being one of the fundamental units in the compositional series $Ba(Co,Nb)_{1-\delta}O_3$. However, the structure of $Ba_3Nb_2O_8$ is poorly understood in comparison to the other members of the series, in particular with respect to niobium coordination and occupancy.

Various structures have been proposed for $Ba_3Nb_2O_8$, though none have been found to be stable within a single unit cell of the bulk crystal. Two structures are shown below in Figure 5.1, taken from the Inorganic Chemical Structure Database (ICSD).[1,2] These structures are representations of two main proposed structures: the Vanderah structure and the Kemmler-Sack structure.[1]

Both structures are closely related, with structure (a) giving the possibility of a second niobium site, forming face-sharing octahedra with the tetrahedra surrounding two adjacent Nb1 sites. The occupation of the Nb2 sites as opposed to the Nb1 sites leads to an uncoordinated oxygen ion, with a suggested occupancy of the three Nb2 sites of 15%. This leads to a 92.5% occupancy of the Nb1 sites. Both structures are found to be in the $R\bar{3}mH$ space group.

The structure found by Vanderah et al. is a fully ordered structure, with only a single niobium site in a tetrahedral coordination environment, which may suggest that the occupancy of the second niobium site is a feature occurring at grain boundaries only. The structure proposed by Kemmler-Sack allows for the possibility of a second niobium site occupying an octahedral coordination environment, face sharing with two tetrahedra surrounding Nb1 sites and thus a Nb1 vacancy is created to compensate.

DFT calculations were carried out by Dr David Quigley at the University of Warwick* who

*Private correspondence via email

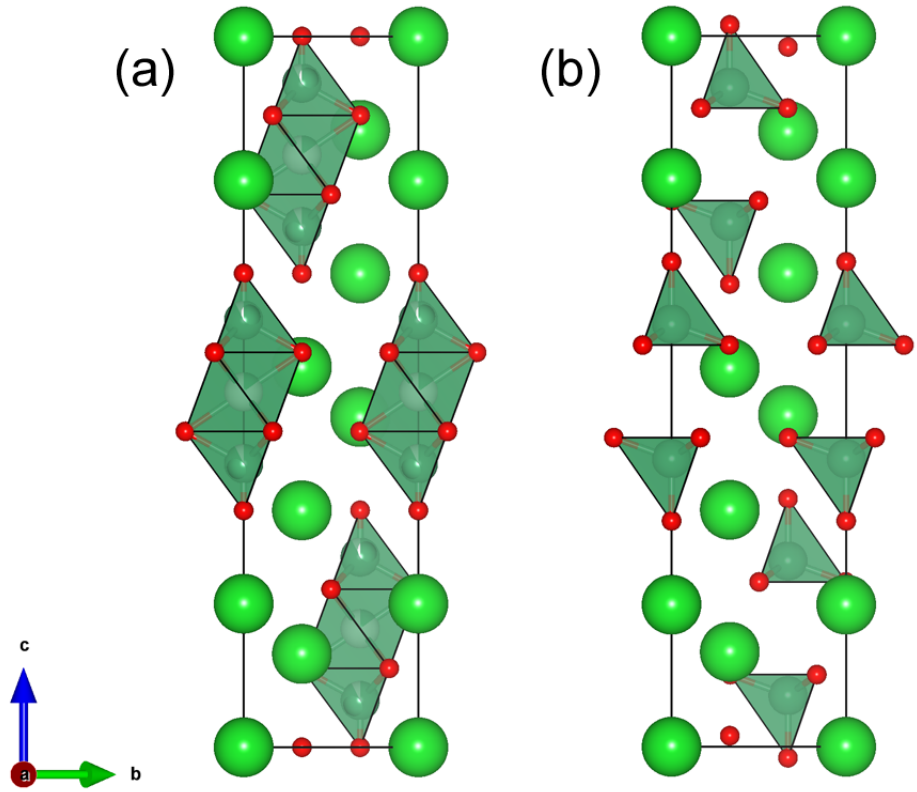

Figure 5.1: Possible structures of $Ba_3Nb_2O_8$; (a) ICSD 15507 (b) ICSD 95193

investigated the occupancy of Nb sites by constructing a number of cells to explore the various coordination environments that the partial occupancy of Nb1 and Nb2 creates. The configurations are summarised as follows:

1. 100% occupancy of Nb1 sites, with zero occupancy of Nb2 sites. The structure relaxes to structure (B) as shown in Figure 5.2.

2. Occupancy of one Nb2 site within a single unit cell, leaving all Nb1 sites occupied. This configuration is not charge balanced if the ions are in their expected oxidation states.

3. Occupancy of one Nb2 site with an adjacent Nb1 site vacant in a single unit cell, corresponding to 1/3 occupancy of the the Nb2 site

4. Occupancy of one Nb2 site with an adjacent Nb1 site vacant in a $2 \times 2 \times 1$ supercell,

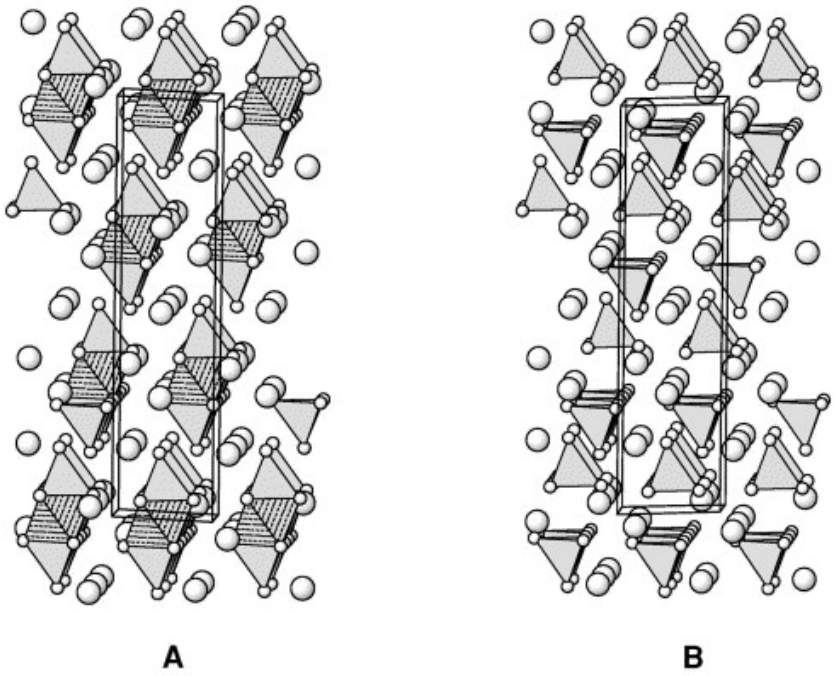

Figure 5.2: Possible structures of $Ba_3Nb_2O_8$; (A) The Kemmler-Sack configuration, and (B) The Vanderah configuration. Large spheres represent Ba ions, smaller spheres are O, and Nb ions occupy the polyhedra. The models are in agreement except that in A, partial occupancy (15%) of the NbO_6 octahedral sites is proposed, as indicated by the hatched octahedra.[1]

giving an occupancy of approximately 15%

5. Similar to configuration 4, but the Nb1 vacancy is placed as far as possible away from the Nb2 site as is possible within the supercell.

Both configurations 3 and 4 relaxed to the fully occupied Nb1 structure, as described in configuration 1. Configuration 5 was found to be 18 eV higher per conventional unit cell than in the case of 100% occupancy of Nb1 sites, excluding situations such as surface or grain boundaries where beneficial environments for Nb1 vacancies could exist. Therefore, the Vanderah structure remains the most promising structural configuration for $Ba_3Nb_2O_9$.

While energetically favourable, the Vanderah structure is inconsistent with experimental quadrupolar coupling parameters and raises questions as to whether this structure is experimentally realised. There is the potential for additional crystal structures that have not yet been identified, including structures that may exhibit symmetrically inequivalent niobium

sites.

Due to the success of the EMMA method in predicting the structure of $Ba_5Nb_4O_{15}$ and associated structures, identifying additional structures for $Ba_3Nb_2O_8$ becomes increasingly feasible.

5.2 EMMA build

The EMMA building process was the same as described previously in Chapters 3 and 4, though due to the possibility of tetrahedrally coordination Nb (as opposed to only the octahedrally coordinated Nb found in the $Ba_kCo_l\square_mNb_nO_{3k}$ series), a number of different layers were used. These are summarised below in Figure 5.3.

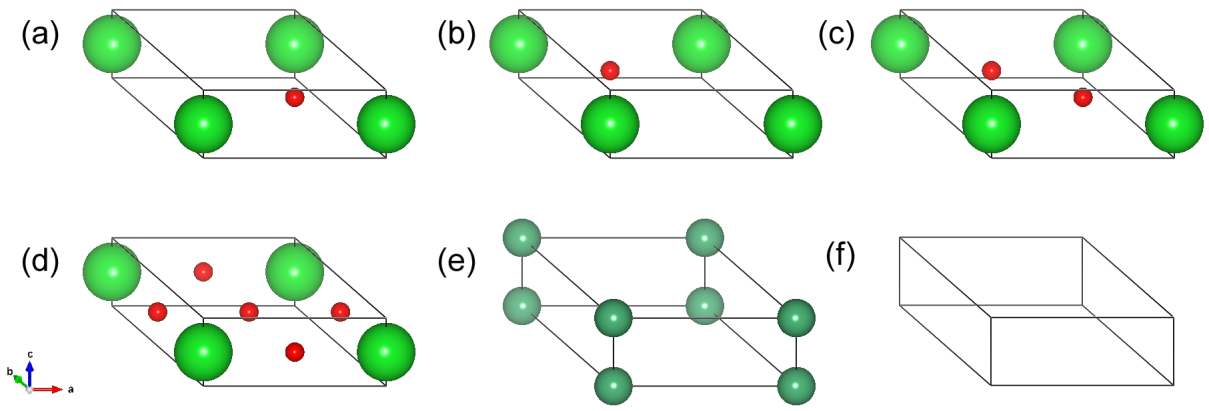

Figure 5.3: The layers used in the study of $Ba_3Nb_2O_8$: (a) BaO (1) (b) BaO (2) (c) BaO_2 (d) BaO_3 (e) Nb (f) Vacancy

The candidate structures were assembled as a nine-layer structure in a $2 \times 2 \times 1$ unit cell to accommodate the vacancy systems described above, and as such, the total number of structures generated totalled 153,216. Due to the high number of structures, performing DFT on all structures was not an option and as a result forcefield screening was used to highlight interesting structures.

5.3 Forcefield Optimisation

In the methodology outlined in Chapter 3, a key component of the process is the ability to identify potential candidate structures in the initial forcefield screening. It is therefore essential that the forcefield ranks promising structures high enough to survive the initial cut, usually set by examining the distribution of structures in comparison to the lowest energy structure. In the previous chapter, cuts were made based on the top ranked ten structures, in this instance constrained by computing resources available for DFT calculations.

5.3.1 Determining a Suitability Parameter

The suitability of a particular forcefield can be assessed through comparison to known experimental structures, using lattice parameters such as unit cell dimensions as a guide. This was seen in the previous chapter, where the forcefield parameters were chosen based on comparison to the known experimental structures of $Ba_3CoNb_2O_9$, $Ba_5Nb_4O_{15}$ and $Ba_8CoNb_6O_{24}$. In addition, other practical considerations can be taken into account, such as additions of shell charges and higher order bond descriptions, such as three-body terms, which may bias particular coordination environments. However, since $Ba_3Nb_2O_8$ has an unconfirmed structure, more care has to be taken to ensure that potential structures are not missed in the initial screening stage.

Therefore, the forcefield used in Chapter 4 was examined more closely, looking at the similarity between the ranking of the forcefield calculations and DFT calculations for the structures of $Ba_5Nb_4O_{15}$ and $Ba_8CoNb_6O_{24}$. The results in Table 5.1 demonstrate that although the forcefield ranking is the same as the DFT ranking for $Ba_5Nb_4O_{15}$, the energy spacing relative to the previous structure is not accurately matched, underestimating some differences and overestimating others. This is most clearly seen in the difference between structures 4 and 5, with DFT calculations giving an energy difference of 1.717 eV/FU, while forcefield

calculations give an energy difference of 5.440 eV/FU.

Structure Number	Δ_{FF} (eV/FU)	Δ_{DFT} (eV/FU)
3	0.000	0.000
2	0.147	0.348
4	0.000	0.001
5	5.440	1.717
1	1.070	0.170

Table 5.1: The difference in ranking between the forcefield and DFT rankings for $Ba_5Nb_4O_{15}$

In the case of $Ba_5Nb_4O_{15}$, the discrepancy between the energy spacings of structures 4 and 5 do not prove problematic, largely due to the fact that only 5 structures are generated in total. However, with increasing structure numbers, a gap of 5 eV/FU could lead to potential structures being missed from the final (and more accurate) energy ranking step.

This is more clearly seen in the case of $Ba_8CoNb_6O_{24}$, as demonstrated in Table 5.2, where the forcefield does not rank the structures in the correct order, indicated by the negative energy from the previous structure. For example, structure 214 is the most stable structure in the DFT rankings (and, as discussed in the previous chapter, matches the experimental structure), with an energy difference of 0.674 eV/FU to the next most stable structure, structure 312. However, in the forcefield screening, structure 312 is 0.136 eV/FU more stable than 214. This pattern is continued throughout the top ten structures, with lack of agreement between the forcefield and DFT energy spacing.

This result can be clearly seen in the distribution below for all the structures generated for the 8 layer structure is shown in Figure 5.4. The distribution shows that a small number of structures are found to be more stable than the experimental structure in the initial screening stage, as demonstrated by a shift to the left of 0.

Structure Number	Δ_{FF} (eV/FU)	Δ_{DFT} (eV/FU)
214	0.000	0.000
312	−0.136	0.674
264	0.123	0.010
142	−1.309	0.033
216	−0.338	0.029
304	−1.228	0.053
213	2.430	0.027
133	0.206	0.122
184	−1.420	0.015
176	−0.473	0.709

Table 5.2: The difference in ranking between the forcefield and DFT rankings for $Ba_8CoNb_6O_{24}$

It therefore becomes clear that this particular forcefield has trouble mirroring the DFT ranking, and it may be possible to identify a forcefield that is able to rank candidate structures with more accuracy, as well as one that is able to maintain the lattice parameters of the experimental structures of $Ba_5Nb_4O_{15}$ and $Ba_8CoNb_6O_{24}$.

It is possible to determine a suitability parameter, Δ_{rank} for each forcefield, based on a summation of the difference between the DFT energy gap and the forcefield energy gap. This is shown in equation below:

$$\Delta_{\mathrm{rank}} = \sum_{n} \frac{(\Delta_{\mathrm{DFT}} - \Delta_{\mathrm{FF}})^2}{{\Delta_{\mathrm{DFT}}}^2} \tag{5.1}$$

where Δ_{DFT} indicates the DFT energy spacing between structures n_1 and n_2, Δ_{FF} indicates the forcefield energy spacing between structures n_1 and n_2, and n is the number of structures

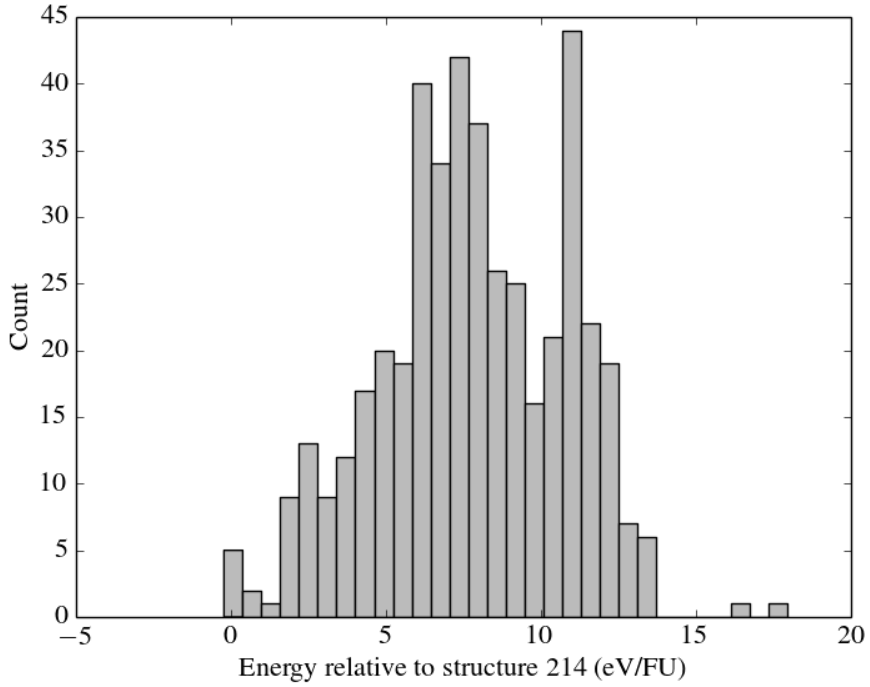

Figure 5.4: Histogram showing the energy distribution of $Ba_8CoNb_6O_{24}$ for the original forcefield, used in the previous study of $Ba_kCo_l\square_mNb_nO_{3k}$

to be compared.

The difference between the DFT energy spacing and the forcefield energy spacing is taken relative to the DFT energy spacing so that the summation is not overpowered by larger energy gaps. For example, using the energy difference between structures 214 and 312 in $Ba_8CoNb_6O_{24}$, we obtain the following when substituting into equation 5.1:

$$\frac{(0.674 - (-0.136))^2}{0.674^2} = 1.44$$

The lower the value, the greater the similarity of the forcefield and DFT rankings. Summing over the lowest 10 energy structures, the original FF gives a value of 18949.5238, as shown in Table 5.3 below:

Structure Number	Δ_{FF} (eV/FU)	Δ_{DFT} (eV/FU)	Δ_{rank}
214	0.000	0.000	0.000
312	−0.136	0.674	1.445
264	0.123	0.010	169.263
142	−1.309	0.033	1503.062
216	−0.338	0.029	159.168
304	−1.228	0.053	580.870
213	2.430	0.027	7698.940
133	0.206	0.122	0.480
184	−1.420	0.015	8834.135
176	−0.473	0.709	2.161

Table 5.3: The difference in ranking between the forcefield and DFT rankings for $Ba_8CoNb_6O_{24}$. The Δ_{FF} and Δ_{DFT} parameters are rounded in the table to 3 d.p, while 8 d.p were used to calculate Δ_{rank}, explaining the minor discrepancies. All calculations were taken relative to the experimental structure (Structure 214).

5.3.2 Looking at a New Forcefield

In the literature, there are a number of reported forcefields to describe the interaction between the different ions present in $Ba_3Nb_2O_8$. Using combinations of these parameters leads to 300 permutations of forcefields.

The forcefields were initially assessed on the basis of differences between the experimental lattice parameters and the forcefield optimised parameters.[†] The forcefields that had the best agreement between the experimental and optimised structures were then taken forward to the next assessment: the geometry optimisation of the top ten structures. The forcefield

[†]The program to combine and assess the forcefields was developed and written by Dr Chris Collins

energy spacing between the top ten structures was compared to the DFT spacing using equation 5.1. Some of the results are shown in the table below:

Forcefield Number	Δ_{rank}
16	18949.5238
31	9484.249224
57	131101.9478
191	3463.001269

Table 5.4: The performance of selected forcefields based on agreement between the DFT and forcefield ranking using equation 5.1, where FF16 is the original forcefield.

Though Δ_{rank} shows how well the FF and DFT ranking agree, we can gain more information looking at the energy distribution. Therefore, all 448 structures for the 8 layer structure were optimised using FF57, which had the highest value of Δ_{rank}, which has the parameters given in Table 5.5.

As can be seen by the histogram shown in Figure 5.5, the experimental structure for the 8 layer compound is found near the centre of the distribution, as indicated by the negative x-axis. The structure found to be most stable in the forcefield run was found to be over 5 eV/FU less stable than the experimental structure following DFT calculations.

The above example demonstrates the logical case of a high value leading to an unsuitable forcefield. However, a low value using equation 5.1 does not necessarily equate to a suitable forcefield. This can be seen with FF31, which has the second lowest value of Δ_{rank} using equation 5.1. It ranks the experimental structure as third most stable.

However, when looking at the energy distribution for the total number of structures (shown below in Figure 5.6), there is no clear energy gap between structures that are more stable

Buckingham Potential			
Interaction	Å(eV)	ρ (eV)	C (eV Å^6)
Nb^{5+} .... O^{2-}[3]	3023.2	0.3000	0.0
Co^{2+} .... O^{2-}[4]	1195.0	0.3087	0.0
Ba^{2+} .... O^{2-}[5]	2096.8	0.3522	8.0
O^{2-} .... O^{2-}[6]	22764.3	0.1490	42.0

Shell Charges		
Ion	Y ($\|e\|$)	k (eV Å^{-2})
Ba^{2+}	1.848	29.10
O^{2-}	−2.240	42.00

Table 5.5: The parameters for forcefield number 57.

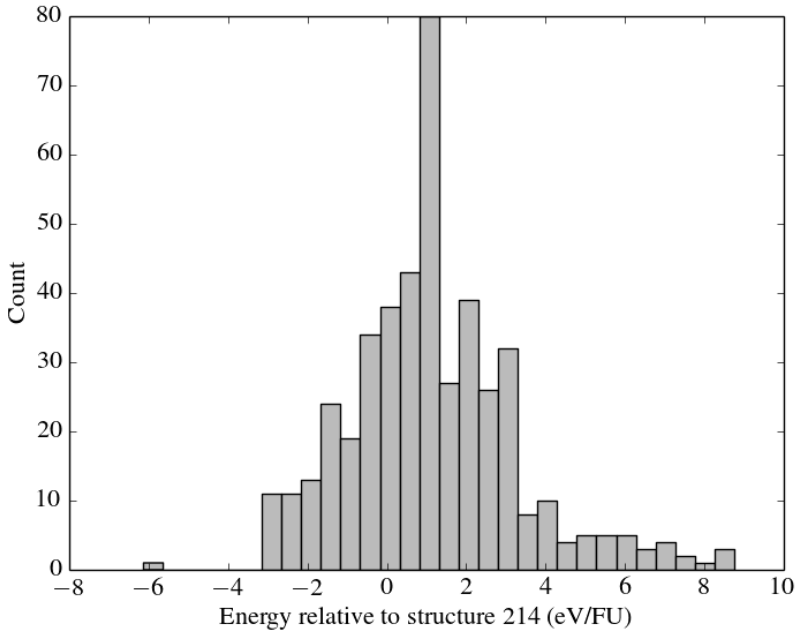

Figure 5.5: Histogram demonstrating the energy distribution of $Ba_8CoNb_6O_{24}$ following forcefield relaxation with FF57.

and those that are less stable. This makes it more difficult to define a clear cut-off energy for the DFT ranking, should this be necessary.

Buckingham Potential			
Interaction	Å(eV)	ρ (eV)	C (eV Å^6)
Nb^{5+} .... O^{2-}[7]	1796.30	0.3460	0.0
Co^{2+} .... O^{2-}[3]	696.3	0.3362	0.0
Ba^{2+} .... O^{2-}[8]	4818.0	0.3067	8.0
O^{2-} .... O^{2-}[6]	22764.3	0.1490	42.0

Shell Charges		
Ion	Y ($\|e\|$)	k (eV Å^{-2})
Nb^{5+}	-4.496	1358.58
Ba^{2+}	1.831	34.05
O^{2-}	-2.240	42.00

Table 5.6: The parameters for forcefield number 31

FF191 also has good agreement with the DFT energy ranking (including ranking the experimental structure as the most stable structure). This forcefield potential also includes a three-body term, adding the bond bending component to the energy. Interestingly, as described in the previous chapter, FF16 originally included a three-body term but it was removed to simplify the forcefield so that only single-body potentials were used. In this case, the decision was made to keep the three-body term, due to the success of the forcefield in maintaining lattice parameters and matching the DFT ranking.

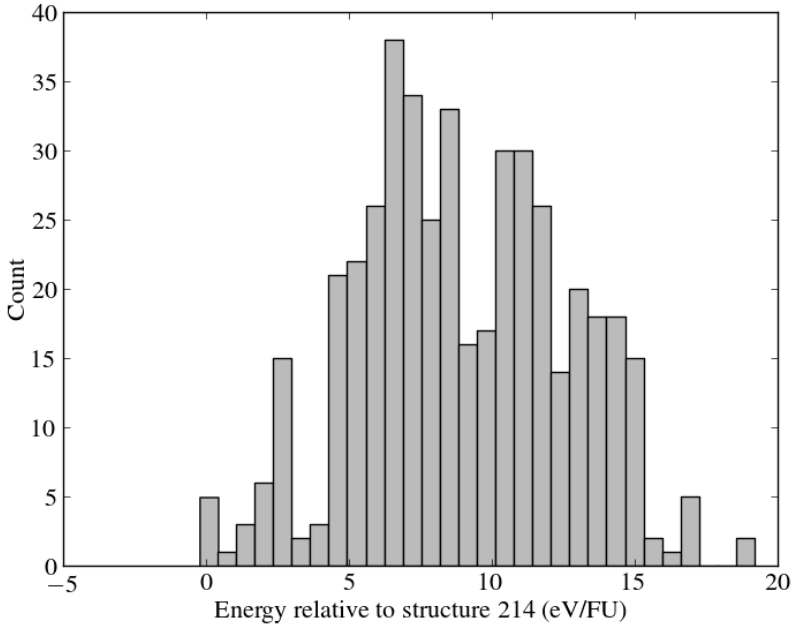

Figure 5.6: Histogram demonstrating the energy distribution of $ba_8CoNb_6O_{24}$ following forcefield relaxation with FF31

As shown by Figure 5.7, there is also a clear gap defining the most stable structures. This makes the decision of which structures to take forward to the DFT ranking more straightforward. A summary of FF191 is given below in Table 5.8, showing good agreement between the experimental structure and forcefield optimised structures.

5.3.3 Application to $Ba_3Nb_2O_8$

Based on the considerations described above, FF191 was used to perform the initial screening of $Ba_3Nb_2O_9$. Following the FF optimisation stage, a number of structures were selected and their relative ranking was reassessed following DFT calculations.

In the previous chapter, this number was chosen based on consideration of the energy distributions and the amount of computing resources available. For the study of $Ba_3Nb_2O_8$, a more sophisticated approach was taken to eliminate the somewhat arbitrary number of DFT calculations.

Buckingham Potential			
Interaction	Å(eV)	ρ (eV)	C (eV Å^6)
Nb^{5+} .... O^{2-}[9]	1425.0	0.365	0.0
Co^{2+} .... O^{2-}[4]	1195	0.3087	0.0
Ba^{2+} .... O^{2-}[8]	4818.0	0.3067	8.0
O^{2-} .... O^{2-}[6]	22764.3	0.1490	27.88

Shell Charges		
Ion	Y ($\|e\|$)	k (eV Å^{-2})
Ba^{2+}	1.831	34.05
O^{2-}	−2.90	70.00

Three Body Term		
Bond	k_θ (eV rad^{-2})	θ_0 (°)
O_{shell} - Nb_{core} - O_{shell}	0.5776	90.0

Table 5.7: The parameters for forcefield number 191

Parameter	Exp.	FF	% difference
a (Å)	5.89	5.93	0.64
b (Å)	5.89	5.93	0.63
c (Å)	12.00	11.98	-0.15
Volume (Å^3)	360.95	365.01	1.12

Table 5.8: A comparison of the lattice parameters of $Ba_8CoNb_6O_{24}$ before and after geometry optimisation using forcefield 191

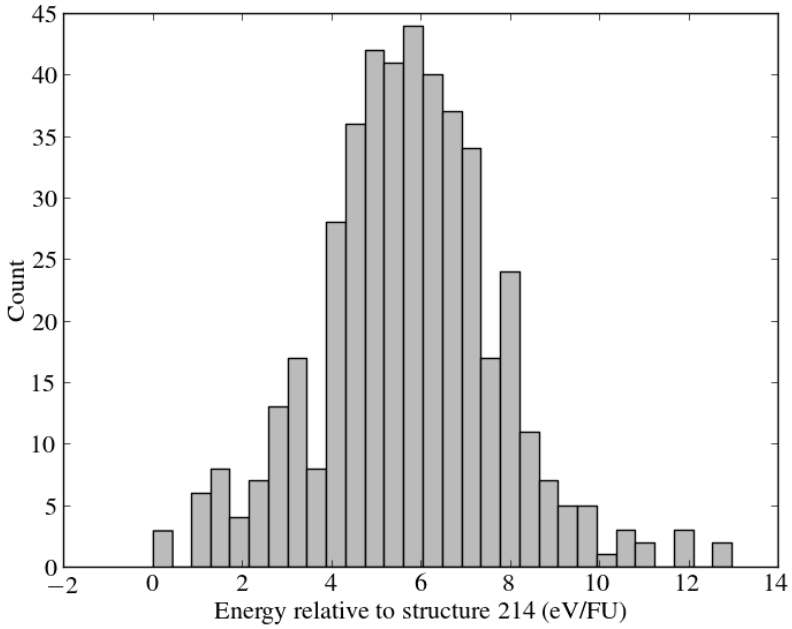

Figure 5.7: Histogram showing the energy distribution of $Ba_8CoNb_6O_{24}$ following relaxation with FF191

The study of $Ba_8CoNb_6O_{24}$ revealed repeated structures in the final ranking stage. Repeated structures can occur for several reasons, and could theoretically happen at different points in the EMMA screening process. For instance, structures may be different after forcefield optimisation but may move towards the same structure during DFT optimisation. It may also be the case that structures assembled with layers in different combinations could move towards the same structure during forcefield optimisation.

Consequently, for the study of $Ba_3Nb_2O_8$, structures were assessed following forcefield optimisation for similarities in unit cell and symmetry, using a tolerance factor to account for minor differences in atomic positions.[‡] It was found that in the lowest ranked 500 structures, a number of structure types occurred more than once, and there were a total of 61 unique structures (subsequently identified based on first appearance). An abridged version of the results are shown below in Table 5.9.

[‡]The program to assess structure similarity was developed and written by Dr Matthew Dyer

Structure ID	Occurrences	Energy (eV)
S-0	1	−1262.57
S-1	1	−1262.16
S-2	81	−1262.03
S-83	20	−1261.89
S-171	267	−1261.04

Table 5.9: A summary of the repeated structures in the lowest ranked 500 structures for $Ba_3Nb_2O_8$

The repetition of structures provides information about the potential energy surface. For example, S-171 is repeated over 250 times in the lowest ranked 500 structures. This indicates that the local minimum around S-171 is broad. In addition, when comparing the Vanderah structure using the same forcefield, all of the above structures are ranked as more stable, with an energy difference of over 0.5 eV/FU. This indicates that there may be other promising structures at this composition than those already identified to date.

5.4 DFT Calculations

DFT calculations were performed for any significantly repeated structures (defined as structures occurring more than five times) and structures ranked lowest in energy, summarised in Table 5.10.

As can be seen from Table 5.10, when ranked using DFT energies, the Vanderah structure becomes the most stable structure. This is somewhat disconcerting when considering the energy distribution following forcefield optimisation, as the Vanderah structure does not appear in the first 500 structures, and is found in the middle of the energy distribution, as highlighted in Figure 5.9, where the position of the Vanderah structure is shown by the

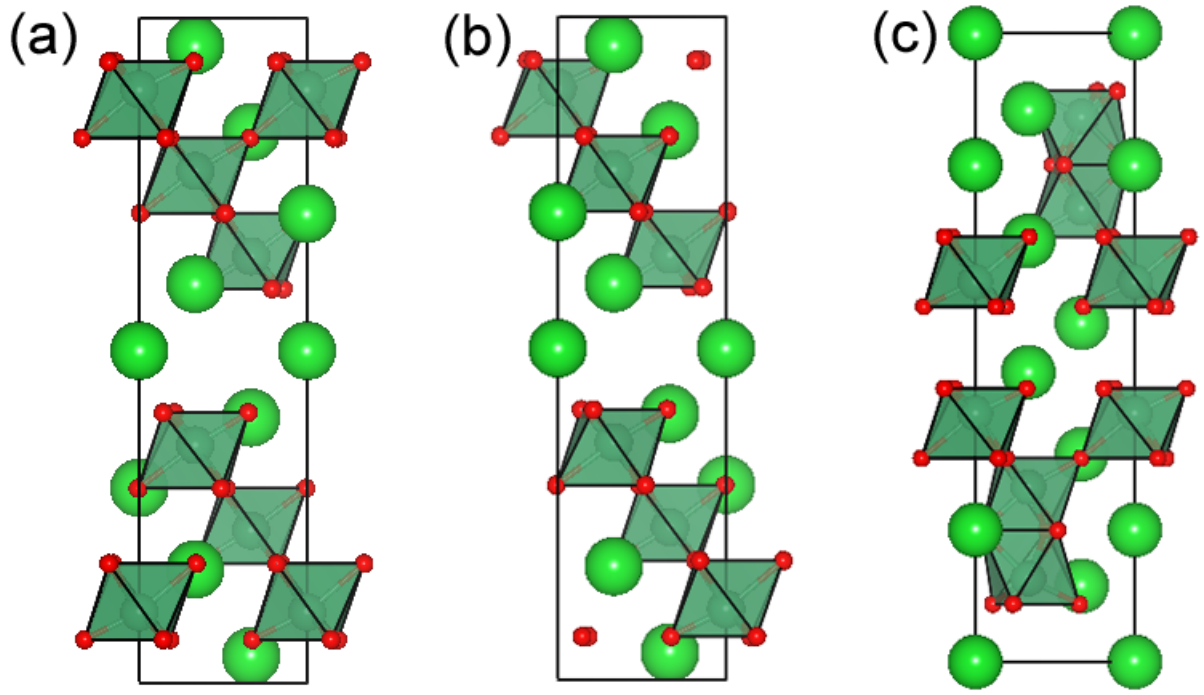

Figure 5.8: Possible structures of $Ba_3Nb_2O_8$. These structures were identified as promising due to repetition within the lowest ranked 500 structures: (a) S-2 (b) S-83 (c) S-171

dashed line. It may also be the case that other promising candidate structures are omitted due to their apparent instability using this particular FF.

One of the reasons for the Vanderah instability in this particular forcefield may be due to the presence of tetrahedrally coordinated niobium environments. The compositional series $Ba(Co,Nb)_{1-\delta}O_3$ investigated in the previous chapter comprised of only octahedral coordination environments. It may be the case that the octahedrally coordinated environments are heavily favoured, particularly as the FF was chosen based on the continuity of the ranking between the FF and DFT calculations for structures with ions coordinated octahededrally. It is likely that the inclusion of the three-body term favoured a particular coordination environment.

It is interesting to note that the most favourable structure from the EMMA candidates (S-171) possesses face-sharing octahedra. Therefore, another screening mechanism may be to look for particular stacking sequences that are known to be favoured. However, this involves

Structure	TOTEN (eV)	E (eV/FU)	E1 (eV/FU)	E2 (eV/FU)
BaO	−11.81	−11.81	-	-
$Ba_5Nb_4O_{15}$	−192.34	−192.34	-	-
$Ba_4Nb_2O_9$	−344.41	−114.80	-	−0.92
$Ba_3Nb_2O_8$ (S-0)	-	−101.77	+0.61	+0.31
$Ba_3Nb_2O_8$ (S-1)	−303.53	−101.18	+1.21	+0.90
$Ba_3Nb_2O_8$ (S-2)	−306.21	−102.07	+0.31	+0.01
$Ba_3Nb_2O_8$ (S-83)	−306.17	−102.06	+0.33	+0.02
$Ba_3Nb_2O_8$ (S-171)	−306.60	−102.21	+0.18	−0.12
$Ba_3Nb_2O_8$ (Vanderah)	−307.09	−102.36	+0.02	−0.29

Table 5.10: A summary of the DFT calculations on candidate structures for $Ba_3Nb_2O_8$
E1 = energy compared to $\frac{1}{3}(Ba_4Nb_2O_9 + Ba_5Nb_4O_{15})$
E2 = energy compared to $\frac{1}{2}(Ba_5Nb_4O_{15} + BaO)$

prior knowledge of the family of compounds, which may be unavailable.

In addition, none of the proposed structures match with the experimental NMR observations.[§] It is likely that the preference for octahedral coordination environments distorts the energy distribution, making tetrahedral coordination environments unfavourable, and hence there may be interesting structures lost in the forcefield ranking stage. In addition, the occupancy question is difficult to address using forcefields, and it is possible that vacancy systems exist in larger unit cells than those constructed in this study.

[§]Private correspondence with Dr John Hanna at the University of Warwick

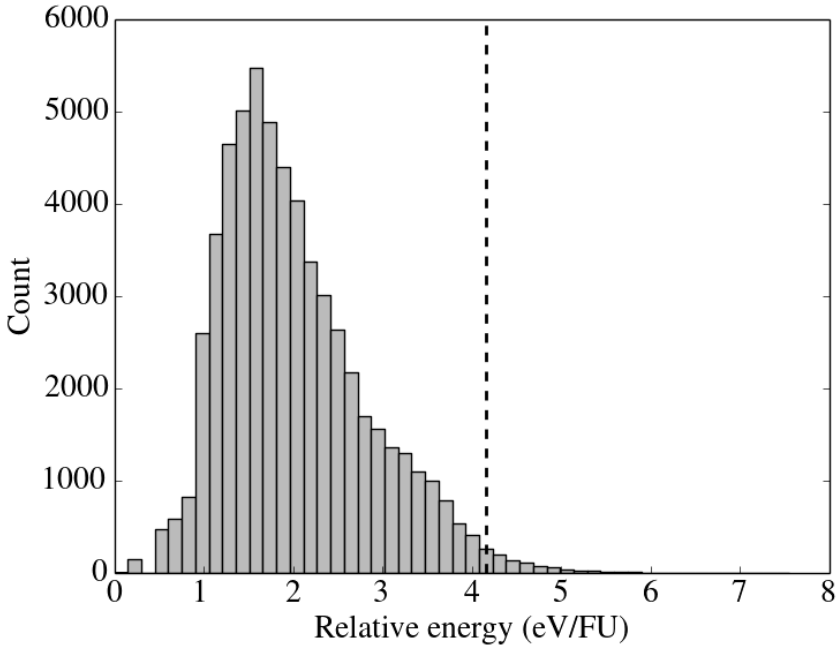

Figure 5.9: Histogram showing the energy distribution of $Ba_3Nb_2O_8$ for FF191, where the dashed line indicates the position of the Vanderah structure.

5.5 Conclusions

The study of $Ba_3Nb_2O_8$ led to some key improvements in the EMMA process, most notably identifying repeated structures to limit and direct the number of calculations needed at the DFT stage. However, the preference for octahedrally coordinated environments over tetrahedrally coordinated environments means that candidate structures that possess the latter are overlooked and lost in the energy distribution. It is possible that the structure of $Ba_3Nb_2O_8$ was generated in the EMMA assembly but ranked too low to be considered as a serious candidate.

The forcefield choice was difficult for this structure due to the fact that niobium can be either tetrahedrally coordinated or octahedrally coordinated, and the ideal forcefield would favour both equally so that both environments could be considered fairly.

This study demonstrates clearly the advantages and disadvantages of forcefield calculations. The calculations are computationally inexpensive, which means that hundreds of thousands

(if not more) of structures can be energetically ranked. However, the success of this ranking is entirely dependent on the suitability of the forcefield for any given structure. This point becomes increasingly difficult as less is known about the structure, as there are no avenues for comparison. Therefore, future work must move away from the use of forcefields towards *ab initio* methods or towards the development of more robust forcefields. This will hopefully become more possible with greater computing resources and eventually lead to the solutions of structures for compounds such as $Ba_3Nb_2O_8$.

References

1. Vanderah, T. A., Collins, T. R., Wong-Ng, W. & Roth, R. S. Phase equilibria and crystal chemistry in the BaO–Al_2O_3–Nb_2O_5 and BaO–Nb_2O_5 systems. *Journal of Alloys and Compounds* **346,** 1–13 (1–2 2002).

2. Kemmler-Sack, S. V. & Treiber, U. On hexagonal perovskites with cationic vacancies. *Anorganische Und Allgemeine Chemie* **478,** 198–204 (1981).

3. Woodley, S. M., Battle, P. D., Gale, J. D. & Catlow, R. A. The prediction of inorganic crystal structures using a genetic algorithm and energy minimisation. *Physical Chemistry Chemical Physics* **1,** 2535–2542 (1999).

4. Hart, F. X. & Bates, J. B. Lattice model calculation of the strain energy density and other properties of crystalline $LiCoO_2$. *Journal of Applied Physics* **83,** 7560–7566 (1998).

5. Islam, M. S. & Winch, L. J. Defect chemistry and oxygen diffusion in the $HgBa_2Ca_2Cu_3O_{8+\delta}$ superconductor: A computer simulation study. *Physical Review B* **52,** 10510 –10515 (1995).

6. Lewis, G. V. & Catlow, R. A. Potential models for ionic oxides. *Journal of Physics C: Solid State Physics* **18,** 1149–1161 (6 1985).

7. Baetzold, R. C. Calculations of defect properties important in photorefractive $Sr_{0.6}Ba_{0.4}Nb_2O_6$. **48,** 5789 –5796 (1993).

8. Pirovano, C., Islam, M. S., Vannier, R. N. & Nowogrocki, G. Modelling the crystal structures of Aurivillius phases. *Solid State Ionics* **140,** 115 –123 (2001).

9. Jackson, R. A. & Valerio, M. E. G. A new interatomic potential for the ferroelectric and paraelectric phases of $LiNbO_3$. *Journal of Physics: Condensed Matter* **17,** 837–843 (2005).

Chapter 6

Investigation of $(x)\mathbf{LiMgPO_4} + (1-x)\mathbf{Li_2MgSiO_4}$

Abstract

$LiMgPO_4$ and Li_2MgSiO_4 can be described using similar structural motifs due their close-packed oxide lattices with cations present in the interstitial sites. Using this fact, it is possible to generate a superlattice with the composition of $(x)LiMgPO_4 + (1-x)Li_2MgSiO_4$. The proposed composition is investigated using a combination of forcefield calculations and density functional theory (DFT). The suggested structures are first evaluated using forcefield optimisation with Monte Carlo site swapping, and the stability of the suggested composition is then assessed using DFT energies. It is hoped that new structures could be experimentally synthesised, building on the promising work on $LiMgPO_4$ that suggests it may be a lithium-ion conductor.

6.1 Introduction

Lithium-ion batteries are important for energy storage in a wide variety of applications, such as consumer electronics and transportation.[1,2] Recently, attention has shifted from the conventional Li^+ ion batteries to the development of fast solid-state Li^+ ion conductors, due to their function as electrolytes in all solid-state Li^+ batteries, which are less flammable than their organic liquid counterparts.[3] However, low bulk Li^+ ion conductivity at room temperature in solid-state Li electrolytes remains a key challenge, alongside environmental issues and electrochemical stability.[4]

There are several lithium-based materials that have been investigated for use in solid-state electrolytes, such as sulphide and oxide compounds. More recently, $LiFePO_4$ (LFP)[5] has emerged as a key cathode material due to its stable olivine structure. In contrast with other Li cathode materials that adopt perovskite and spinel structures, which may allow for the release of oxygen, the strong P - O bonds in LFP prevent this in the case of explosion, and as a result, LFP-based batteries do not need as intense monitoring systems as in other Li-ion batteries.[6]

One approach that can facilitate the discovery of new electrode materials involves chemical substitution in known Li electrode compounds, with a key feature being Li^+ ion diffusion for intercalation and deintercalation.[7] A range of aliovalent and isovalent substitutions have been explored in $LiFePO_4$, with five possible substitution mechanisms currently known.[8] $LiMgPO_4$ is known to also adopt the olivine structure (shown in Figure 6.1), and comprises of non-toxic materials. It is predicted to have a low barrier to Li^+ ion diffusion of 0.3 eV, comparable to that of known Li^+ ion conductors. The structure contains tetrahedral PO_4 and octahedral LiO_6 and MgO_6 groups, where the inversion site is occupied by Li^+ ions and the mirror site is taken by Mg^{2+} ions.[9]

The structure of $LiMgPO_4$ can hence be thought of as a network of PO_4 tetrahedra populated

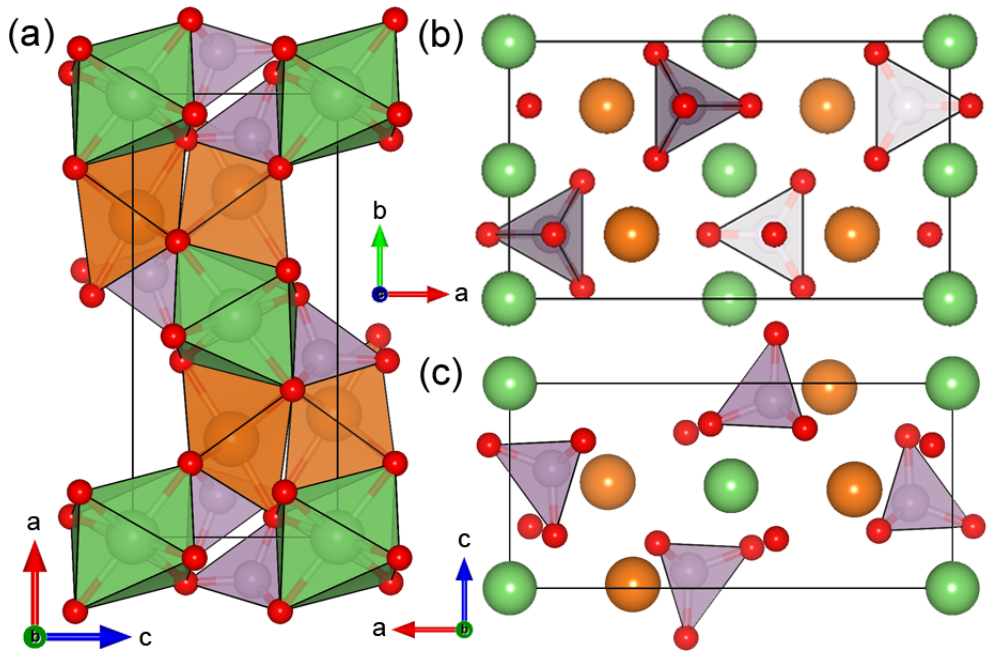

Figure 6.1: The structure of $LiMgPO_4$ viewed from different orientations. The green atoms represent Li; orange Mg; red O and purple P.

by Li^+ and Mg^{2+} interstitial cations. The compound Li_2MgSiO_4 also contains a network of SiO_4 tetrahedra in similar positions to the PO_4 tetrahedra described for $LiMgPO_4$, however the Li^+ and Mg^{2+} cations also occupy tetrahedra, forming a three-dimensional framework of shared tetrahedra vertices, shown in Figure 6.2.[10] A study was recently performed on the similar Li_4SiO_4 - Li_3PO_4 system, with simulations reporting that ionic conductivities are calculated to be orders of magnitude higher in the mixed phase in comparison with the end members.[11]

It is therefore possible to envisage compounds of the series $(x)LiMgPO_4 + (1-x)Li_2MgSiO_4$, connected by a network of PO_4 and SiO_4 tetrahedra populated with interstitial cations and vacancies, as demonstrated in Figure 6.3. Though Li_2MgSiO_4 is more known for its dielectric properties,[12] the combination with $LiMgPO_4$ offers a potential avenue for better Li^+ ion conductivity due to the combination of partially occupied octahedral and tetrahedral sites.

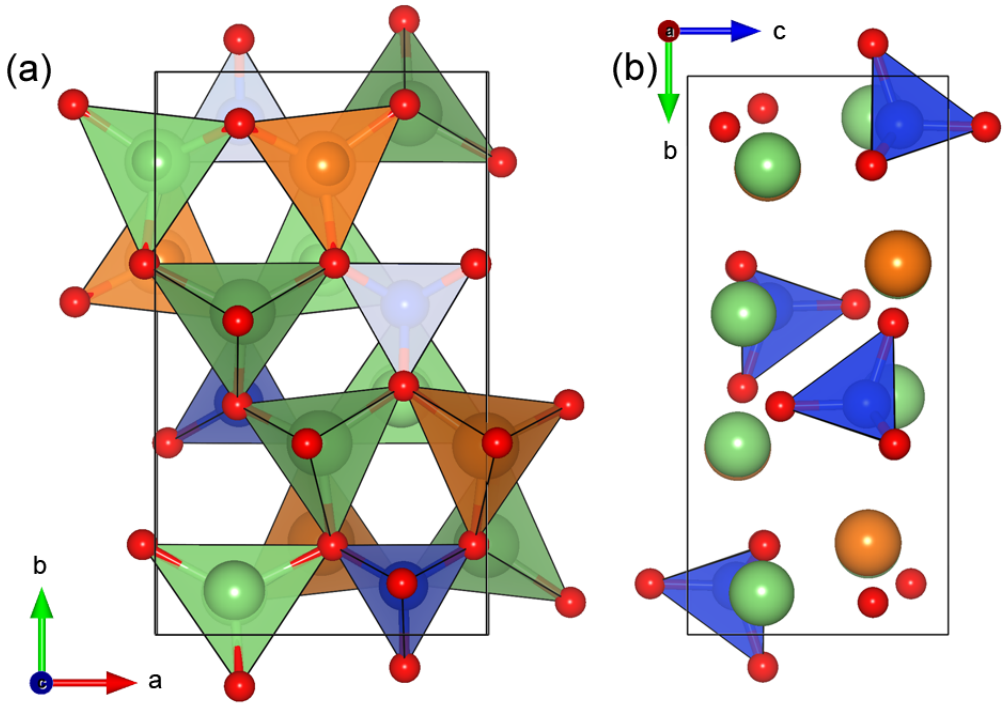

Figure 6.2: The structure of Li_2MgSiO_4 viewed from different different orientations. The green atoms represent Li; orange Mg; red O and blue Si.

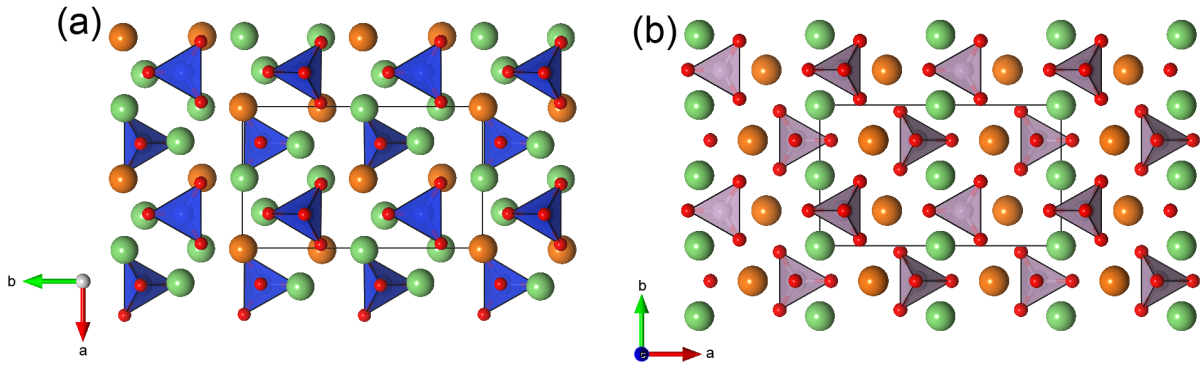

Figure 6.3: A comparison of the structures of (a) Li_2MgSiO_4 and (b) $LiMgPO_4$. A general lattice can be built around the SiO_4 and PO_4 tetrahedra, populated by lithium, magnesium and vacancies to describe mixed phases.

6.2 Methodology

While both $LiMgPO_4$ and Li_2MgSiO_4 have structures that can be described in modular units, a site-swapping mechanism was deemed more appropriate to investigate the system of $LiMgPO_4$ - Li_2MgSiO_4, largely due to the fact that the structures are easily visualised in

terms of octahedral and tetrahedral sites, populated by lithium, magnesium or vacancies and silicon or phosphorus, respectively. This means that it is possible to envisage a routine in which ions (or vacancies) are swapped between possible sites and the swap is either accepted or rejected based on particular criteria.

In this case, two criteria were used to assess to validity of a swap. Firstly, a comparison of the total energies to ascertain whether the new structure is more energetically favourable. Secondly, a Monte Carlo acceptance criteria was used based on the Boltzmann distribution, with a specified reduced temperature. This ensures that the routine does not get trapped in a local minimum, as described in Chapter 3. As with the EMMA procedure, the swaps are initially assessed based on forcefield energies, due to the computational expense of DFT. Any promising structures were then re-examined using DFT.

6.3 Buckingham Potential

The choice of forcefield has a large impact on results, particularly when investigating unknown compounds where certain bonding geometries may be favoured. However, in this case, the structures of both end members are known and the bonding geometries in the compositional series are highly likely to be similar, which means that the choice of forcefield can be made based on comparison of the lattice parameters and coordination geometries following structure optimisation to that of the initial structure.

Due to the ionic nature of both $LiMgPO_4$ and Li_2MgSiO_4, a Buckingham potential was used. The parameter set was taken from a variety of sources[13–15] and matched to the experimental structures as described above. The potential is summarised below in Table 6.1. The forcefield is able to maintain the unit cell volumes of both $LiMgPO_4$ and Li_2MgSiO_4 well, with a minor expansion of 0.98% in the former and a minor contraction of 1.05% in the latter. In addition, the bond angles are preserved for both.

In addition, since one of the key components of this study revolves around the octahedral and tetrahedral interstitial sites populated in the oxide lattice, it is important that the forcefield is able to maintain these coordination polyhedra as distinct sites. Therefore, a comparison between the coordination polyhedra has been made in both $LiMgPO_4$ and Li_2MgSiO_4 and is summarised in Table 6.3 below, with a schematic of each polyhedron shown in Figure 6.4.

Buckingham Potential			
Interaction	Å(eV)	ρ (eV)	C (eV Å)
Li^{+} .... O^{2-}	632.1018	0.2906	0.0
Mg^{2+} .... O^{2-}	1428.5000	0.2945	0.0
P^{5+} .... O^{2-}	897.2648	0.3577	0.0
Si^{4+} .... O^{2-}	1283.910	0.3205	10.7
O^{2-} .... O^{2-}	22764.3	0.1490	42.0

Shell Charges		
Ion	Y ($\|e\|$)	k (eV $Å^{-2}$)
O^{2-}	-2.96	65.00

Three-body term		
Bonds	k_θ (eV rad^{-2})	θ_0 (deg)
O_{shell} - P_{core} - O_{shell}	1.35578	109.47

Table 6.1: The cut-off limit for all interactions was set to 12 Å.

In general, the Buckingham potential set is able to model the local structures fairly well.

Compound	Initial Value	Final Value	Difference
$LiMgPO_4$	281.3259	284.0745	2.7486 (+0.98%)
Li_2MgSiO_4	336.4499	332.9216	3.5283 (−1.05%)

Table 6.2: The unit cell volumes (Å^3) of $LiMgPO_4$ and Li_2MgSiO_4 following forcefield relaxation.

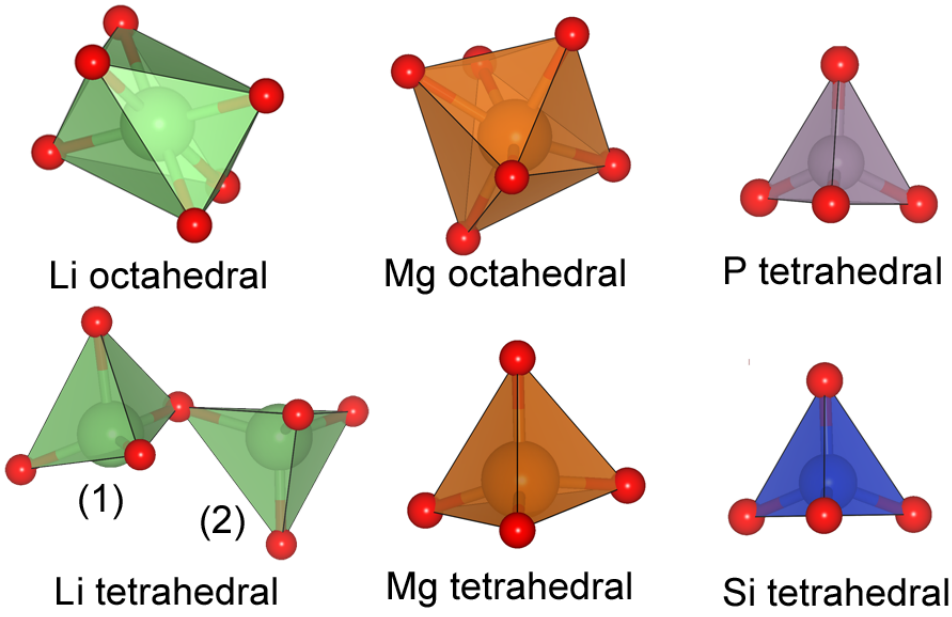

Figure 6.4: Representations of the polyhedra found in $LiMgPO_4$ and Li_2MgSiO_4

The largest difference is seen in the Mg octahedral site, where significant differences are observed in the average bond length and effective coordination number, and in particular a large expansion of the polyhedral volume is observed.

6.3.1 Experimental Compositions

To investigate the structure of $LiMgPO_4$, an oxide lattice populated with PO_4 tetrahedra was constructed, while for Li_2MgSiO_4 the oxide lattice was populated with SiO_4 tetrahedra. The cells were then randomly populated over both the tetrahedral and octahedral sites with lithium and magnesium ions, matching the experimental composition. In addition, a vacancy

Site	Average bond length (Å)	Volume (Å^3)	Coordination Number
$LiMgPO_4$			
Li octahedral	2.20 (+2.82%)	13.14 (+6.60%)	5.98 (+0.54%)
Mg octahedral	2.18 (+3.49%)	12.90 (+8.93%)	5.54 (−5.25%)
P tetrahedral	1.52 (−1.46%)	1.79 (−4.02%)	4.00 (+0.22%)
Li_2MgSiO_4			
Li1 tetrahedral	1.96 (−0.46%)	3.76 (−2.60%)	3.93 (+0.82%)
Li2 tetrahedral	2.02 (−0.39%)	3.75 (−2.92%)	3.78 (+3.89%)
Mg tetrahedral	1.94 (−0.71%)	3.65 (−2.07%)	3.99 (+0.02%)
Si tetrahedral	1.64 (0.00%)	2.26 (−0.04%)	4.00 (+0.05%)

Table 6.3: A summary of the coordination polyhedra in $LiMgPO_4$ and Li_2MgSiO_4 following forcefield relaxation, with the percentage difference compared to the experimental structure. There are two distinct lithium tetrahedral sites in Li_2MgSiO_4, as shown in Figure 6.4.

site was created by the insertion of an atom 'X'. This atom is deleted once the forcefield relaxation step begins, but it is necessary so that swaps can occur between populated and unpopulated sites. For both compositions, the unit cell was multiplied to give a supercell containing 16 oxygen ions. An example of the starting structures for both compounds is shown in Figure 6.5.

As the initial population of lithium and magnesium ions over the octahedral and tetrahedral sites is random, it was decided that the site-swapping should occur over four distinct starting structures to maximise the possibility of finding the experimental structure. An initial forcefield relaxation of the candidate starting structure was completed to ensure the viability of the starting structure for subsequent Monte Carlo steps. If the structure did not converge, it was rejected, and the ions were randomly distributed over the sites again.

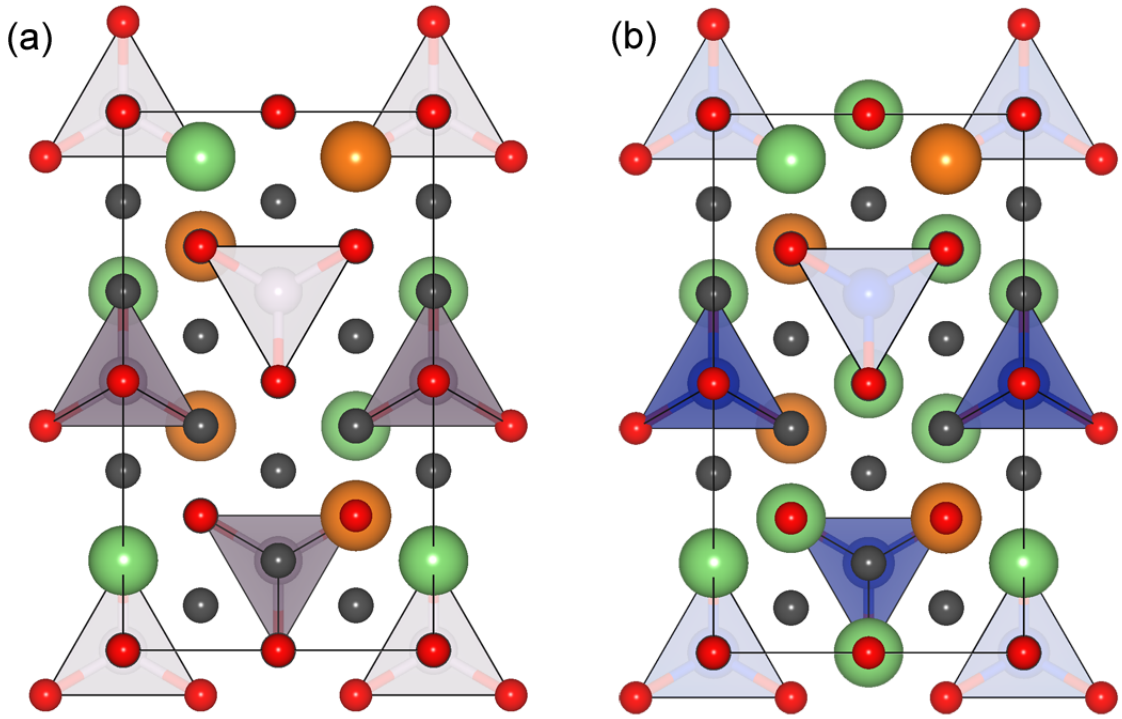

Figure 6.5: The starting points for (a) $LiMgPO_4$ and (b) Li_2MgSiO_4. The grey atoms represent dummy atoms for vacancy sites.

For both compositions, four unique starting structures were generated, giving four separate runs of the Monte Carlo site swapping routine. Each run was given 1000 steps to attempt to swap between Li, Mg and vacancy sites, while the reduced temperature for the Monte Carlo acceptance was set to 1 eV^{-1}, given by the expression:

$$T^* = \frac{k_b T}{\varepsilon} \tag{6.1}$$

where T^* is the reduced temperature, as defined in reference to units of k_b and the energy scale.

$LiMgPO_4$

The experimental structure of $LiMgPO_4$ was found to be the lowest energy structure in three out of four runs, confirmed by both inspection and space group analysis using FINDSYM.

In the first three runs, the experimental structure was found multiple times in the ten lowest energy structures for that run, as demonstrated in Figure 6.6.

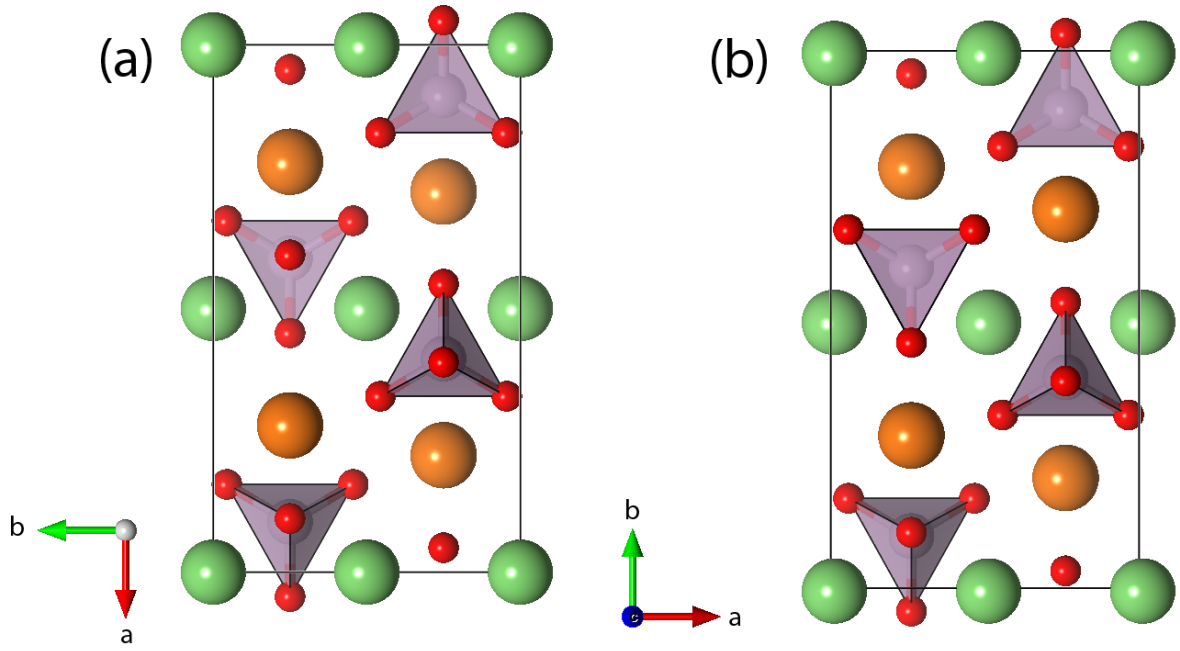

Figure 6.6: A comparison of the experimental structure for $LiMgPO_4$ (a) with the lowest energy structure identified in the Monte Carlo site swapping routine (b). They share the same structure, which can be identified by rotation of the axes.

Run	1	2	3	4
FF (eV/FU)	0.0001	0.0000	0.0000	+0.2051
DFT (eV/FU)	−0.0016	0.0000	0.0000	+0.1696

Table 6.4: A comparison of the lowest energy structures found in each run in the study of $LiMgPO_4$. The energies shown are relative to the experimental structure.

However, it was not found in the fourth run, as the lowest energy structure was found to be 0.2 eV/FU less stable than the experimental structure. The lowest energy structure from each run was also relaxed using DFT. The results are summarised below in Table 6.4. In addition, the starting structure and end structures are shown in Figure 6.7.

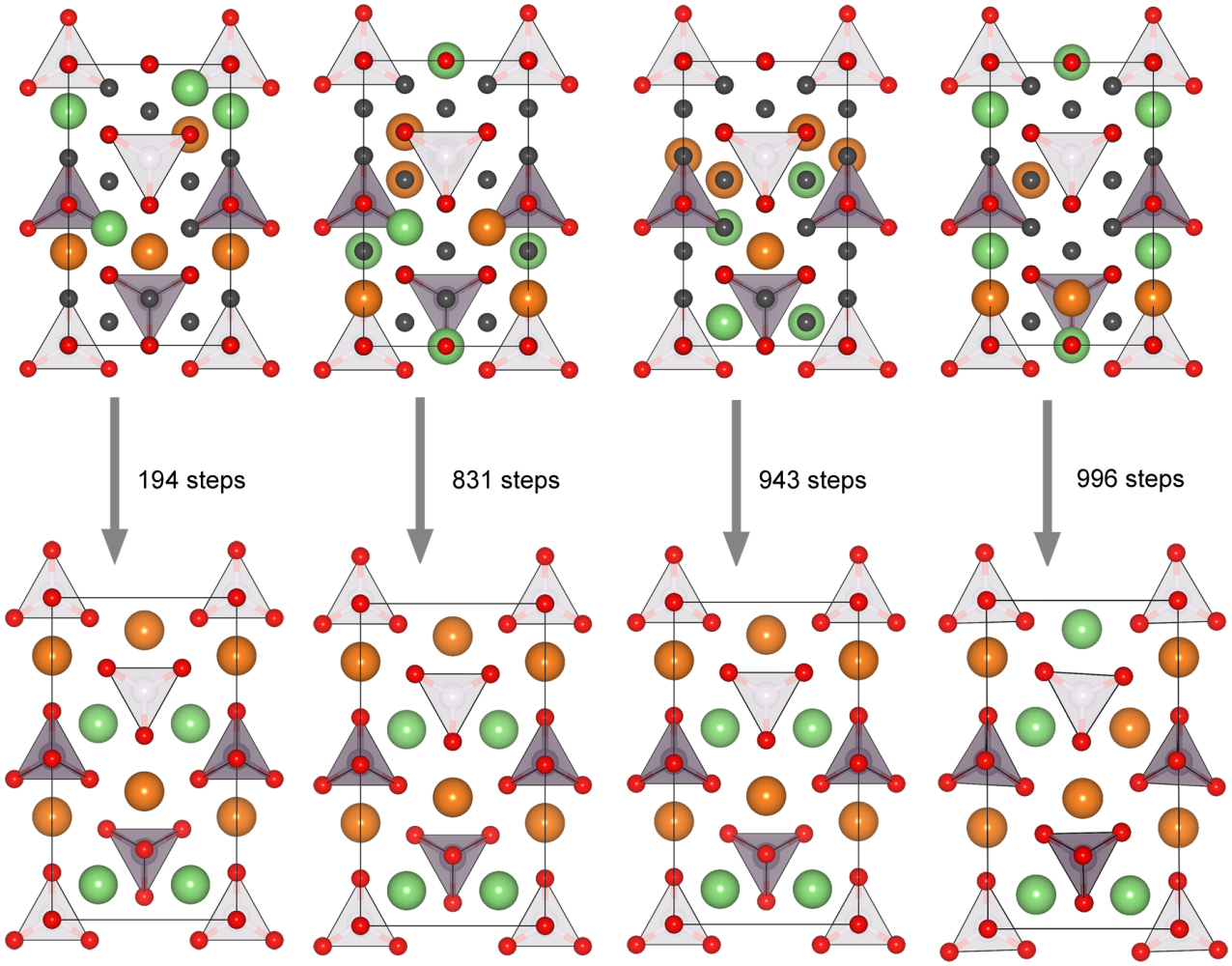

Figure 6.7: Summary of the various starting points and number of steps needed to reach the lowest energy structure for $LiMgPO_4$.

Li_2MgSiO_4

The study of Li_2MgSiO_4 was more problematic than the study of $LiMgPO_4$. Only one of the four runs approached the energy of the experimental structure, as shown in Table 6.5. The structure found in run 2 was found to be very similar to that of the experimental energy, with a 0.01 eV/FU difference, which demonstrates the small differences in energies between different polymorphs. The lowest energy structures from each run are shown below in Figure 6.8.

Run	1	2	3	4
FF (eV/FU)	+0.1406	+0.0107	+0.3840	+0.1970
DFT (eV/FU)	+0.1912	+0.0671	+0.4769	+0.2587

Table 6.5: A comparison of the lowest energy structures found in each run in the study of Li_2MgSiO_4. The energies shown are relative to the experimental structure.

In general, the DFT energy rankings match the forcefield energy rankings. However, DFT energies appear to discriminate between the energies better, with a larger energy gap found between the experimental structure and the lowest energy structure identified in run 2.

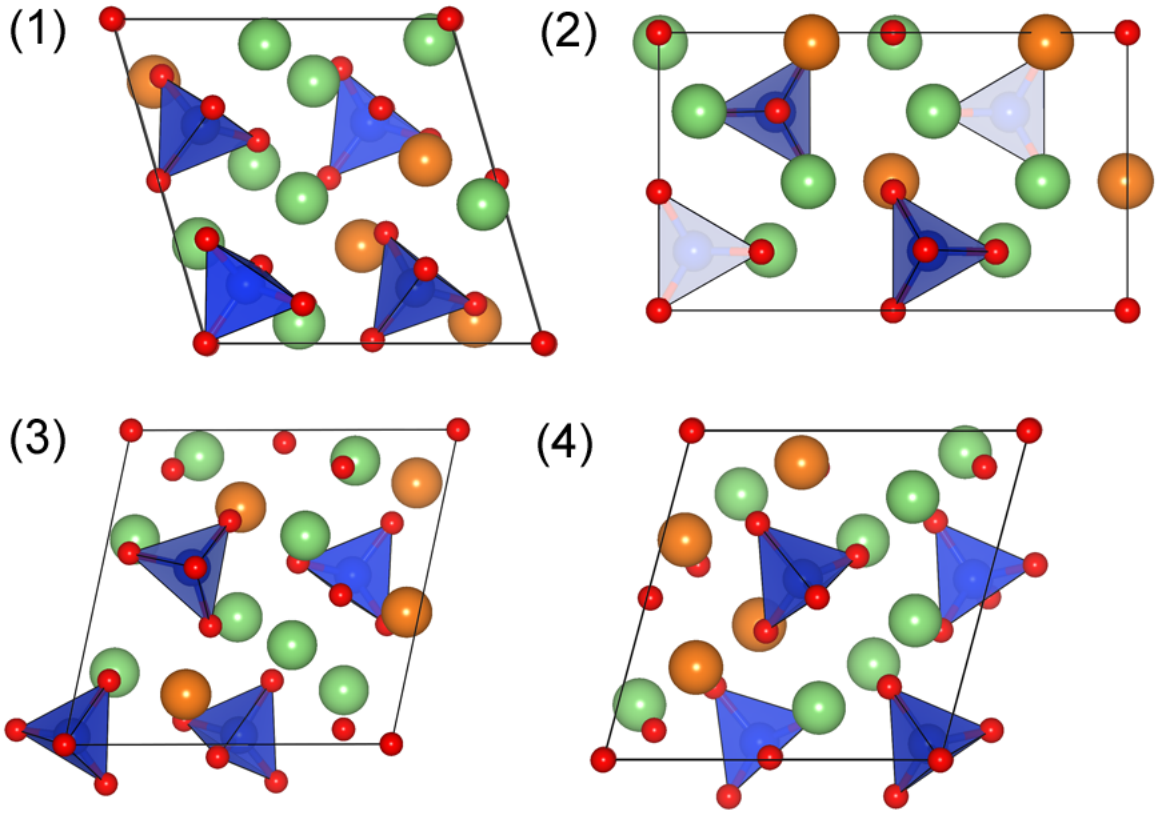

Figure 6.8: The lowest energy structure found in each run for Li_2MgSiO_4 using the Buckingham potential

On inspection of the most stable structures from each run, it is clear that the Buckingham potential used in the study has more difficulty maintaining the unit cell parameters for cells with composition Li_2MgSiO_4. This is even seen in the starting structures following

relaxation, where some distortion has taken place from the ideal oxide lattice generated. However, the structure shown in Figure 6.8 (2) is moving towards the experimental structure, which demonstrates that the forcefield is able to model the structure in certain cases. In addition, it is also possible that the experimental structure would have been found with more Monte Carlo steps.

6.3.2 $x = 0.5$

The site-swapping code was found to have success with $LiMgPO_4$ and moderate success with Li_2MgSiO_4, which makes it possible to investigate novel compositions in the series with only minor modifications to the process. In the case of a mixed composition, the oxide lattice must be populated with both PO_4 and SiO_4 tetrahedra, and swaps must occur between these sites relative to swaps between the lithium, magnesium and vacancy sites. Initially, a swap ratio of 5:1 was chosen, meaning that for every Si/P swap, five Li/Mg/X swaps take place. The composition $x = 0.5$ was chosen, to give an overall composition of $Li_{1.5}MgP_{0.5}Si_{0.5}O_4$. Due to the necessity of having integer compositions, the cell was constructed as $Li_6Mg_4P_2Si_2O_{16}$, which also allows for investigations of $x = 0.25$ and $x = 0.75$ in the future.

Structure	FF	Stability (eV/FU)	DFT (eV)	Stability (eV/FU)
1-205	−913.9674	+0.0848	−195.2848	+0.2791
2-688	−913.9283	+0.0945	−195.2237	+0.2944
4-672	−913.6786	+0.1570	−194.9655	+0.3589
4-961	−913.6165	+0.1725	−195.0488	+0.3381
4-714	−913.5083	+0.1995	−194.9872	+0.3535

Table 6.6: Table showing the five lowest energy structures from the Monte Carlo site swapping run. Each structure was named based on the run number and step, e.g. structure 1-205 was identified on run 1, step 205. The stability is taken relative to $\frac{1}{2}(LiMgPO_4 + Li_2MgSiO_4)$

The results for $x = 0.5$ are shown above in Table 6.6, with the lowest energy structure shown for each run in Figure 6.9. Due to the more complex structures investigated with $x = 0.5$, the forcefield was found to have more trouble with the structural optimisation steps, largely due to the shells on the oxygen ions becoming detached from their cores. In addition, many of the structures that were relaxed were not able to reach the required convergence conditions for the geometry optimisation. This problem was not experienced at the experimental compositions, but is experienced in the mixed compositions due to the increase in both complexity and unit cell size.

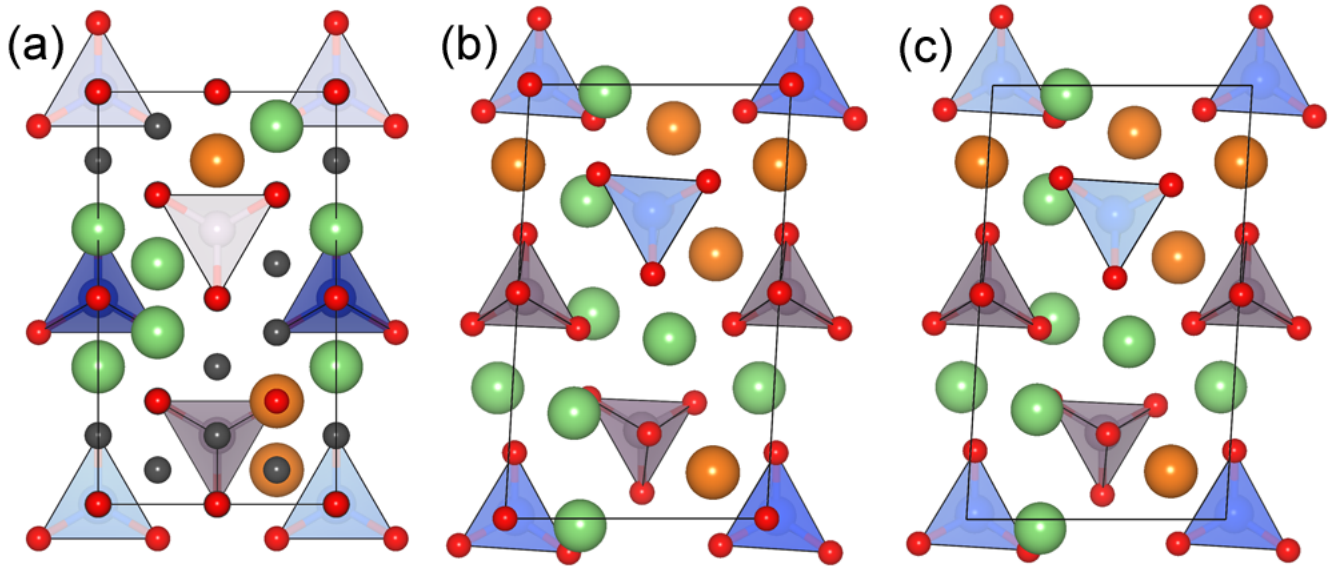

Figure 6.9: (a) The starting structure for run 1 (b) The lowest energy structure identified in the Monte Carlo site swapping process (1-205) and (c) The structure of 1-205 following DFT relaxation.

The two lowest energy structures have fairly similar energies both with FF and DFT calculations. All structures were found to be unstable relative to $\frac{1}{2}(LiMgPO_4 + Li_2MgSiO_4)$. In addition, it is interesting that the ranking was unchanged following DFT calculations relative to the FF calculations, which shows that the forcefield is able to rank the candidate structures fairly accurately, at least in terms of energetics.

The lowest energy structure identified is found to be 0.3 eV/FU less stable relative to $\frac{1}{2}(LiMgPO_4 + Li_2MgSiO_4)$. The initial forcefield relaxation showed distortion of the co-

ordination polyhedra and unit cell, which was then corrected during following DFT relaxation. However, due to the problems with convergence, other forcefield alternatives must be considered.

6.4 Morse potential

Due to the nature of site swapping, the forcefield must be stable under non-equilibrium conditions. Though the Buckingham potential described above was found to have good agreement with the experimental lattice parameters and bonding geometries, many of the structures generated were not able to converge to the required convergence setting, or the shells were found to detach from their cores. It was therefore decided to investigate whether a Morse potential was more suitable, as this was originally constructed for use in glassy systems and for molecular dynamics, and is thus more likely to be stable under non-equilibrium conditions.

The parameters for the Morse potential were developed primarily for silicate materials of technological and geological importance.[16] The form of the potential model is discussed in more detail in Chapter 2, while the parameters are summarised below in Table 6.7. The forcefield was found to be in good agreement with the experimental structure of Li_2MgSiO_4. The Morse potential was less effective in maintaining the unit cell dimensions of $LiMgPO_4$, observing a significant expansion across all three length parameters (roughly 2% in each direction). The results for the unit cell volumes are summarised below in Table 6.8.

Again, the local bonding geometry is important, particularly as both octahedral and tetrahedral sites are available in the site-swapping routine. As can be seen from Table 6.9, the forcefield is able to maintain the coordination geometry; specifically, there is good agreement with the silicate and phosphate tetrahedra. There are larger differences in the lithium polyhedra; in particular, the first of the lithium tetrahedral sites in Li_2MgSiO_4. This proves

Interaction	D_{ij} (eV)	a_{ij} (Å^{-2})	r_0 (Å)	C_{ij} (eV Å^{12})
$Li^{0.6}$ – $O^{-1.2}$	0.001114	3.429506	2.681360	1.0
$Mg^{1.2}$ – $O^{-1.2}$	0.038908	2.281000	2.586153	5.0
$Si^{2.4}$ – $O^{-1.2}$	0.340554	2.006700	2.000000	1.0
$P^{3.0}$ – $O^{-1.2}$	0.831326	2.585833	1.800790	1.0
$O^{-1.2}$ – $O^{-1.2}$	0.042395	1.379316	3.618701	22.0

Table 6.7: The parameters used in the investigation of $LiMgPO_4$ – Li_2MgSiO_4. The cutoff of the short-range interactions was set to 15 Å.

Compound	Initial Value	Final Value	Difference
$LiMgPO_4$	281.3259	299.1026	17.7767 (+6.32%)
Li_2MgSiO_4	336.4499	339.6788	3.2289 (+0.96%)

Table 6.8: The unit cell volumes (Å^3) of $LiMgPO_4$ and Li_2MgSiO_4 following forcefield relaxation.

interesting when considering the forcefield relaxation of Li_3PO_4 with the same forcefield parameters, which shows a unit cell expansion of approximately 4%, due to the presence of lithium tetrahedra of similar sizes found in Li_2MgSiO_4.

6.4.1 Experimental Compositions

In order to assess how well the forcefield performs in the Monte Carlo site swapping routine, the end members of the series were investigated in the same way as above in Section 6.3.1. The results are summarised below for both $LiMgPO_4$ and Li_2MgSiO_4 in Table 6.10.

The results from the site-swapping using the Morse potential are somewhat expected from the unit cell parameter comparison. The potential had trouble relaxing the $LiMgPO_4$ structure,

Site	Average bond length (Å)	Volume (Å^3)	Coordination Number
$LiMgPO_4$			
Li octahedral	2.17 (+1.21%)	12.52 (+1.56%)	5.85 (−2.13%)
Mg octahedral	2.10 (−0.16%)	11.54 (−2.52%)	5.68 (−2.95%)
P tetrahedral	1.55 (+0.74%)	1.89 (+1.57%)	3.96 (−0.69%)
Li_2MgSiO_4			
Li1 tetrahedral	2.02 (+2.32%)	4.18 (+8.16%)	3.99 (+2.40%)
Li2 tetrahedral	2.03 (+0.06%)	4.02 (+4.09%)	3.95 (+8.62%)
Mg tetrahedral	1.98 (+1.32)	3.93 (+4.51%)	3.99 (+0.18%)
Si tetrahedral	1.60 (−2.26%)	2.11 (−6.73%)	3.99 (−0.11%)

Table 6.9: A summary of the coordination polyhedra in $LiMgPO_4$ and Li_2MgSiO_4 following forcefield relaxation, with the percentage difference compared to the experimental structure. There are two distinct lithium tetrahedral sites in Li_2MgSiO_4, as shown in Figure 6.4.

and was unable to find the experimental structure in the routine at all. In fact, it ranked several candidate structures as more stable than the experimental structure, though DFT calculations found these structures as less stable.

The Morse potential also appears to have issues with maintaining the unit cell parameters, as distortion occurs from the idealised oxide lattice. The structure from run 3 is shown in Figure 6.10 (a), which shows that the PO_4 tetrahedra are distorted. This structure is then found to be the least stable from the four runs following DFT calculations.

In contrast, as found with the Buckingham potential, a structure very similar to the experimental structure of Li_2MgSiO_4 was found multiple times in each run. The experimental structure of Li_2MgSiO_4 has partially occupied Li/Mg sites, which cannot be reflected in forcefield calculations. The structure found in the Monte Carlo run is simply an arrange-

Run	1	2	3	4
$LiMgPO_4$				
FF (eV/FU)	−0.1165	−0.1165	−0.0454	−0.0782
DFT (eV/FU)	+0.2880	+0.2881	+0.4500	+0.2864
Li_2MgSiO_4				
FF (eV/FU)	−0.0019	+0.0286	−0.0019	−0.0019
DFT (eV/FU)	+0.0653	+0.1370	+0.0653	+0.0653

Table 6.10: A comparison of the lowest energy structures found in each run in the studies of $LiMgPO_4$ and Li_2MgSiO_4 using the Morse potential. The energies shown are relative to the experimental structures.

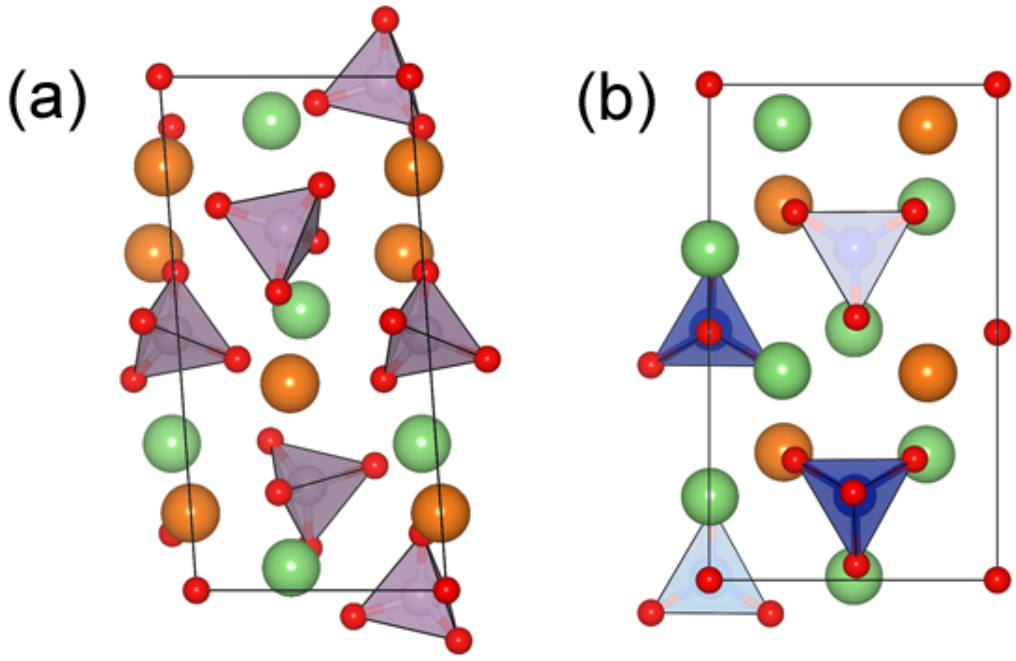

Figure 6.10: The lowest energy structure found in the Monte Carlo site-swapping routine for (a) $LiMgPO_4$ and (b) Li_2MgSiO_4 using the Morse potential.

ment of these sites with full occupancy, though it does not represent the site that has the highest Mg content. The structure is shown in Figure 6.10 (b).

Though the Monte Carlo investigation of Li_2MgSiO_4 was similar with both the Morse and Buckingham potentials, the Buckingham potential had much more success in the investigation of $LiMgPO_4$. However, the Buckingham potential also had trouble with the mixed composition $x = 0.5$, and hence the Monte Carlo run was repeated again for $x = 0.5$ with the Morse potential for comparative purposes.

6.4.2 $x = 0.5$

The cell was constructed as discussed in Section 6.3.2 with the Buckingham potential, with the same choice of parameters. The results from the Morse potential are summarised below in Table 6.11.

Structure	FF	Stability (eV/FU)	DFT (eV)	Stability (eV/FU)
2-103	−373.7032	+0.0024	−195.8623	+0.1347
2-304	−373.6502	+0.0554	−195.6379	+0.3591
3-775	−373.6388	+0.0185	−195.5882	+0.2033
1-87	−373.6123	+0.0251	−195.1301	+0.3178
4-995	−373.4002	+0.0781	−194.5834	+0.4545

Table 6.11: Table showing the five lowest energy structures from the Monte Carlo site swapping run. Each structure was named based on the run number and step, e.g. structure 2-103 was identified on run 2, step 103. The stability is taken relative to $\frac{1}{2}(LiMgPO_4 + Li_2MgSiO_4)$

Structure 2-103 is found to be more stable relative to $\frac{1}{2}(LiMgPO_4 + Li_2MgSiO_4)$ than any structures found using the Buckingham potential. In addition, there was a better record of convergence using the Morse potential. Therefore, although the experimental compositions were better modelled by the Buckingham potentials overall, the Morse potential appears to handle the mixed compositions well.

6.5 Parameter Optimisation

The above sections demonstrate the difficulty in choosing the forcefield for the initial site-swapping mechanism. However, there are other parameters involved in the site-swapping mechanism, including the number of starting structures, the maximum number of steps allowed in each run, the ratio of Li/Mg/vacancy to P/Si swaps and the reduced temperature for the Monte Carlo acceptance criteria.

This list is not exhaustive, and there are a number of other possibilities, for example the number of steps in the geometry optimisation and the optimisation method used, amongst others. However, these considerations are more based on computational resources and time; it was therefore decided to focus on the parameters directly involved in the initial site swapping mechanism and generation of the structures as opposed to those in the optimisation step. It was decided to choose 4 options for each of the different parameters, resulting in 256 combinations. They are summarised in Table 6.12 below.

Parameter	Option 1	Option 2	Option 3	Option 4
Number of starting structures	1	2	4	8
Number of steps	100	500	1000	2000
Ratio of Li/Mg/X : P/Si swap	1:1	2:1	5:1	10:1
Reduced T	0.001	0.01	0.1	1

Table 6.12: A list of the parameters chosen to investigate for the Monte Carlo site swapping routine.

This results in 961 calculations with the different numbers of starting structures. While the Buckingham potential gives better agreement with the end members, the instability of the shells could lead to some problems running so many calculations, and hence for the

parameter test the Morse potential was used. In addition, the composition $x = 0.5$ was used so that the ratio of Li/Mg/X : P/Si could be investigated.

For each separate combination, the lowest energy structure was taken from all available runs. For example, combination 256 has 8 starting structures creating 8 individual runs, each with a lowest energy structure. The lowest energy structure was taken from the lowest of these structures.

6.5.1 Analysis

For each parameter, the distribution of the lowest energy structures was examined using a box-plot, summarised in Figure 6.11, which shows the spread of the data using a five number summary: the lowest value, the lower quartile, the median, the upper quartile and the highest value.

As can be seen in the Figure 6.11 (a), the lowest energy structure was found using the maximum number of starting structures. However, the results for the lowest energy structure for each number of starting structures are quite similar, though 8 starting structures does find the structure with the overall lowest energy. The greatest change is in the distribution of the energies. As the number of starting structures increases, the energies of the most stable structure tends to decrease as demonstrated by the decrease in the median energy (shown by the thicker middle line), and the range of the energies also decreases.

It is not always the case that increasing the number of steps gives a lower energy structure, as shown in Figure 6.11 (b), where the lowest energy structure was found with 1000 steps. However, this is completely random, due to the fact that the swap choices are random. In terms of the swap ratio, shown in Figure 6.11 (c), 1:1 gives the lowest energy structure and the range of energies is fairly low, whereas 2:1 has a much larger range. For reduced temperature, shown in Figure 6.11 (d), 0.1 K gives the lowest energy structure but has a large

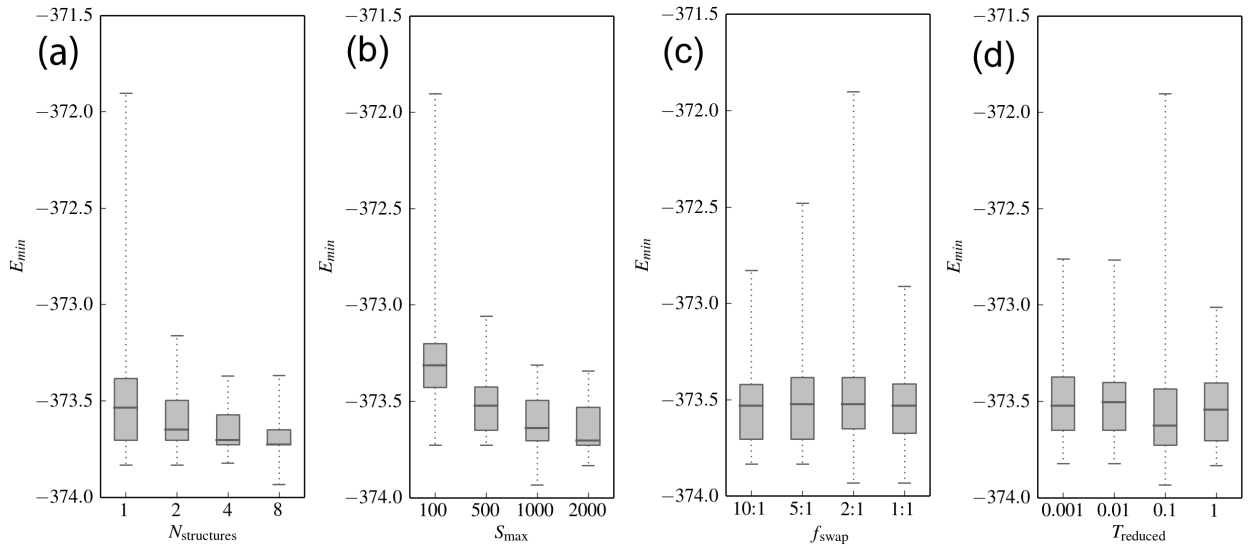

Figure 6.11: Box plots showing the distribution of the lowest energy structures found for each parameter (a) number of starting structures (b) maximum number of steps (c) Li/Mg/X : Si/P swap frequency and (d) reduced temperature.

range in energies. This result is likely an outlier, as it is outside of 1.5 × the interquartile range.

It may also be the case that the lowest energy structure is found with the greatest number of starting structures due to there being a greater number of steps available. However, it is likely that it is due to the increase in starting positions available. This is demonstrated in Figure 6.12 (a), which shows the number of steps needed to find the lowest energy structure for each number of starting structures. The distribution for each number of starting structures is fairly similar, with the lowest energy starting structure found roughly on step 500.

As the starting structure is so important, there may be a relationship between the initial and most stable energies. This is shown in Figure 6.12 (b), which shows the final energy versus the initial energy for each number of steps. There are eight bands, which represents the eight different starting structures used. The scatter plot demonstrates that both 100 and 500 steps do not provide enough swaps to lower the energy significantly from the initial starting energy.

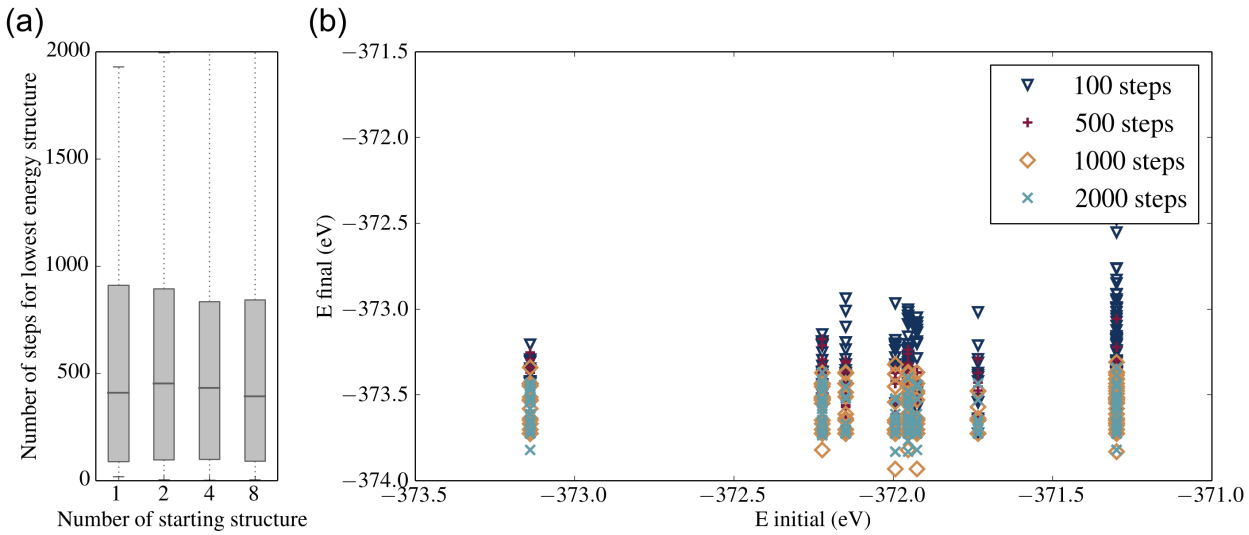

Figure 6.12: (a) A box plot showing the number of steps needed to find the lowest energy structure for each number of starting structures and (b) A scatter plot showing the starting energy versus the final energy for each structure.

6.5.2 Updating $x = 0.5$

In addition, there were several structures identified with lower forcefield energies than identified in the initial run of $x = 0.5$. The results are shown in the table below for the lowest five energy structures found in the parameter test (see Table 6.13).

The ideal set of parameters are not easily identified from inspection of the five lowest energy structures. Noticeably, all structures were run with either 1000 or 2000 steps. However, there is variation in the number of starting structures, the swap ratio and the reduced temperature, though the reduced T appears to favour a higher value. This conclusion is similar to the one drawn following analysis of the box plots.

The energies of the lowest five structures were calculated by DFT for comparison with $\frac{1}{2}(LiMgPO_4 + Li_2MgSiO_4)$, with the results summarised in Table 6.14. None of the structures identified in the lowest five energy structures were found to be more stable than structure 2-103 when relaxed in DFT, which again shows that the Morse potential has trouble

Structure	Energy (eV)	Runs	Steps	Swap Ratio	Reduced T
227-6	−0.2296	8	1000	1:1	0.1
243-6	−0.1302	8	2000	1:1	0.1
171-3	−0.1194	4	1000	1:5	0.1
116-2	−0.063	2	2000	1:1	1
192-3	−0.034	4	2000	1:10	1

Table 6.13: The lowest five structures from the parameter test. The structure is named based on the combination and run number, e.g. 227-6 is combination 227, run 6. The energy is given relative to the lowest energy found from the trial study of $x = 0.5$.

matching the DFT rankings. The structures themselves are shown below in Figure 6.13. In addition, the ordering is not consistent between the FF and DFT rankings, with structure 243-6 moving from the 2nd most stable in the FF ranking to the least stable in DFT.

6.6 Novel compositions

Due to the unit cell size created in the study of $x = 0.5$, investigations of $x = 0.25$ and $x = 0.75$ were readily available. Therefore, base structures of both were created, leading to the cells of $Li_7Mg_4PSi_3O_{16}$ and $Li_5Mg_4P_3Si_2O_{16}$, respectively, shown below in Figure 6.14.

As with the study of $x = 0.5$, the sites were then randomly distributed across the structure and initial starting structures were generated. The parameters for the site-swapping mechanism were taken from the analysis in Section 6.5.1, with the choice of 2000 Monte Carlo steps with 8 starting structures, a swap ratio of 1:1 and a reduced temperature of 0.1. Due to the issues with the forcefield choice, it was decided to run two Monte Carlo site-swapping routines for each composition, with one using the Buckingham potential and the other using

Structure	FF	Stability (eV/FU)	DFT (eV)	Stability (eV/FU)
227-6	−373.9329	−0.0550	−195.4379	+0.2408
243-6	−373.8335	−0.0302	−194.3687	+0.5081
171-3	−373.8227	−0.0275	−195.2923	+0.2772
116-2	−373.7669	−0.0135	−195.1527	+0.3110
192	−373.7376	−0.0062	−195.0959	+0.3261

Table 6.14: Table showing the five lowest energy structures from the Monte Carlo parameter optimisation of $x = 0.5$. The stability is taken relative to $\frac{1}{2}(LiMgPO_4 + Li_2MgSiO_4)$

a Morse potential, as neither potential is an ideal choice.

6.6.1 $x = 0.25$

To perform the Monte Carlo Site Swapping on $Li_7Mg_4PSi_3O_{16}$, 8 starting structures were used. Using the Buckingham potential, 192 structures were assessed before the 8 starting structures were identified, whereas only 18 structures were necessary for the Morse potential, showing a clear timing reason for using the Morse potential.

The results for $x = 0.25$ are shown below in Table 6.15. The lowest energy five structures accepted across all runs were taken. All structures were found to be unstable relative to the parent structures, with the lowest energy structure identified as being less stable by 0.2189 eV/FU. Both the Morse potential and Buckingham potential identified structures with similar DFT energies, with the lowest energy structure for each shown in Figure 6.15

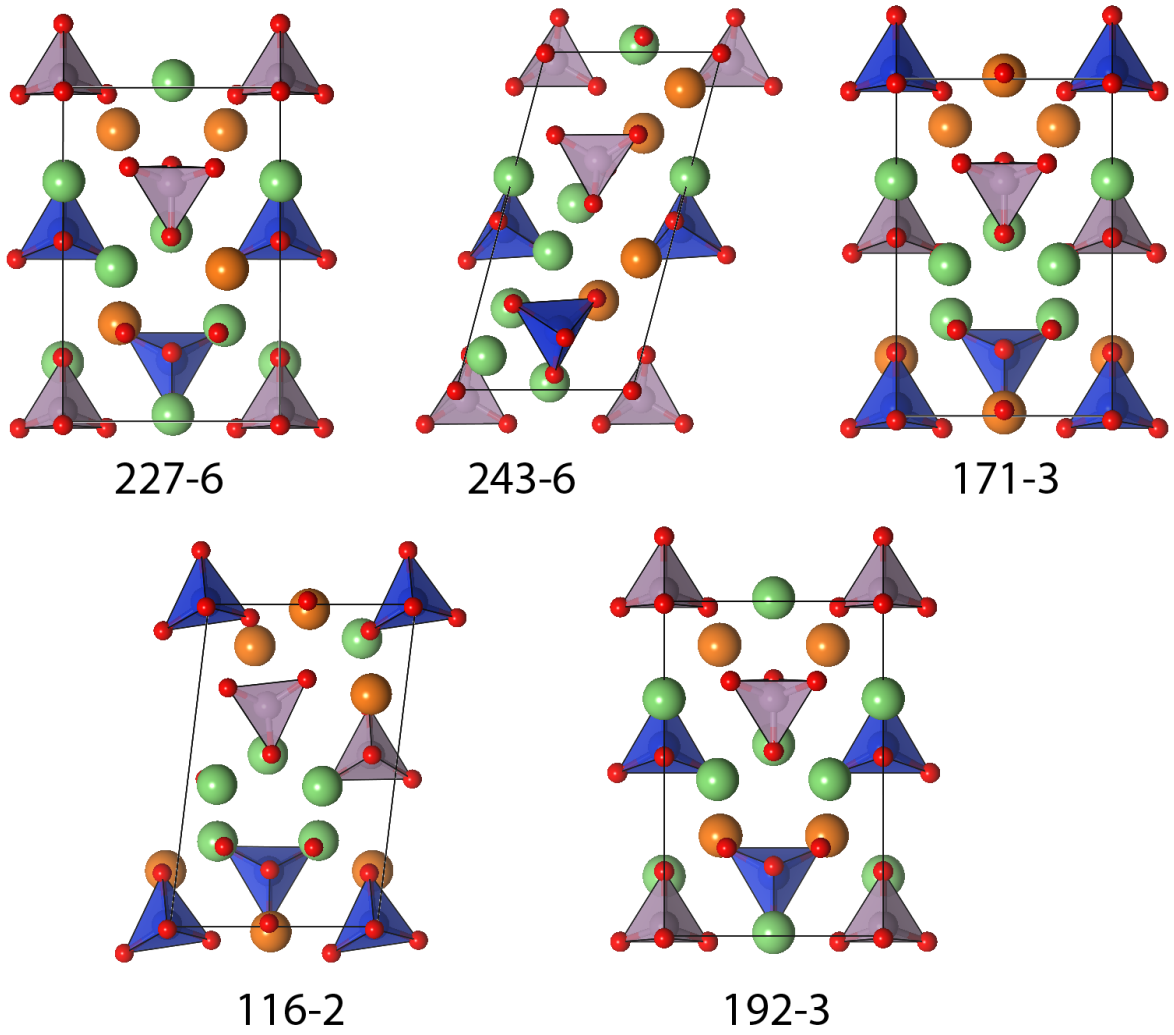

Figure 6.13: The five structures that have the lowest energy following the parameter optimisation using the Morse potential following DFT relaxation for $x = 0.5$. The structures are named based on combination and run number, e.g. 227-6 is combination 227, run 6

6.6.2 $x = 0.75$

Similar to the investigation above, the generation of starting structures for $x = 0.75$ using the Morse potential was more efficient than when using the Buckingham potential, with the former only requiring 15 attempts in comparison to 146.

The lowest energy five structures accepted across all runs were taken, where appropriate. Across all runs using the Buckingham potential, structure 3-700 was identified as the lowest energy structure, and was found over 50 times in the process. As such, DFT was only

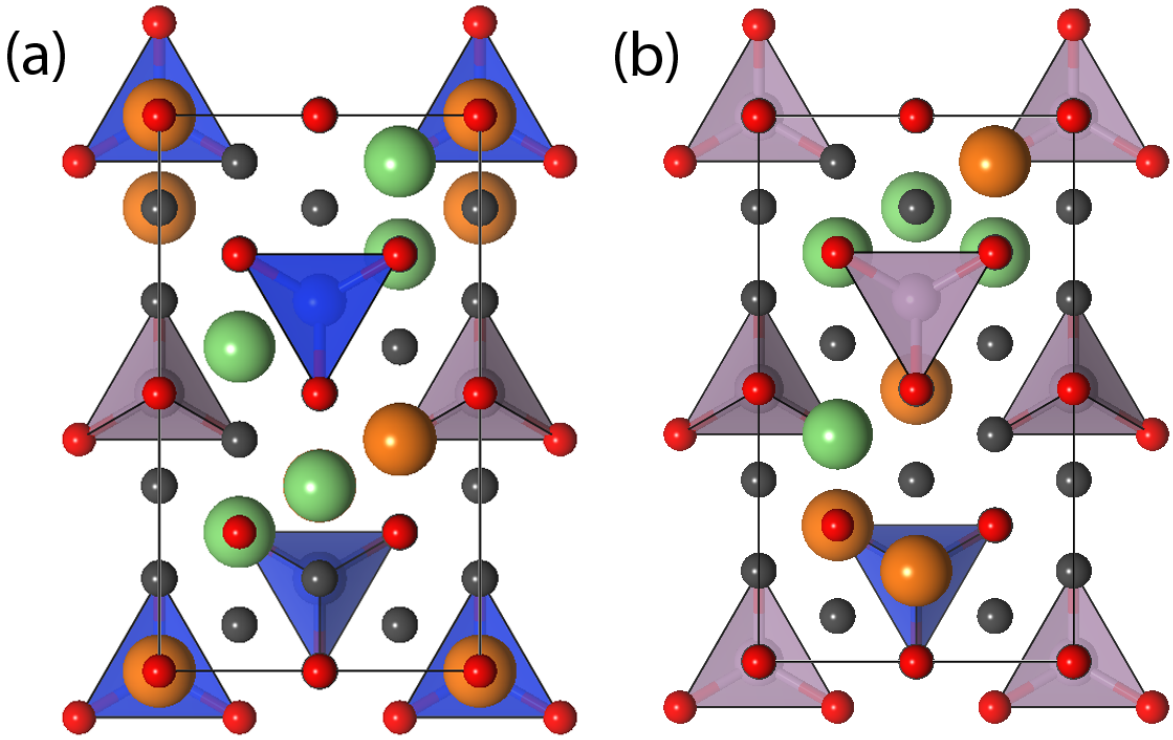

Figure 6.14: (a) The base cell for $x = 0.25$, giving $Li_7Mg_4PSi_3O_{16}$ (b) The base cell for $x = 0.75$, giving $Li_5Mg_4P_3Si_2O_{16}$.

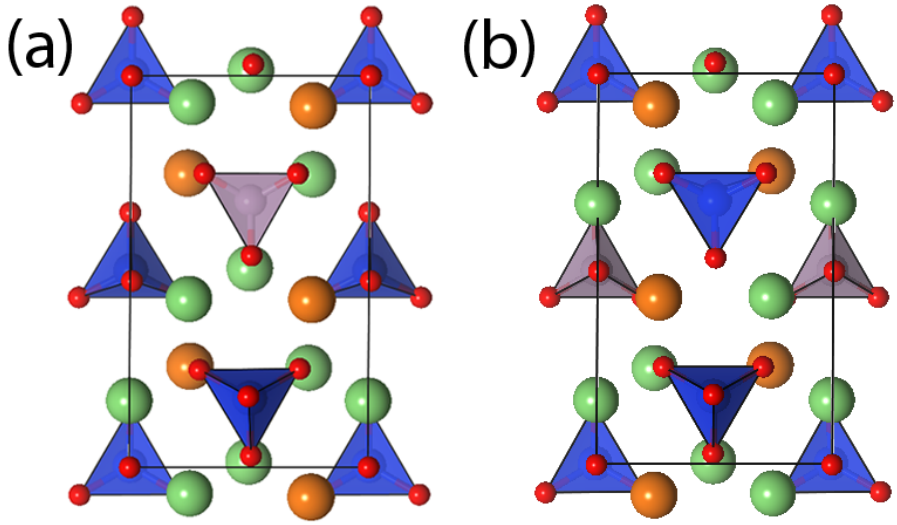

Figure 6.15: (The lowest energy structure found for $x = 0.25$ using (a) the Buckingham potential and (b) the Morse potential.

performed on this structure. The results for $x = 0.75$ are shown below in Table 6.16.

Structure	FF	Stability (eV/FU)	DFT (eV)	Stability (eV/FU)
Buckingham Potential				
2-1377	−867.0349	+0.2755	−199.6167	+0.4390
5-1506	−867.0965	0.2601	−200.2383	+0.2836
6-955	−867.0707	+0.2666	−200.3851	+0.2469
6-1483	−867.0791	+0.2645	−200.3560	+0.2542
7-742	−867.0235	+0.2784	−200.4732	+0.2249
Morse Potential				
1-807	−352.6704	+0.0719	−200.4972	+0.2189
5-512	−352.6787	+0.0707	−200.2178	+0.2887
7-1384	−352.5900	+0.0929	−200.1844	+0.2971
7-432	−352.6442	+0.0794	−200.4057	+0.2417
8-1983	−352.6425	+0.0798	−200.4928	+0.2200

Table 6.15: Table showing the five lowest energy structures from the Monte Carlo parameter optimisation of $x = 0.25$. The stability is taken relative to $\frac{1}{4}LiMgPO_4 + \frac{3}{4}Li_2MgSiO_4$.

All structures were found to be unstable relative to the parent structures following DFT relaxation, with the lowest energy structure identified as being less stable by 0.251 eV/FU. The Buckingham potential identified a structure with a lower energy than those found using the Morse potential, with both structures shown below in Figure 6.16.

Structure	FF	Stability (eV/FU)	DFT (eV)	Stability (eV/FU)
Buckingham Potential				
3-700	−959.8978	+0.1445	−190.4253	+0.2511
Morse Potential				
1-676	−394.3520	+0.0280	−189.8502	+0.3949
1-1576	−394.4691	−0.0013	−189.0265	+0.6008
2-596	−394.7915	−0.0819	−189.1656	+0.5660
2-1698	−394.4258	+0.0095	−189.5484	+0.4703
3-1038	−352.6425	−0.0234	−190.0005	+0.3573

Table 6.16: Table showing the five lowest energy structures from the Monte Carlo parameter optimisation of $x = 0.75$. The stability is taken relative to $\frac{3}{4}LiMgPO_4 + \frac{1}{4}Li_2MgSiO_4$

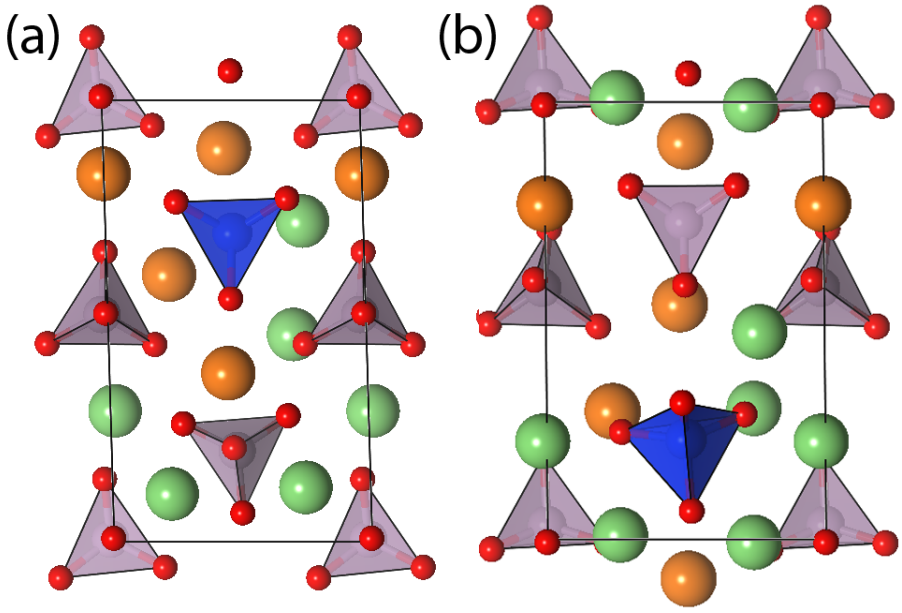

Figure 6.16: The lowest energy structures found for $x = 0.75$ using (a) the Buckingham potential and (b) the Morse potential

6.7 Conclusion

Monte Carlo site swapping has been applied to $(x)\mathrm{LiMgPO_4} + (1-x)\mathrm{Li_2MgSiO_4}$ with some success. Initially, the end members of the family were investigated to determine the most suitable forcefield potential. The Buckingham potential was able to identify the experimental structure of $\mathrm{LiMgPO_4}$ and a polymorph very close in energy to the experimental structure of $\mathrm{Li_2MgSIO_4}$. However, when applied to the system with $x = 0.5$, there were some issues with convergence.

The use of a Morse potential was also considered. This was successful in identifying a representation of the experimental structure of $\mathrm{Li_2MgSiO_4}$, albeit not representing the partial occupancy fully. However, it struggled to identify the experimental structure of $\mathrm{LiMgPO_4}$, not matching the DFT ranking of energies. With the use of a Morse potential, a more stable structure (following DFT calculations) for $x = 0.5$ was found than using the Buckingham potential.

Following parameter optimisation, the compositions of $x = 0.25$ and $x = 0.75$ were investigated, using both the Buckingham and Morse potentials. For $x = 0.25$, both forcefields identified structures of similar stability, whereas for $x = 0.75$ the Buckingham potential identified a structure that was found to be much lower in energy than any of the structures identified using the Morse potential. In all cases, the structures were found to be less stable than the respective ratios of the parent compounds.

In general, Monte Carlo site-swapping is a powerful tool to investigate the structures of unknown compounds. However, the assessment of the candidate structures is dependent on the initial forcefield optimisation accurately representing the stabilities of these structures relative to one another. It is often the case that the ranking of these structures is found to change following DFT calculations. Moving forward, it appears that one way to minimise this problem is to use multiple forcefields to investigate the same system.

References

1. Fergus, J. W. Ceramic and polymeric solid electrolytes for lithium-ion batteries. *Journal of Power Sources* **195,** 4554–4569 (2010).

2. Knauth, P. Inorganic solid Li ion conductors: An overview. *Solid State Ionics* **180,** 911–916 (2009).

3. Goodenough, J. B. Evolution of strategies for modern rechargeable batteries. *Accounts of Chemical Research* **46,** 1053–1061 (2013).

4. Kamaya, N. *et al.* A lithium superionic conductor. *Nature* **10,** 682–686 (2011).

5. Zaghib, K. *et al.* Review and analysis of nanostructured olivine-based lithium rechearge-able batteries: Status and trends. *Journal of Power Sources* **232,** 357–369 (2013).

6. Joachin, H., Kaun, T. D., Zaghib, K. & Prakash, J. Electrochemical and Thermal Studies of Carbon-Coated $LiFePO_4$ Cathode. *Journal of The Electrochemical Society* **156,** A401–A406 (2009).

7. Malik, R., Abdellahi, A. & Ceder, G. A Critical Review of the Li Insertion Mechanisms in $LiFePO_4$ Electrodes. *Journal of The Electrochemical Society* **160,** A3179–A3197 (2013).

8. Meethong, N., Kao, H., Speakman, S. A. & Chiang, Y.-M. Aliovalent substitutions in olivine lithium iron phosphate and impact on structure and properties. *Advanced Functional Materials* **19,** 1060–1070 (2009).

9. Hanic, F., Handlović, M., Burdová, K. & Majling, J. Crystal structure of lithium mag-nesium phosphate, $LiMgPO_4$: Crystal chemistry of the olivine-type compounds. *Journal of Crystallographic and Spectroscopic Research* **12,** 99–127 (1982).

10. Iskhakova, L. D. & Rybakov, V. B. Crystal structure of Li_2MgSiO_4. *Crystallography Reports* **48,** 39–43 (2003).

11. Deng, Y. *et al.* Structural and mechanistic insights into fast lithium-ion conduction in Li_4SiO_4–Li_3PO_4 solid electrolytes. *Journal of the American Chemical Society* **137,** 9136–9145 (2015).

12. George, S., Anjana, P. S., Deepu, V. N., Mohanan, P. & Sebastian, M. T. Low-temperature sintering and microwave dielectric properties of Li_2MgSiO_4 ceramics. *Journal of the American Ceramic Society* **92,** 1244–1249 (2009).

13. Zhang, P. *et al.* Molecular dynamics study on ion diffusion in $LiFePO_4$ olivine materials. *The Journal of Physical Chemistry A* **112,** 5406–5410 (2008).

14. Tolchard, J. R., Islam, M. S. & Slater, P. R. Defect chemistry and oxygen ion migration in the apatite-type materials $La_{9.33}Si_6O_{26}$ and $La_8Sr_2Si_6O_{26}$. *Journal of Materials Chemistry* **13,** 1956–1961 (2003).

15. Lewis, G. V. & Catlow, R. A. Potential models for ionic oxides. *Journal of Physics C: Solid State Physics* **18,** 1149–1161 (6 1985).

16. Pedone, A., Malavasi, G., Menziani, M. C., Cormack, A. N. & Segre, U. A new self-consistent empirical interatomic potential model for oxides, silicates, and silica-based glasses. *The Journal of Physical Chemistry B* **110,** 11780–11795 (2006).

Chapter 7

Conclusions

This thesis has outlined two new methods for crystal structure prediction. The first, the Extended Module Materials Assembly method, was applied in Chapters 4 and 5 to a series of hexagonal pervoskite structures. In the first of these chapters, the method was successful in predicting known experimental structures, and work focussed on logical extensions to these structures by increasing the stacking length. In the second of these chapters, EMMA was applied to a composition with an unknown structure, with new experimental work not in complete agreement with the proposed model. Unfortunately, the candidate structures were all found to be less stable than the proposed structure using DFT calculations.

In Chapter 4, a Hubbard U was applied to correct for the highly correlated d-orbitals present in the system due to Co^{2+}. As the work primarily focussed on the prediction of stable systems rather than an investigation of the systems themselves, a literature value was used. Further work could be done to investigate the dependence of the spin configuration on U and whether varying U favours particular systems. Chapter 5 looked at an unsolved structure in a related system; however, with no access to first-hand experimental data, comparison between simulation and experiment was not easy. Therefore, future work within the group should focus on synthesising $Ba_3Nb_2O_8$ and performing a structural refinement, so that further

computational work can be facilitated with more recent experimental data. In addition, identifying a forcefield without a three-body term would give a better chance of finding structures that deviate from those currently known.

Chapter 6 showed the implementation of a site-swapping method using Monte Carlo. In this system, the structures investigated were mixed phases of known compounds. The structures found with the lowest energy were within reasonable stability limits to consider experimental synthesis. However, again there are limitations to this method, such as the use of forcefields and the choice of parameters. While efforts were made to overcome these limitations, such as the use of two forcefields and varying the parameters, there is still room for improvement. Future work on this system should primarily focus on refinement of the methodology and calculations. It is likely that site-disorder is present in the mixed-phases, which could significantly change the structures that are found to be stable.

There are several key advantages to using EMMA as opposed to other methods. The high-throughput design means that all structures that obey the combination rules are generated, and the use of both forcefields and DFT means that thousands of structures can be assessed. In Chapter 5, the proposed structure for $Ba_3Nb_2O_9$ was generated, but it was not carried forward to DFT calculations due to its low ranking in the forcefield screening compared to other candidate structures. This demonstrates one of the disadvantages of using EMMA: its reliance on forcefields means that the forcefield has to represent the system accurately, working well when the system is known and understood. However, it works less well when the system is unknown, though there is the option of using multiple forcefields, which increases the number of calculations necessary. However, despite the disadvantages, the versatility and power of the EMMA approach cannot be ignored. In particular, the integration of experimental knowledge with the choice of module sets is an important step, with prediction and experimentation working together to progress and develop novel and commercially viable materials.

Optimisation of both codes remains a key challenge. In both processes, user input is required at all stages, and future work could focus on making the methods more automated (for example, automatically carrying structures forward from forcefield to DFT stages). Combining both methods is also an avenue of work being explored in the group at present, as this enables the evaluation of thousands of candidate structures without having to generate them all. Other future work involves the experimental synthesis of candidate structures that were identified as stable, as well as investigation of their electronic properties computationally.

Overall, this thesis has demonstrated that methodologies that work for one system might not work for the other. The EMMA method was chosen because the hexagonal pervoskite structures can easily be broken down into discrete layers, while Monte-Carlo site swapping was applied to the $(x)\mathrm{LiMgPO_4} + (1-x)\mathrm{Li_2MgSiO_4}$ system due to the presence of specific sites that could be occupied by different ions. These methods were specifically designed with the question in mind, and hence cannot be transferred easily. More general future work for the field of crystal structure prediction in general should focus on designing methods that are applicable to a wide variety of problems.